

# PRG

## Photogrammetrie Fernerkundung Geoinformation

Journal for Photogrammetry, Remote Sensing  
and Geoinformation Science

Organ der Deutschen Gesellschaft für Photogrammetrie,  
Fernerkundung und Geoinformation (DGPF) e. V.

Jahrgang 2014, Heft 4

Hauptschriftleiter:  
Prof. Dr.-Ing. Wolfgang Kresse

Schriftleiter:  
Prof. Dr.-Ing. Stefan Hinz, Prof. Dr. techn. Franz Rottensteiner,  
Prof. Dr. rer.nat. Ulrich Michel, Prof. Dr. rer.nat. Lars Bernard  
und Dr.-Ing. Eckhardt Seyfert

**Redaktionsbeirat** (Editorial Board): Clement Atzberger, Andrew Frank,  
Christian Heipke, Joachim Hill, Patrick Hostert, Hans-Gerd Maas, Wolfgang  
Reinhardt, Camillo Ressel, Jochen Schiewe



E. Schweizerbart'sche Verlagsbuchhandlung  
(Nägele u. Obermiller) Stuttgart 2014



Deutsche Gesellschaft für Photogrammetrie, Fernerkundung  
und Geoinformation (DGPF) e.V.  
Gegründet 1909

---

Die *Deutsche Gesellschaft für Photogrammetrie, Fernerkundung und Geoinformation* (DGPF) e.V. unterstützt als Mitglieds- bzw. Trägergesellschaft die folgenden Dachverbände:



International Society  
for Photogrammetry  
and Remote Sensing

**DAGM**

Deutsche Arbeits-  
gemeinschaft für  
Mustererkennung e.V.



---

Herausgeber:

© 2014 Deutsche Gesellschaft für Photogrammetrie, Fernerkundung und Geoinformation (DGPF) e.V.  
Präsident: Prof. Dr. Thomas Kolbe, Technische Universität München, Institut für Geodäsie, GIS und Landmanagement, Lehrstuhl für Geoinformatik, Arcisstraße 21, 80333 München, Germany, Tel. +49-89-289-23888  
Geschäftsstelle: Tanja Nyc, c/o Technische Universität München, Institut für Geodäsie, GIS und Landmanagement, Lehrstuhl für Geoinformatik, Arcisstraße 21, 80333 München, Germany, Tel.: +49-89-289-22578, e-mail: [geschaeftsstelle@dgpf.de](mailto:geschaeftsstelle@dgpf.de), Gläubiger-Identifikationsnummer DE54 ZZZ0 0000 8351 37

Published by: E. Schweizerbart'sche Verlagsbuchhandlung (Nägele u. Obermiller), Johannesstraße 3A, 70176 Stuttgart, Germany, Tel.: +49-711 351456-0, Fax: +49-711 351456-99, e-mail: [mail@schweizerbart.de](mailto:mail@schweizerbart.de)  
Internet: <http://www.schweizerbart.de>

© Gedruckt auf alterungsbeständigem Papier nach ISO 9706-1994

All rights reserved including translation into foreign languages. This journal or parts thereof may not be reproduced in any form without permission from the publishers.

Die Wiedergabe von Gebrauchsnamen, Handelsnamen, Warenbezeichnungen usw. in dieser Zeitschrift berechtigt auch ohne besondere Kennzeichnung nicht zu der Annahme, dass solche Namen im Sinne der Warenzeichen- und Markenschutz-Gesetzgebung als frei zu betrachten wären und daher von jedermann benutzt werden dürften.

Verantwortlich für den Inhalt der Beiträge sind die Autoren.

ISSN 1432-8364

Science Citation Index Expanded (also known as SciSearch®) Journal Citation Reports/Science Edition

Hauptschriftleiter: Prof. Dr.-Ing. Wolfgang Kresse, Hochschule Neubrandenburg, Fachbereich Landschaftswissenschaften und Geomatik, Brodaer Straße 2, 17033 Neubrandenburg, Germany, e-mail: [kresse@hs-nb.de](mailto:kresse@hs-nb.de)

Schriftleiter: Prof. Dr.-Ing. Stefan Hinz, Karlsruher Institut für Technologie – KIT, Institut für Photogrammetrie und Fernerkundung, Englerstraße 7, 76131 Karlsruhe, Germany, e-mail: [stefan.hinz@ipf.uni-karlsruhe.de](mailto:stefan.hinz@ipf.uni-karlsruhe.de), Privatdozent Dr. techn. Franz Rottensteiner, Leibniz Universität Hannover, Institut für Photogrammetrie und GeoInformation, Nienburger Straße 1, 30167 Hannover, Germany, e-mail: [rottensteiner@ipi.uni-hannover.de](mailto:rottensteiner@ipi.uni-hannover.de), Prof. Dr. rer. nat. Ulrich Michel, Pädagogische Hochschule Heidelberg, Czernyring 22/11–12, 69115 Heidelberg, Germany, e-mail: [michel@ph-heidelberg.de](mailto:michel@ph-heidelberg.de), Prof. Dr. rer. nat. Lars Bernard, Technische Universität Dresden, Fachrichtung Geowissenschaften, Helmholtzstraße 10, 01062 Dresden, Germany, e-mail: [lars.bernard@tu-dresden.de](mailto:lars.bernard@tu-dresden.de), und Dr.-Ing. Eckhardt Seyfert, Landesvermessung und Geobasisinformation Brandenburg, Heinrich-Mann-Allee 103, 14473 Potsdam, Germany, e-mail: [eckhardt.seyfert@geobasis-bb.de](mailto:eckhardt.seyfert@geobasis-bb.de)

Erscheinungsweise: 6 Hefte pro Jahrgang.  
Bezugspreis im Abonnement: € 239,- pro Jahrgang. Mitglieder der DGPF erhalten die Zeitschrift kostenlos. Der Online-Zugang ist im regulären Subskriptionspreis enthalten.  
Anzeigenverwaltung: E. Schweizerbart'sche Verlagsbuchhandlung (Nägele u. Obermiller), Johannesstraße 3A, 70176 Stuttgart, Germany, Tel.: +49-711 351456-0; Fax: +49-711 351456-99.  
e-mail: [mail@schweizerbart.de](mailto:mail@schweizerbart.de), Internet: <http://www.schweizerbart.de>  
Bernhard Harzer Verlag GmbH, Westmarkstraße 59/59a, 76227 Karlsruhe, Germany, Tel.: +49-721 944020, Fax: +49-721 9440230, e-mail: [Info@harzer.de](mailto:Info@harzer.de), Internet: [www.harzer.de](http://www.harzer.de)  
Printed in Germany by Tutte Druckerei & Verlagsservice GmbH, 94121 Salzweg, Germany.

## PFG – Jahrgang 2014, Heft 4 Inhaltsverzeichnis

---

### Editorial

BILL, R.: Unmanned Aerial Systems (UAS) – Attractive Extensions to Spatial Data Collection Methods . . . . .	225
---	-----

---

### Originalbeiträge

ELING, C., KLINGBEIL, L., WIELAND, M. & KUHLMANN, H.: Direct Georeferencing of Micro Aerial Vehicles – System Design, System Calibration and First Evaluation Tests . . . . .	227
REHAK, M., MABILLARD, R. & SKALOUD, J.: A Micro Aerial Vehicle with Precise Position and Attitude Sensors. . . . .	239
BRAUCHLE, J., RÜTHER-KINDEL, W. & BERGER, R.: MACS-TumbleCam – A Novel Approach for Aerial Oblique Imaging . . . . .	253
BÜTTNER, A. & RÖSER, H.-P.: Hyperspectral Remote Sensing with the UAS “Stuttgarter Adler”– System Setup, Calibration and First Results . . . . .	265
BERNHARD, E.-M., TWELE, A. & MARTINIS, S.: The Effect of Vegetation Type and Density on X-Band SAR Backscatter after Forest Fires . . . . .	275

---

### Beitrag aus Wissenschaft und Praxis

CONTE, G., RUDOL, P. & DOHERTY, P.: Evaluation of a Light-weight Lidar and a Photogrammetric System for Unmanned Airborne Mapping Applications. . . . .	287
---	-----

---

### Mitteilungen

Hochschulnachrichten	
Universität Stuttgart, Dissertation Wassim Moussa . . . . .	299
Deutsche Geodätische Kommission: DGK-Wissenschaftspreis . . . . .	301
Neuerscheinung . . . . .	301
Veranstaltungskalender . . . . .	302
Korporative Mitglieder . . . . .	303

Zusammenfassungen der „Originalbeiträge“ und der „Beiträge aus Wissenschaft und Praxis“  
(deutsch und englisch) sind auch verfügbar unter [www.dgpf.de/neu/pfg/ausgaben.htm](http://www.dgpf.de/neu/pfg/ausgaben.htm)





## Unmanned Aerial Systems (UAS) – Attractive Extensions to Spatial Data Collection Methods

Drones, UAV / UAS (unmanned aerial / aircraft / airborne / assisted vehicles / systems) – also called RPAS (remotely piloted aircraft systems) – are currently resounded throughout the land. For these small aircrafts – here named unmanned aerial systems (UAS) – there are a lot of very interesting application possibilities and exciting research questions in the context of photogrammetry, remote sensing and geoinformatics, of which the reader can convince herself or himself in this focussed issue on the topic of UAS. Selected papers which were held at the conference UAV-g 2013 in Rostock in September 2013 (see GRENZDÖRFFER & BILL (eds.), 2013: UAV-g 2013. ISPRS Archives Volume XL-1/W2) have been compiled, updated, revised and passed through the review system of PFG.

The UAS overall system consists of the carrier flying platform with the on-board sensors, the payload – in the simplest case a digital camera – and the ground station for guiding and monitoring the flight from take-off to landing. As platform for aerial photography model airplanes, model helicopters, multicopters or balloons / blimps are available. Interesting platforms for UAS photogrammetry, operating with less than 5 kg including payload, are often called micro- and mini-UAS. This may usually fly in sight with a general permit in uncontrolled airspace. Aboard the carrier platform, various sensors such as GNSS, INS, compass, and barometer are combined to determine the position and orientation of the platform for the integrated navigation solution. Payloads will be depending on the application envisioned: a variety of sensors, e.g. still video camera, digital camera, multispectral camera, spectrometers, hyperspectral sensors or laser scanners, are used.

UAS are able to close the large gap between the terrestrial and airborne/spaceborne geodata acquisition for many applications: for a limited areal extent of the investigated territory

both a great ground resolution and a high temporal relevance can be delivered. Accordingly, they find a variety of applications such as in the geosciences (geography, geomorphology, geophysics or meteorology), environmental and planning disciplines (vegetation science, landscape ecology, environmental monitoring, settlement dynamics, agriculture and forestry, archaeology) and also in the surveying and geographic information industry (low-cost photogrammetry, topographic mapping and land use changes).

Common projects include some 100 to some 1000 pictures, which are recorded in less than half an hour. The calculations for the orientation of the images – usually using some control points in the terrain – can be done locally at the workstation or in the cloud. The achievable accuracy using calibrated cameras and flown in altitudes up to about 50 m are in the centimetre range. Standard products such as orthophoto mosaics, digital terrain or surface models and 3D point clouds are generated largely automated from the aerial photographs.

Research is still required, inter alia, in the precise orientation near real-time, in the fusion of many different sensors on board, in the derivation of further products – e.g. to 3D feature extraction or image interpretation – or in the joint and simultaneous use of multiple UAS (UAS swarms) to cover larger areas. The papers selected in this special issue of PFG illustrate a snapshot in the research landscape with a special focus on photogrammetry, i.e. orientation and georeferencing as well as new sensors.

ELING, KLINGBEIL, WIELAND & KUHLMANN present a new developed on-board direct georeferencing system, which is real-time capable, applicable for lightweight UAS and which provides very precise results (position accuracy ~5 cm and attitude accuracy ~0.5 deg). The hardware development and some details of the

implemented software are described. In this context especially the RTK-GNSS software and the concept of the attitude determination using inertial sensors, magnetic field sensors as well as an on-board GNSS baseline will be highlighted. Finally they present results of their first field tests.

REHAK, MABILLARD & SKALOUĐ are developing a low-cost micro UAS with the capability of direct georeferencing. They explain the hardware implementation and especially the non-trivial synchronization of all components. Several field tests were done and the results are discussed.

BRAUCHLE, RÜTHER-KINDEL & BERGER are describing the new, light weight 3D measurement camera system MACS-TumbleCam that was developed at the German Aerospace Center DLR Berlin-Adlershof. The first test flights show a ground resolution of 2 cm and height resolution of 3 cm, which underline the extraordinary capabilities of the platform and the measurement camera system.

BÜTTNER & RÖSER are dealing with hyperspectral remote sensing on-board of the UAS "Stuttgarter Adler". Besides a detailed specification of the system concept and instrument

design, the calibration procedure of the hyperspectral sensor system is discussed and results of the laboratory calibration are presented. The complete processing chain of measurement data is described and first results of measurement-flights over agricultural test sites are presented.

The developed airborne lidar Scanner (ALS) system of CONTE, RUDOL & DOHERTY consists of a high-precision GNSS receiver, an inertial measurement unit and a magnetic compass which are used to complement a lidar sensor in order to determine a digital surface model. They present the evaluation of the accuracy of the generated surface model in comparison to a surface model generated using a commercial photogrammetric software. Finally, the multi-echo capability of the used lidar sensor is evaluated in areas covered with dense vegetation.

I hope you will find this focussed issue on UAS photogrammetry both interesting and useful for your daily work.

RALF BILL  
Chair for Geodesy and Geoinformatics  
Rostock University

This PFG-issue 4/2014 contains one article that does not belong to the general focus of "Unmanned Aerial Systems": EVA-MARIA BERNHARD et al. analysed the detectability of vegetation changes after forest fires using TerraSAR-X images and now publish some very promising results in their article. As be-

ing based on data, this article has a slightly other perspective than the UAS-articles that mostly focus on hardware aspects, but completes the general theme of photogrammetry and remote sensing.

WOLFGANG KRESSE, Neubrandenburg



# Direct Georeferencing of Micro Aerial Vehicles – System Design, System Calibration and First Evaluation Tests

CHRISTIAN ELING, LASSE KLINGBEIL, MARKUS WIELAND & HEINER KUHLMANN, Bonn

**Keywords:** direct georeferencing, RTK GPS, IMU, Kalman filtering, real-time operating system

**Summary:** In this article, a direct georeferencing system for the position and attitude determination of micro aerial vehicles (MAVs) is presented. The system consists of two GPS receivers, inertial sensors, a magnetometer, a barometer and an external sensor input for the integration of visual odometry data from stereo camera systems. The main characteristics of the system are that (1) it is real-time capable, (2) it is lightweight, to be applicable to MAVs and (3) it provides results with accuracies  $< 5$  cm for the positions and  $< 0.5$  deg to 1 deg for the attitudes. In this contribution the hardware development and the implemented algorithms for the direct georeferencing are described. In this context especially the RTK GPS and the attitude determination will be highlighted. Finally, details on the system calibration, results of a test flight, including a comparison to a photogrammetric bundle adjustment, and an outlook on further developments will conclude this contribution.

**Zusammenfassung:** *Direkte Georeferenzierung von MAVs (Micro Aerial Vehicles) – Systementwurf, Systemkalibrierung und erste Tests.* In diesem Beitrag wird ein System zur direkten Georeferenzierung von kleinen unbemannten Flugobjekten präsentiert. Das System ist in der Lage, Positionen und Orientierungen mit Genauigkeiten von  $< 5$  cm und  $< 0.5$  bis 1 deg in Echtzeit zu bestimmen. Dazu werden zwei GPS Empfänger, Inertial- und Magnetfeldsensoren, ein Barometer und in Zukunft auch Informationen aus Stereo-Kamera-Systemen verwendet. Neben Aspekten der Systementwicklung stehen in diesem Beitrag die implementierten Algorithmen im Vordergrund. In diesem Kontext werden insbesondere Details zum aktuellen Stand der Entwicklung der RTK GPS Auswertung und der Orientierungsbestimmung vorgestellt. Abschließend wird die Systemkalibrierung beschrieben, und es folgen erste Ergebnisse aus Flugexperimenten inklusive einem Vergleich zu einer photogrammetrischen Bündelausgleichung sowie ein Ausblick auf zukünftige Arbeiten.

## 1 Introduction

The acquisition of data by use of mobile platforms has become established in many communities in the recent decades. For some years now also UAVs (unmanned aerial vehicles) are commonly used for mobile mapping applications, since UAVs have the advantage of being able to overfly inaccessible and also dangerous areas. Furthermore, they can get very close to objects to achieve high resolution data with quite low resolution sensors. Especially in the fields of precision farming (XIANG

& TIAN 2011), infrastructure inspection (MERZ & KENDOUL 2011) or surveying (EISENBEISS et al. 2005) UAVs are meanwhile often deployed.

Recently, there has been a discussion concerning the term UAV. Since this paper is particularly dealing with lightweight UAVs the more specific term MAV (micro aerial vehicle) will be used throughout this paper. MAVs can generally be characterized having a weight limit of 5 kg and a size limit of 1.5 m (EISENBEISS 2009).

## 1.1 Objectives

This contribution is focused on the development of a real-time capable direct georeferencing system for MAVs. The reason for developing a direct instead of an indirect georeferencing system is that spatial and time restrictions often exclude the possibility to deploy ground control points. The demand for the real-time capability of the system results from the aim to also use the georeferencing for the autonomous navigation of the MAV and to enable precise time synchronization. (As a side note, in Germany currently only partially automatic flights are permitted.) Furthermore, the real-time direct georeferencing also offers the opportunity to process the collected mapping data during the flight. For example using the georeferencing as initial values for the bundle adjustment of collected images accelerates the processing time significantly.

The utility of a real-time direct georeferencing for MAV applications can also be illustrated by the project the authors are working on: *Mapping on Demand*.

The goal of this project is to develop an MAV that is able to identify and measure inaccessible three-dimensional objects by use of visual information. A major challenge within the project comes with the term 'on demand', which includes the search, the interpretation and the user specific visualization of spatial information. The MAV is intended to fly fully autonomous on the basis of a high-level user inquiry. During the flight obstacles have to be avoided (HOLZ et al. 2013) and the collect-



**Fig. 1:** The MAV (modified OktoXL, HiSystems) including the sensor and processing components, developed within the project *Mapping on Demand*.

ed images have to be processed on-the-fly in order to extract semantic information (LOCH-DEHBI et al. 2013), which can be used to refine the trajectory planning (NIEUWENHUISEN et al. 2013) in real-time.

Fig. 1 shows the current version of the MAV, as it is developed within the project.

It contains the direct georeferencing system, two stereo camera pairs, which will serve as an additional sensory input for the position and attitude determination (SCHNEIDER et al. 2013) and a 5 MPixel industrial camera as the actual mapping sensor. A small computer is used for the image processing, the flight planning and the machine control.

## 1.2 Accuracy Requirements

The position and attitude accuracy requirements are different for the navigation and the 3D object reconstruction within this project. Since the MAV is intended to maintain a safety distance of 0.5 m to obstacles, a position accuracy of 0.1 m is sufficient for the navigation. For the machine control the attitude accuracies should be in the range of 1 deg – 5 deg.

Compared to the navigation the positions and attitudes have to be known better for the 3D object reconstruction, since the absolute georeferencing of the final product, e.g. high-resolution 3D model of a building, is based on the positions and attitudes from the direct georeferencing system. Therefore, the position accuracy should be 1 cm – 3 cm and the attitude accuracy should preferably be better than 1 deg. At this point it has to be noticed that the relative accuracy of the exterior camera orientation can be improved by an ensuing photogrammetric bundle adjustment, but systematic georeferencing errors definitely have to be avoided.

## 1.3 Structure of the Paper

In section 2 the related work on direct georeferencing for MAVs is summarized. Details on the sensors and the overall system development will be shown in section 3. In section 4 the software and algorithm development follows. In this context details to the RTK GPS

positioning algorithms and the concept to the attitude determination will be presented. Section 5 is focused on the system calibration. In section 6 results of a test flight including a comparison to results from a photogrammetric bundle adjustment will be presented. Since the algorithm development is not yet completed an outlook on future developments concludes this contribution (section 7).

## 2 Related Work

Direct georeferencing has extensively been researched in airborne applications, such as presented in SCHWARZ et al. (1993), SKALOUUD (1999), and HEIPKE et al. (2002). However, these systems cannot be adopted easily for MAVs operating in urban areas. There are two reasons for that: (1) Due to the lower flying altitude the GPS measurement conditions are often not ideal, since obstacles like trees or buildings lead to shadowing and multipath effects. Thus, additional sensors, e.g. an inertial measurement unit (IMU) play a more important role. (2) The choice of these sensors is restricted by space and weight limitations of the MAV. For instance, only a lower quality IMU can be used. For this reason, further sensors, e.g. cameras, are needed to also allow for a reliable georeferencing during GPS losses of lock.

Usually, direct georeferencing of MAVs is done by means of single L1 C/A code GPS receivers and low-cost inertial sensors as well as magnetometers (YOO & AHN 2003, MERZ & KENDOUL 2011, XIANG & TIAN 2011). However, the resulting accuracies of these sensor combinations ( $\sigma_{\text{pos}} \approx 2 \text{ m} - 10 \text{ m}$  and  $\sigma_{\text{att}} \approx 2 \text{ deg} - 10 \text{ deg}$ ) are insufficient for geodetic MAV applications. Therefore, the development of precise direct georeferencing systems for MAVs is currently highly demanded (BLÁHA et al. 2011). First approaches applying RTK (real-time kinematic) GPS on MAVs were presented in RIEKE et al. (2011), STEMPFHUBER & BUCHHOLZ (2011), BÄUMKER et al. (2013) and REHAK et al. (2014).

REHAK et al. (2014) additionally use a Field-Programmable Gate Array (FPGA) for the processing of 4 redundant MEMS-IMU chips. Nevertheless, in none of the referenced devel-

opments the position and attitude determination is performed in real-time on board of the MAV.

## 3 System Design

This research is focused on the development of a direct georeferencing system with the following characteristics: (1) The weight of the system has to be less than 500 g to be applicable to MAVs. (2) The system has to be real-time capable. (3) Outages of single sensors should be bridgeable by other sensors. (4) The system is intended to provide accurate positions ( $\sigma_{\text{pos}} < 5 \text{ cm}$ ) and attitudes ( $\sigma_{\text{deg}} < 1 \text{ deg}$ ). (5) The system should allow for the integration of data from additional sensors, such as cameras or laser scanners.

The ability to include additional sensors to the system was – apart from the size and the weight constraint – the main reason for developing an own system instead of using a commercial unit with similar capabilities.

### 3.1 Georeferencing Unit

Fig. 2 shows the prototype version of the georeferencing unit. It measures 11.0 cm × 10.2 cm × 4.5 cm and has a weight of roughly 240 g without the GPS antennas.

The main positioning device is a Novatel OEM615 dual-frequency GPS board. Together with a radio link (XBee Pro 868) to a GPS master station it allows for a precise RTK GPS position determination (see section 4.1). Additionally, the unit contains a small low cost sin-

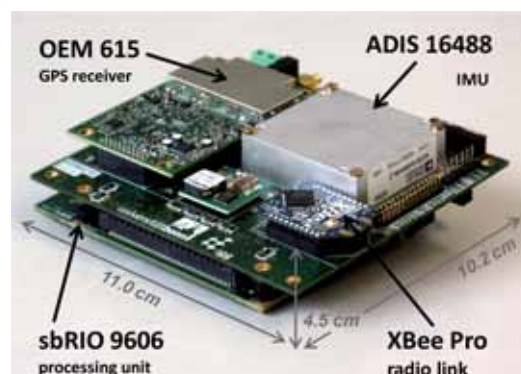
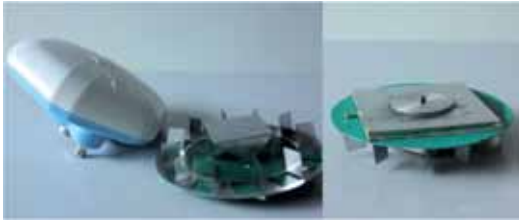


Fig. 2: The direct georeferencing unit.



**Fig. 3:** The original (left) and the dismantled (right) dual-frequency GPS antenna.

gle-frequency GPS receiver (u-blox LEA6T), which is mainly intended to be used for the heading determination (see section 4.2).

As a sensor for the attitude determination and for supporting the position estimation, the georeferencing unit contains a tactical grade MEMS IMU (Analog Devices ADIS16488), including three axis gyroscopes, accelerometers, magnetometers and a barometer.

Finally, the georeferencing unit also consists of a real-time processing unit (National Instruments sbRIO 9606), which is a re-configurable IO board, including a 400 MHz processor and an FPGA. The FPGA allows for a very fast and parallel communication with several serial interfaces. Afterwards, the pre-processed sensor data are provided to the 400 MHz processor via direct memory accesses (DMAs), avoiding delays and supporting the real-time capabilities of the system.

Fig. 4 shows the different sensors and the implemented interfaces of the direct georeferencing system.

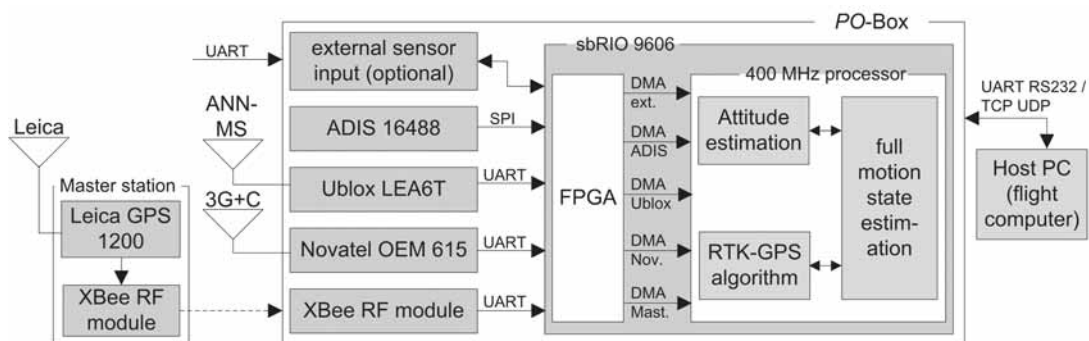


**Fig. 4:** Block diagram of the direct georeferencing system, which is named the *PO-Box* (3G+C = galileo, gps, glonass + compass, ADIS = Analog Devices (company), ANN MS = active gps antenna from Ublox, DMA = direct memory access, FPGA = field-programmable gate array, Nov. = Novatel, OEM = original equipment manufacturer, *PO* = Position and Orientation, sbRIO = single board remote input/output, SPI = serial peripheral interface, TCP UDP = transmission control protocol, user datagram protocol, UART = universal asynchronous receiver/transmitter, Ublox = swiss company, XBee RF = XBee radio frequency).

### 3.2 GPS Antennas

Preferably, a dual frequency GPS receiver is connected to a geodetic grade dual frequency GPS antenna. However, these antennas are usually too heavy for MAV applications. Therefore, we dismantled such an antenna (navXperience 3G+C, see Fig. 3). In this way the protective housing and the 5/8" screw thread in the bottom of the antenna could be omitted so that the weight of the antenna could be reduced from 350 g to 100 g.

Certainly, by dismantling the antenna, the external reference point was lost. Thus, the antenna had to be recalibrated in an anechoic chamber (ZEIMETZ & KUHLMANN 2010). By comparison to the original antenna the dismantling led to significant changes in the phase centre offset ( $\Delta_{up} \approx 4$  cm,  $\Delta_{north}$  and  $\Delta_{east} < 1$  mm) and in the phase centre variations ( $< 5$  mm).

As antenna for the single-frequency GPS receiver (LEA6T), a low-cost antenna from u-blox (ANN-MS) is mounted on the outer end of one of the riggers of the MAV (see Fig. 1). Together, both antennas form a short baseline on the MAV, which can be used for the attitude determination.

## 4 Software Development

The final goal of the algorithm development is the fusion of the GPS observations, the measurements from the IMU, the magnetometer and the barometer as well as information from the stereo camera systems in a tightly coupled approach. In doing so, precise and reliable positions and attitudes should be provided in real-time. In the current state of the development, the GPS based position estimation and the IMU / magnetometer based attitude estimation are separate, independent algorithms. Although this is not yet the final envisaged state, it already provides the full exterior orientation of the system. Furthermore, it is an excellent basis for future developments.

In the following, the basics of the RTK GPS algorithms and the concept of the attitude determination will be presented. All algorithms are developed in C++ and compiled as dynamic link libraries (dll), which are then imported into the real time operating system running on the 400 MHz processor. The programming of the FPGA and the 400 MHz processor is done using LabView.

### 4.1 The RTK GPS Software

RTK GPS is the most suitable procedure to obtain kinematic GPS positions with cm-accuracies in real-time.

The RTK GPS algorithms used on the georeferencing system, are in-house developed although there are commercial (even for the Novatel OEM 615) and open source (RTKLIB, TAKASU & YASUDA 2009) RTK GPS solutions available.

The main reasons for developing an own RTK GPS software are: (1) The final goal of the algorithm development is a tightly-coupled GPS processing. The advantages of such an implementation are that the ambiguity resolution is getting faster and the cycle slips can be detected more robustly. In order to achieve this goal RTK GPS algorithms with its data management first have to be implemented. (2) In commercial software there is generally no access to the source code. Thus, adaptations according to special uses, e.g. modification of the motion model, are generally impossi-

ble. (3) In the development of a real-time system the implemented software has to meet the requirements of the operating system that is running on the real-time processing unit.

#### 4.1.1 The RTK GPS algorithms

The key to RTK GPS positioning is the ambiguity resolution, which is the process of resolving the unknown number of integer cycles. In order to achieve this, the RTK algorithm contains the following steps:

- float solution,
- integer ambiguity estimation,
- fixed solution.

The float solution is the step, where the ambiguities are first estimated as real values. This is done in an extended Kalman filter (EKF). In this filter the observation vector  $l$  consists of double-difference (DD) carrier phases  $\Phi_{RM}^{jk}$  and pseudoranges  $P_{RM}^{jk}$  on the GPS-L1 and the GPS-L2 frequency, to allow for an instantaneous ambiguity resolution.

$$l = \left[ \Phi_{RM,L1}^{1k} \dots \Phi_{RM,L1}^{mk} \Phi_{RM,L2}^{1k} \dots \Phi_{RM,L2}^{mk} \dots \right. \\ \left. P_{RM,L1}^{1k} \dots P_{RM,L1}^{mk} P_{RM,L2}^{1k} \dots P_{RM,L2}^{mk} \right]^T \quad (1)$$

Beside the rover position  $r_r$ , the state vector  $x_{SD}$  contains single-difference (SD) ambiguities  $N_{RM}^j$ :

$$x_{SD} = \left[ r_{R,x} \ r_{R,y} \ r_{R,z} \ N_{RM,L1}^1 \dots N_{RM,L1}^n \dots \right. \\ \left. N_{RM,L2}^1 \dots N_{RM,L2}^n \right]^T \quad (2)$$

The reason for estimating SD instead of DD ambiguities is to avoid the hand over problem that would arise for DD ambiguities, when the reference satellite changes (TAKASU & YASUDA 2009).

The chosen motion model is a random walk model, which is a simple but efficient model, when no additional information is available. Due to the use of own RTK GPS algorithms the process noise of the positions can be adopted according to the planned motions, which are known from the flight planning. In contrast, the ambiguities are assumed to be constant. This is why the process noise of the ambiguity parameters is set to a very small value ( $\sigma_{amb} = 1 \cdot 10^{-4}$  cycles).

In the measurement noise a distinction must be made between the carrier phases and the pseudoranges. Therefore, a factor  $f$  is used, which is 1 for carrier phases and 100 for pseudoranges:

$$\sigma_{\varphi,P}^2 = 2 \cdot f^2 \cdot (a^2 + (b / \sin el)^2) \quad (3)$$

This model is split into a constant and an elevation ( $el$ ) dependent part. The author's experience is that  $a = 2$  mm and  $b = 2$  mm lead to the best results for the MAV applications.

Once the ambiguities are estimated in the float solution the integer ambiguity estimation follows. In this step the float ambiguities and their covariance matrix are used to search for the integer ambiguities. This is done by the modified least squares ambiguity decorrelation adjustment (MLAMBDA) (CHANG et al. 2005). After the ambiguity search a decision must be made, if the resulting set of ambiguities can be accepted or if it has to be rejected, since there is the risk of incorrectly fixing the ambiguities. This decision is made by the simple ratio test (VERHAGEN & TEUNISSEN 2006). Finally, in case ambiguities could be fixed successfully, the fixed solution can be computed, leading to rover positions with cm-accuracy.

More details to the implemented RTK GPS algorithms can be found in ELING et al. (2014).

#### 4.1.2 Task scheduling

The RTK GPS processing is realized in two parallel tasks, the master task and the rover

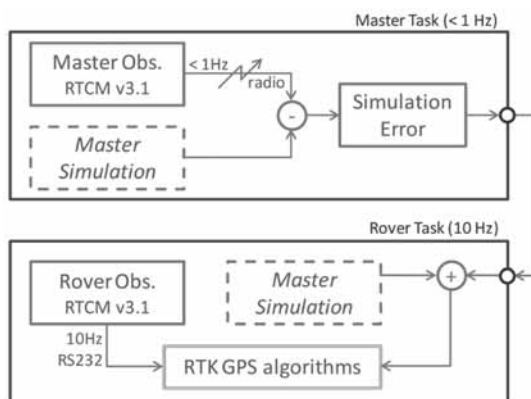


**Fig. 5:** The rover and the master task as they are realized on the 400 MHz processor (RTCM = Radio Technical Commission for Maritime Services).

task (Fig. 5). The actual position determination is carried out in the rover task with a rate of 10 Hz. Since the master station remains on ground, the master observations have to be transmitted via radio to the direct georeferencing system with a rate of 1 Hz. In order to be less dependent on the potentially unreliable master data transmission and the lower sampling rate, not the actual but simulated master observations are used for the position determination. The true master observations are only used to update the simulation error in the master task. The simulation error has to be applied to correct the simulation results in the rover task. There, the assumption is made, that the simulation error keeps constant over a short time. With this method, a position accuracy better than 10 cm can still be maintained in most cases, even when the link to the master station is interrupted for about 30 s.

#### 4.2 Attitude Determination

The georeferencing unit includes several sensors, which can be used for the attitude determination: gyroscopes, accelerometers, magnetometers, an onboard GPS baseline, RTK GPS and stereo camera pairs. Even if the stereo camera pairs are not directly connected to the georeferencing unit they also provide precise relative orientation information (SCHNEIDER et al. 2013).

##### 4.2.1 The attitude filter

Only using the angular rates, the accelerations and the magnetic field observations would generally deliver enough information to determine all three attitude angles (roll, pitch, yaw) of the MAV. However, ferromagnetic material on the MAV and the high electric currents of the rotors lead to significant distortions of the magnetometer during a flight, even if the magnetometer is well calibrated (CARUSO 2000). Hence, in order to avoid the need for the magnetometer readings as much as possible, the onboard GPS baseline has been established on the MAV.

In the current status of the implementation, the attitude determination is realized in a quaternion based EKF, e.g. SABATINI (2006),

which is currently still decoupled from the position determination. The state vector  $\mathbf{x}_{Att}$  contains the following parameters:

$$\mathbf{x}_{Att} = [q_0 \ q_1 \ q_2 \ q_3 \ \Delta\omega_x \ \Delta\omega_y \ \Delta\omega_z \ a_{r,x} \ a_{r,y} \ a_{r,z}]^T. \quad (4)$$

Thus, beside a quaternion  $\mathbf{q}$ , representing the attitude, and the gyro bias  $\Delta\boldsymbol{\omega}$ , also the translational accelerations  $\mathbf{a}_r$  are estimated, to allow for a separation of the dynamics of the MAV from the gravitation vector.

In the system dynamics model the bias corrected angular rates are used to predict the quaternion vector  $\mathbf{q}$ . The prediction of the translational accelerations  $\mathbf{a}_r$  is based on a Gauss-Markov process, assuming that they are tending to zero.

Finally, the measurement vector  $\mathbf{l}_{Att}$  includes the magnetic field observations  $\mathbf{m}$ , the accelerations  $\mathbf{a}$  and the onboard GPS baseline vector  $\mathbf{r}$ .

$$\mathbf{l}_{Att} = [m_x \ m_y \ m_z \ a_x \ a_y \ a_z \ r_E \ r_N \ r_U]^T \quad (5)$$

#### 4.2.2 The ambiguity resolution

The difficulty in using the onboard GPS baseline is that only single-frequency GPS observations are available for their determination and usually, the time to fix the ambiguities of single frequency GPS data takes a few minutes (ODIJK et al. 2007). To improve this, the attitude determination is performed in three steps: (1) an approximate attitude solution, based on the magnetometer and the accelerometer readings, (2) the ambiguity resolution and (3) the final attitude determination, also including the baseline parameters in the measurement model.

Hence, the idea is to use an approximate attitude solution to shrink the search space of possible ambiguity candidates in the integer ambiguity estimation (ELING et al. 2013). In doing so, the ambiguity resolution can be improved significantly, with the result that the ambiguities can mostly already be fixed within the first epoch.

## 5 System Calibration

In order to correctly fuse all sensory information and to provide a precise georeference of the taken images, the relative positions and attitudes of all sensors within the system have to be known. Although it is in principle possible to determine these values by sophisticated calibration procedures, we decided to measure them using a high resolution laser scanner.

The used measurement equipment for the system calibration consists of a 3D laser scanning portable coordinate-measuring machine arm (Romer Infinite 2.0) and a 3D laser scanner (Perceptron ScanWorks V5). Together, this equipment leads to accuracies of  $\sigma \leq 45 \mu\text{m}$  for single points. One of the resulting point clouds is shown in Fig. 6. After the scanning, the translations and rotations between the georeferencing sensors and the high-resolution camera were measured in the point-cloud by 3D-modeling of the different sensors. We estimate that the accuracy of this method is below one millimeter for the translations and below some tenth of one degree for the rotations.

Of course, even if the sensors are firmly fixed to the platform, slight changes of the calibration parameters during a flight cannot be excluded. Furthermore, the IMU axes directions, which are best possibly mechanically aligned with the body frame axes, cannot be calibrated precisely via the laserscanner approach. Thus, the full system calibration still can be improved. Currently, the authors are working on the realization of a calibration field, where ground control points allow for the determination of the calibration parameters during a flight.

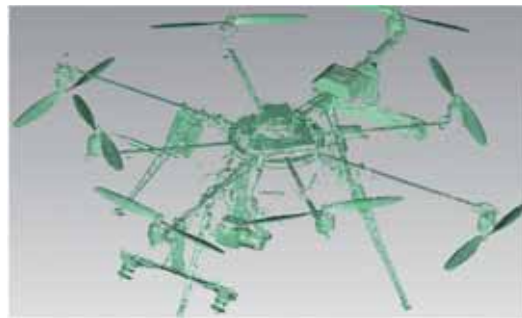


**Fig. 6:** Point-cloud of a laser scan, which has been used for the system calibration.

The interior orientation of the camera has been determined via a laboratory test field calibration. By means of this calibration the calibrated focal length, the principal point, and the non-linear distortion of the camera were estimated.

## 6 Results

By comparing the GPS-positions of the georeferencing system with the results of other recognized GPS software packages, e.g. RTKLIB and Leica Geo Office, the correctness of the implemented RTK GPS algorithms could already be confirmed (ELING et al. 2014). This is of course only an evaluation of the correctness of the implementation, as the same data are used. At the moment, we do not have an independent check on the absolute accuracy of the direct georeferencing system. However, we can use the results of a free photogrammetric bundle adjustment (BA), which is independent of ground control points, to evaluate the form of the trajectory. The direct georeferencing trajectory, both in the translation and the rotation, should only differ by a spatial similarity transformation from the BA trajectory.

For the comparison to a BA trajectory, the following steps were performed:

- time synchronized image and position/attitude data collection during a MAV flight,
- photogrammetric BA on the collected images,
- 7-parameter Helmert transformation between the GPS and the camera coordinates,
- position and attitude difference determination.

In Fig. 7 the GPS track of the manually flown test flight is shown (red line). During the flight the GPS ambiguities could be fixed for all epochs. From the starting point the MAV was first navigated to a building. Afterwards, in the green marked area, images of the façade of the building on the right were taken at a rate of 1 Hz.

Finally, the images were orientated via a photogrammetric BA. Since the flight path along the building did not follow a regular pattern, the image overlap was uneven, but the geometric point distribution was good. The re-



**Fig. 7:** The RTK-GPS positions during the test flight. Images were taken in the image acquisition area to observe the building on the right.

sulting standard deviations of the BA translations and rotations relative to the first camera position, which defines the photogrammetric coordinate frame, are better than 4 mm and 0.02 deg for all epochs.

For comparison of the BA positions with the direct georeferencing positions a 7-parameter Helmert transformation between the GPS and the camera positions was performed, considering the system calibration parameters.

In Fig. 8 the differences between the camera positions, determined via GPS and via BA are shown. Thus, the differences of the trajectories are mostly less than  $\pm 5$  cm in all components. A mean value and a standard deviation can also be calculated from the differences. The mean values are zero and the standard deviations are 1.4 cm – 2.3 cm. Hence, the precisions of the positions meet the requirements of 1 cm – 3 cm. Please note that the GNSS measurement conditions were challenging during this test flight, since the MAV flew close to trees and a building.

For the attitude evaluation the BA results, representing the rotations from the camera- to the photogrammetric-frame  $R_{Cam}^{Photo}$ , have to be transformed into rotations from the body- to the navigation frame  $R_{Body}^{Nav}$ , which then should match the output of the direct georeferencing system:

$$R_{Body}^{Nav}(t) = R_{Photo}^{Nav} \cdot R_{Cam}^{Photo}(t) \cdot R_{Body}^{Cam} \quad (6)$$

Therefore, the system calibration rotation matrix  $R_{Body}^{Cam}$  and the rotation matrix from the 7-parameter Helmert transformation  $R_{Photo}^{Nav}$

have to be applied. The only time-dependent variable on the right side of (6) is the result of the BA ( $R_{Cam}^{Photo}(t)$ ).

The differences between the direct georeferencing system and the camera attitudes are presented in Fig. 9. Here, two different time series are shown for each attitude angle: The blue dots represent the differences to the approximate attitudes (see section 4.2), which were determined only using the IMU and the magnetometer observations and the red dots represent the differences to the attitudes based on the IMU, the magnetometer and the on-board GPS baseline.

Since the magnetometer is the only sensor in the “IMU+magnetometer” combination, providing yaw-information, significant deviations are visible in the “IMU+magnetometer”-

yaw-angles. These deviations, looking like a trend here, result from a distortion of the magnetometer readings. Adding the GPS baseline improves the yaw-results enormously. Thus, the standard deviations of the “IMU+magnetometer+GPS” differences are < 1 deg for all attitude components. However, the mean value of the pitch angle is approximately 1 deg. Thus, there seems to be a remaining offset in the calibration, which has to be reviewed.

### 7 Conclusions and Future Work

In this contribution a newly developed direct georeferencing system has been presented. The system combines two GPS receivers, in-

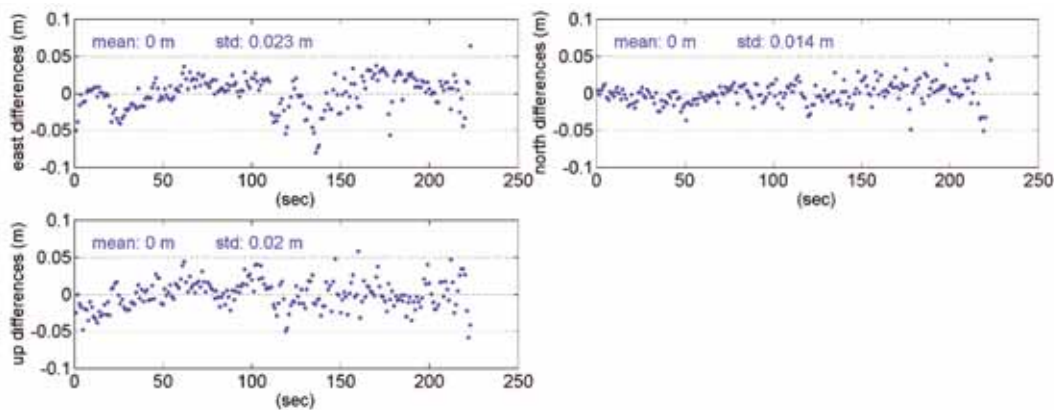


Fig. 8: Differences between the camera positions, determined via GPS and via BA.

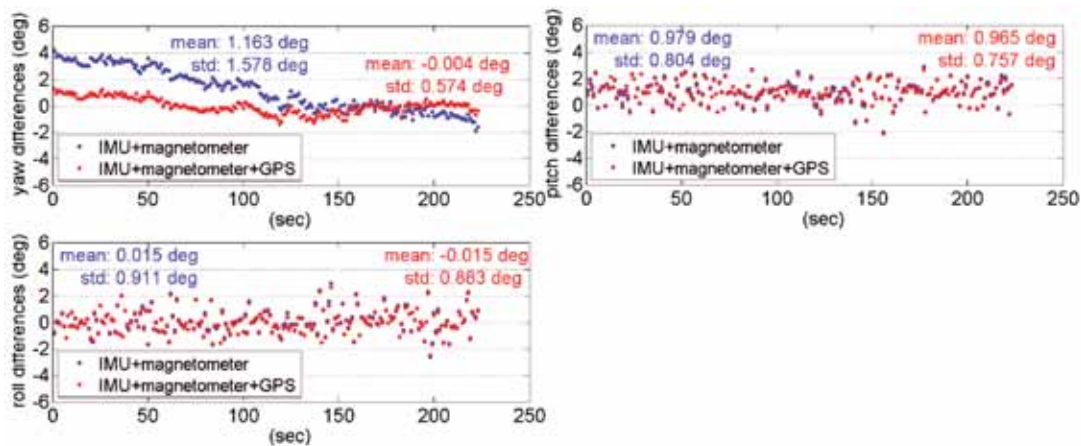


Fig. 9: Differences between the attitudes from the bundle adjustment and the attitudes from the georeferencing system.

ertial sensors, magnetic field sensors, a barometer and a real-time processing unit. The main advantages of the system are that (1) it is lightweight, (2) it is real time capable, (3) it leads to accurate results and (4) it is able to bridge gaps of single sensors. In the current state the system is already providing positions and attitudes in real-time with accuracies in the order of a few centimetres and degrees. However, the intended robustness of the full motion state estimation, especially in non-ideal GPS conditions, has not yet been achieved.

The authors are currently working on the implementation of tightly coupled GPS algorithms. In such a full motion state filter the positions will then also have a positive impact on the attitude determination. Furthermore, the optical flow information from the stereo cameras still has to be integrated in the position and attitude determination. A challenge of this development will be the consideration of the latency time of the position and attitude changes from the camera systems with respect to the GPS and IMU data.

## Acknowledgements

This work was funded by the DFG (Deutsche Forschungsgemeinschaft) under the project number 1505 “Mapping on Demand”. The authors wish to express their gratitude for that. Furthermore, the authors would like to thank JOHANNES SCHNEIDER and THOMAS LÄBE (Department of Photogrammetry, University of Bonn) for providing the results of the bundle adjustment.

## References

- BÄUMKER, M., PRZYBILLA, H.-J. & ZURHORST, A., 2013: Enhancements in UAV flight control and sensor orientation. – The International Archives of Photogrammetry, Remote Sensing and Spatial Information Science **XL-1/W2**: 33–38.
- BLÁHA, M., EISENBEISS, H., GRIMM, D. & LIMPACH, P., 2011: Direct Georeferencing of UAVs. – The International Archives of Photogrammetry, Remote Sensing and Spatial Information Science **XL-1/W2**: 1–6.
- CARUSO, M.J., 2000: Applications of magnetic field sensor for low cost compass systems. – IEEE Position, Location and Navigation Symposium: 177–184.
- CHANG, X.-W., YANG, X. & ZHOU, T., 2005: Mlambda: a modified lambda method for integer least-squares estimation. – Journal of Geodesy **79**: 552–565.
- EISENBEISS, H., LAMBERS, K. & SAUERBIER, M., 2005: Photogrammetric recording of the archaeological site of pinchango alto (palpa, peru) using a mini helicopter (UAV). – The World is in Your Eyes – 33rd CAA Conference.
- EISENBEISS, H., 2009: UAV Photogrammetry. – Dissertation, ETH Zürich, No. 18515.
- ELING, C., ZEIMETZ, P. & KUHLMANN, H., 2013: Development of an instantaneous GNSS/MEMS attitude determination system. – GPS Solution **17**: 129–138.
- ELING, C., KLINGBEIL, L. & KUHLMANN, H., 2014: Development of an RTK-GPS system for precise real-time positioning of lightweight UAVs. – Ingenieurvermessungskurs **2014**: 111–123, Zürich, Schweiz.
- HEIPKE, C., JACOBSEN, K. & WEGMANN, H., 2002: Integrated Sensor Orientation – Test report and workshop proceedings. – OEEPE Official Publication 43, Frankfurt/Main.
- HOLZ, D., NIEUWENHUISEN, M., DROESCHEL, D., SCHREIBER, M. & BEHNKE, S., 2013: Towards multimodal omnidirectional obstacle detection for autonomous unmanned aerial vehicles. – The International Archives of Photogrammetry, Remote Sensing and Spatial Information Science **XL-1/W2**: 201–206.
- LOCH-DEHBI, S., DEHBI, Y. & PLÜMER, L., 2013: Stochastic reasoning for UAV supported reconstruction of 3D building models. – The International Archives of Photogrammetry, Remote Sensing and Spatial Information Science **XL-1/W2**: 257–261.
- MERZ, T. & KENDOUL, F., 2011: Beyond visual range obstacle avoidance and infrastructure inspection by an autonomous helicopter. – IEEE/RSJ International Conference on Intelligent Robots and Systems, IROS 2011, San Francisco, USA.
- NIEUWENHUISEN, M., SCHADLER, M. & BEHNKE, S., 2013: Predictive potential field based collision avoidance for multicopters. – The International Archives of Photogrammetry, Remote Sensing and Spatial Information Science **XL-1/W2**: 293–298.
- ODIJK, D., TRAUOGOTT, J., SACHS, G., MONTENBRUCK, O. & TIBERIUS, C., 2007: Two precision GPS approaches applied to kinematic raw measurements of miniaturized L1 receivers. – 20th International Technical Meeting of the Satellite Division of the Institute of Navigation ION GNSS **2007**: 827–838.

- REHAK, M., MABILLARD, R. & SKALOU, J., 2014: A Micro Aerial Vehicle with Precise Position and Attitude Sensors. – PFG – Photogrammetrie, Fernerkundung, Geoinformation **2014** (4): 239–251.
- RIEKE, M., FOERSTER, T., GEIPEL, J. & PRINZ, T., 2011: Highprecision positioning and real-time data processing of UAV systems. – International Archives of the Photogrammetry, Remote Sensing and Spatial Information Sciences **XXXVIII** (1-C22).
- SABATINI, A.M., 2006: Quaternion-based extended Kalman filter for determining orientation by inertial and magnetic sensing. – IEEE Transactions on Biomedical **E 53** (7): 1346–1356.
- SCHNEIDER, J., LÄBE, T. & FÖRSTNER, W., 2013: Incremental real-time bundle adjustment for multi-camera systems with points at infinity. – The International Archives of Photogrammetry, Remote Sensing and Spatial Information Science **XL-1/W2**: 355–360.
- SCHWARZ, K.P., CHAPMAN, M., CANNON, M. & GONG, P., 1993: An integrated INS/GPS approach to the georeferencing of remotely sensed data. – PE&RS **49** (11): 1667–1674.
- SKALOU, J., 1999: Optimizing Georeferencing of Airborne Survey Systems by INS/DGPS. – PhD thesis, University of Calgary, Canada.
- STEMPFHUBER, W. & BUCHHOLZ, M., 2011: A precise, low-cost RTK GNSS system for UAV applications. – International Archives of the Photogrammetry, Remote Sensing and Spatial Information Sciences **XXXVIII** (1-C22): 289–293.
- TAKASU, T. & YASUDA, A., 2009: Development of the low-cost RTK-GPS receiver with an open source program package RTKlib. – International Symposium on GPS/GNSS, Jeju, South Korea.
- VERHAGEN, S. & TEUNISSEN, P.J.G., 2006: New Global Navigation Satellite System Ambiguity Resolution Method Compared to Existing Approaches. – Journal of Guidance, Control, and Dynamics **29** (4): 981–991.
- XIANG, H. & TIAN, L., 2011: Development of a low-cost agriculture remote sensing system based on an autonomous unmanned aerial vehicle (UAV). – Biosystems Engineering **108**: 174–190.
- YOO, C. & AHN, I., 2003: Low cost GPS/INS sensor fusion system for UAV navigation. – 22nd Digital Avionics Systems Conference **2**: 8.A.1-1 – 8.A.1-9.
- ZEIMETZ, P. & KUHLMANN, H., 2010: Validation of the laboratory calibration of geodetic antennae based on GPS measurements. – FIG Working Week, Sydney, Australia.

## Address of the Authors:

CHRISTIAN ELING, LASSE KLINGBEIL, MARKUS WIELAND & HEINER KUHLMANN, Institut für Geodäsie und Geoinformation, Rheinische Friedrich-Wilhelms-Universität Bonn, Nussallee 17, 53115 Bonn, Tel: +49 228 73 3565, Fax: +49 228 73 2988, e-mail: {c.eling}{l.klingbeil}{m.wieland}@igg.uni-bonn.de, heiner.kuhlmann@uni-bonn.de

Manuskript eingereicht: Oktober 2013

Angenommen: April 2014





# A Micro Aerial Vehicle with Precise Position and Attitude Sensors

MARTIN REHAK, ROMAIN MABILLARD & JAN SKALOUD, Lausanne, Switzerland

**Keywords:** UAV, MAV, integrated sensor orientation, GNSS/INS

**Summary:** This study shows the potential of navigation technologies in the field of position and orientation determination on a micro aerial vehicle (MAV), which weight does not exceed 5 kg. Although the MAV systems feature high flexibility and capability of flying into areas that are inhospitable or inaccessible to humans, the lack of precision in positioning and attitude estimation on-board decreases the gained value of the captured imagery. This limits their mode of operation to indirect georeferencing. This paper presents the development of a low cost MAV with navigation-sensor payload that shall assure a position and attitude control with accuracy from which either direct or integrated sensor orientation can benefit. After describing the hardware configuration and the synchronization of all measurements we present a case study that evaluates the performance of the positioning component and its application on integrated sensor orientation without ground control. There we show that thanks to the implementation of a multi-frequency, low power GNSS receiver, the system can potentially attain the mapping characteristics of much larger platforms flown on man-operated carriers while keeping the sensor size and weight suitable for MAV operations. The attitude accuracy of the developed board hosting several MEMS-IMUs is evaluated dynamically on a terrestrial vehicle using a reference (navigation grade) INS. Although this method offers continuous evaluation of the orientation accuracy and the obtained results are satisfactory with respect to the foreseen operations, this performance remains to be confirmed in a flight.

**Zusammenfassung:** *Ein MAV (Micro Aerial Vehicle) mit genauen Sensoren für die Positions- und Neigungsbestimmung.* Diese Untersuchung zeigt das Potenzial von Navigationssystemen für die Bestimmung der äußeren Orientierung von MAVs (Micro Aerial Vehicles) bis zu einem Gewicht von 5 kg. Die fehlende hochgenaue direkte Bestimmung der Orientierungsdaten der Bilder relativiert oft die Stärken von MAVs, z. B. ein Bildflug in Gebieten, die für den Menschen unzugänglich sind. Das bedeutet, dass immer eine indirekte Georeferenzierung, also die Bildtriangulation, erforderlich ist. In dem vorliegenden Artikel wird die Entwicklung einer low-cost Navigationseinheit für die direkte Georeferenzierung von MAVs vorgestellt. Nach der Beschreibung der Hardware-Konfiguration und der Methode zur Synchronisation aller Komponenten wird eine Fallstudie vorgestellt, die die Leistungsfähigkeit der Methode unter Beweis stellt und dabei die Ergebnisse der direkten Georeferenzierung an bekannten Bodenpunkten prüft. Dabei zeigen die Autoren, dass der Multifrequenz GNSS-Empfänger mit geringer Leistungsaufnahme bezüglich der Genauigkeit mit Systemen, die auf bemannten Flugzeugen verwendet werden, vergleichbar ist. Die Genauigkeit der vom Autorenteam entwickelten Leiterplatte für die Neigungsmessung wurde durch eine 20-minütige Testfahrt mit einem Auto geprüft.

## 1 Introduction

### 1.1 Problem Formulation

Low-cost and low-weight unmanned aerial vehicle (UAV) systems with imaging capa-

bility have enjoyed a rapid development over the past years and are increasingly deployed as carriers for mapping purposes. They present a well-established tool for local-area remote sensing in the fields of agriculture, forestry, mining and hydrology as well as in the

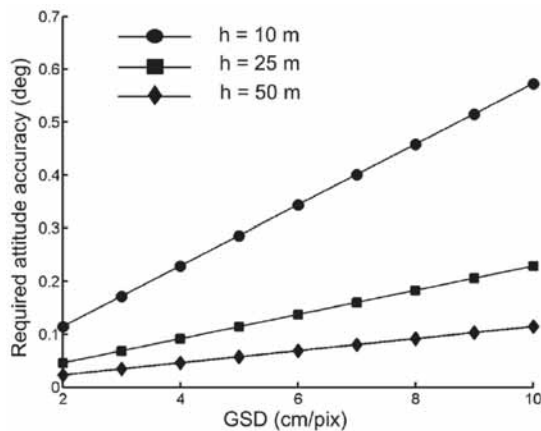


**Fig. 1:** Approximate requirements on attitude accuracy for direct sensor orientation on MAV at different flying heights above ground.

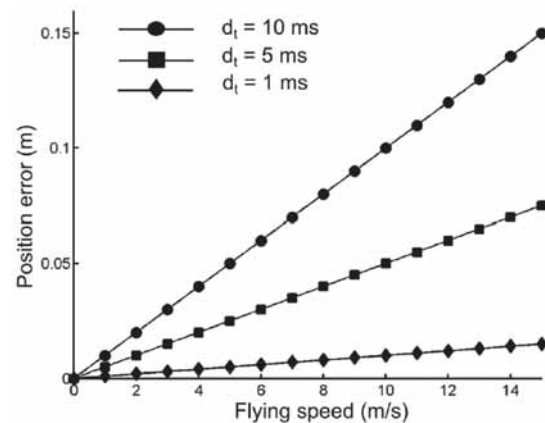


**Fig. 2:** Influence of synchronization errors  $d_t$  on aerial position determination as a function of MAV speed.

scientific research (REMONDINO et al. 2011). Although these systems allow a new way of data collection in the field of geomatics, they inherit an old, i.e. indirect, approach to sensor/image orientation. Indeed, most of the commercially available micro aerial vehicles (MAVs), e.g. AIBOTIX 2013, SENSEFLY 2013, TRIMBLE 2013, carry consumer-market non-metric cameras and single-frequency GPS receivers without precise carrier phase observations providing position accuracy at level of several metres in optimal conditions. That is indeed insufficient for large scale mapping projects and cadastral surveying for which accuracy at a 2–5 centimetre-level is needed. Furthermore the quality of the employed inertial sensor, often part of a low-cost autopilot unit, is not sufficient for accurate attitude determination at a level of  $\sigma_{att} = 0.01 \text{ deg} - 0.1 \text{ deg}$  (Fig. 1).

Hence, missions with the need of accurate mapping require image acquisition in a block-structure with large forward and side overlaps, the existence of possibly many ground-control points (GCPs) as well as contrast in the surface texture. Although single-strip operations are theoretically possible, the requirement on the number and distribution of GCPs makes them impractical. Overall, the need of ground operations limits the mapping productivity of MAVs. Although the orientation requirements have a very wide range and the overall accuracy on the ground is dependent on many aspects, the acceptable attitude error is propor-

tional to the ground sampling distance (GSD) and inversely proportional to the flying height above ground as shown in Fig. 1. On the other hand, the requirement on aerial position control is directly related to GSD. The state-of-the-art of kinematic carrier-phase differential positioning is situated at 2 cm – 5 cm noise level. Apart from the navigation solution based on global navigation satellite systems (GNSS) and inertial measurement systems (INS), the results are also influenced by the imaging sensor quality and image resolution (NASSAR & EL-SHEIMY 2005).

The quality of the GNSS/INS solution is furthermore influenced by the precision of the synchronization with the imaging sensor. Fig. 2 shows the influence of given synchronization errors on position for different flying speeds.

The problem of determining exterior orientation parameters by direct observation of camera position and attitude has been extensively researched in the past (e.g. SKALOUD 1999, MOSTAFA et al. 2001, SKALOUD et al. 1996, COLOMINA 1999). However, only recent studies discuss this problem in the context of MAVs, e.g. EUGSTER & NEBIKER 2008, BLÁHA et al. 2011, BÄUMKER et al. 2011, PFEIFER et al. 2012, BÄUMKER et al. 2013, ELING et al. 2014.

In principle, the following conditions must be met for the correct integration of position and attitude sensors (SKALOUD 1999): 1) The position and orientation offsets between

a GNSS antenna, inertial measurement unit (IMU) and a sensor, i.e. a camera, a laser scanner etc., must be determined, 2) these offsets must remain constant during each mission and 3) the time stamping of all observations must be achieved with sufficient accuracy. To carry out these conditions, we have to pay special attention on the implementation of each system component and their mutual interconnection. Only a precise integration of all components ensures valuable results.

## 1.2 Objectives

In this paper we propose a GNSS/INS sensor payload for the sake of obtaining precise sensor orientation on a multi-rotor MAV. Although the current trend is to use the indirect approach, we can see a gradual rise up in the field of advanced sensor integration into larger UAV platforms, e.g. SWISS DRONE (2013). In a certain sense this evolution follows the classical airborne photogrammetric development (COLOMINA & MOLINA 2014) to which direct sensor orientation was conceptually introduced in the early nineties (SCHWARZ et al. 1993) together with the first experimental confirmation in photogrammetry (SKALOUD et al. 1994). The progress in the field of miniaturization of the inertial technology as well as GNSS receivers and antennae allows in principle to create a small-integrated system from off-the-shelf components. Nevertheless, the hardware implementation needs to be combined with state-of-the-art processing to fulfil the accuracy requirements for direct or integrated sensor orientation.

Our ultimate goal is to integrate advanced navigation devices, i.e. a multi-frequency/constellation GNSS receiver and redundant MEMS IMU to improve the mapping accuracy while minimizing the number of GCPs and enhancing the flying capability of a custom made MAV. In this paper we focus on the MAV development, physical integration, synchronization and quality evaluation of the navigation components. During practical tests we evaluate the accuracy of GNSS-base positions for direct determination of camera projection centres. We also assess the quality of attitude determination on board of a ground

vehicle using a reference IMU. The following part describes the development of the new MAV with an open-source autopilot. The third section concentrates on the sensor integration and implementation on the developed platform. Special attention is given to the parameter estimation of the redundant IMU, its calibration and integration on the MAV. The problem of camera synchronization is described and a method of the shutter-lag determination is presented. The fourth part is devoted to a case study where we describe the first results from platform operation. Finally, the last part draws conclusions and gives recommendations for future investigation.

## 2 System Design

The UAV platform market is getting more favourable every year in terms of price and performance. Manufactures produce sophisticated platforms, autopilots and camera gimbals. Nevertheless, the design is often closed and does not allow access or control of vital system components. Also the platform cannot be easily extended with additional sensors for the precise sensor orientation or for improving its capacity in autonomous navigation in case of interference or a denial of GNSS service. For these reasons we decided to build a new platform that shall be better suited for demanding mapping tasks.

### 2.1 UAV Platform

The custom design of a vertical take-off and landing (VTOL) MAV allows mounting the necessary devices needed to perform modern photogrammetry. The platform is equipped with eight brushless motors to enhance the payload capacity and to increase the redundancy in case of engine failure. The UAV accommodates appropriate sensors and an autopilot to perform stabilized and autonomous flights. The latter is based on a do-it-yourself project intensively developed during past years by the community of engineers and amateurs called Ardupilot APM 2.6 (3DROBOTICS 2013). This autopilot unit includes MEMS gyroscopes and accelerometers, a 3-axis mag-

netic sensor, a barometric pressure sensor and a single frequency low-cost GPS receiver. The cooperation of these navigation components allows horizontally and vertically stabilized positioning of the system as well as position hold, return to the launch site or other features including mission flights according to pre-planned trajectories.

The frame consists of carbon tubes and glass fibre base plates (Fig. 3). Special attention is given to the camera mount. This very light servo-powered gyro-stabilized camera holder keeps the equipment in level (or in selected inclination) during the flight. At the same time it dampens the vibrations from the engines. The camera can be tilted remotely to a desired angle along its horizontal axis. Fig. 4 shows the schematic location of the navigation components on the sensor mount.

The system is powered by high capacity lithium polymer (LiPo) batteries. Depending on the application and especially on the payload (1 kg – 1.5 kg), the flight times vary from 10 to 15 minutes. The system with all the equipment and additional sensors weighs 4.8 kg. The on-board control segment is an embedded micro-PC with an Atom processor connected to the Arduino autopilot. In its current configuration the PC governs the process of data acquisition and sets up the Ardupilot.

A significant challenge associated with MAV is their safety. To enhance the safety either for people and public infrastructure on the ground or also for the MAV itself, the multi-rotor is optionally equipped with a parachute to face emergency situations. The parachute is currently deployed manually by the operator. As a consequence of this additional payload of



**Fig. 3:** Octocopter with equipment (size: 80 cm in diameter).

240 grams, the flight times lower to approximately 8 minutes. Its functionality was tested during several field tests and the minimal flying altitude for a correct deployment was empirically estimated to be about 40 m.

The selected coaxial concept, two engines on each arm of the multi-rotor, has its specific advantages and disadvantages. Tab. 1 shows the basic characteristic of such a design (MULTIROTOR FORUM 2013).

In manual mode the MAV helicopter can be operated by one pilot or as cooperation between two operators: one pilot and a second person responsible for the data acquisition. The system structure is universal as it can be (relatively easily) modified into a version with

**Tab. 1:** Advantages and disadvantages of a coaxial configuration.

+ Higher redundancy
+ Better orientation for a pilot
+ Compactness
+ More agile
+ Wider field of view for a camera
+ Better response to wind gusts
- Efficiency loss 15% – 30%
- Slightly worse stability

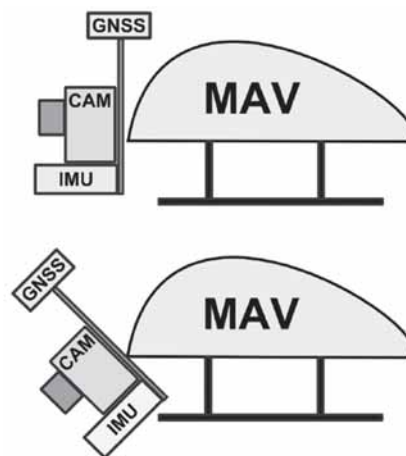


**Fig. 4:** Schematic sketch of the stabilized sensor mount for two distinct tilting angles.

only four motors or because the motors can be replaced by more powerful engines to increase the overall payload capacity.

## 2.2 Optical Sensor

The chosen optical sensor is the Sony NEX-5 camera. The quality of this mirror-less camera is comparable with a SLR camera despite being considerably smaller (only  $111 \times 59 \times 38 \text{ mm}^3$ ) and lighter (210 g without lens). These properties make it highly suitable for MAV platforms. The camera is equipped with a 16 mm fixed Sony lens, which has a reasonable optical quality given its size and weight and offers sufficient stability of the IO parameters through a mission. The camera is modified for better performance and integration into the MAV system. The on-board video-processing segment procures a digital to analogue conversion, video streaming and on-screen-display information of the current camera state as well as the telemetry data from the autopilot. The servo signal emitter triggers the camera shutter via an infra-red (IR) diode and a custom modification of hardware described in section 3.1 eliminates existing shutter lag and enables precise time synchronization with other navigation components. These modifications together with the external power supply convert this low-cost camera to a serious photogrammetric tool.

## 2.3 Precise Positioning

We employ a geodetic-grade multi-frequency and multi-constellation GPS/Glonass/Galileo OEM receiver (JAVAD 2013) with an appropriate antenna, RTK capability and 10 Hz sampling frequency. A similar setup is used as a

base station for differential processing. The position of the MAV is determined in post-processing. However, in its current state it is ready for RTK solution and for further integration with the embedded PC and IMU.

## 2.4 Inertial Measurement Unit

Within a scope of this study we employ the in-house developed FPGA-board (Field-Programmable Gate Arrays) called Gecko4Nav comprising of four MEMS IMU chips, all precisely synchronized to the GPS time-reference (KLUTER 2012). The Gecko4Nav contains two main components. The FPGA board handling the synchronization and data flow is connected to the state-of-the-art custom sensor board, equipped with various types of sensors. The main components are four NavChips IMUs that are software-combined to a redundant IMU (R-IMU). The performance characteristics for each sensor type provided by the manufacturers are shown in Tab. 2. The acquisition and control of the measurements are performed by the on-board firmware, which also governs the IMU sampling frequency. The latter can be selected by the user in the range from 250 to 500 Hz.

Dynamics encountered during the flight influence the behaviour of sensor errors. More specifically, its noise level may vary in time. Although such variations are not known a priori, the noise-level can be monitored on board thanks to multiple inertial sensors that are experiencing the same conditions. Indeed, the R-IMUs configuration improves the navigation performance on several levels (WAEGLI et al. 2010). First, it allows estimating the level of sensor noise directly from the data, which provides a correct view on the reality especially in a vibrating environment. Second, the noise

**Tab. 2:** Stochastic characteristics of the inertial sensors (INTERSENSE 2013).

Sensor performance parameters	Gyroscopes	Accelerometers
In-run bias stability	10°/hr	0.05 mg
Scale factor	0.1 %	0.06%
Angle random walk	0.18°/√hr	0.03 m/s/√hr
Noise density	0.003°/s/√Hz	50 μg/√Hz

level of the overall system can be reduced by weighted combinations or mitigated directly in the navigation filter. Third, defective sensors can be detected and isolated via a Fault Detection and Isolation procedure (GUERRIER et al. 2011). Finally, the overall performance of an R-IMU is superior to its individual inertial units.

### 3 Sensor Integration

#### 3.1 Time Synchronization of a low-cost Camera

Precise time tagging of the camera shutter within the GPS time-scale is the prerequisite for annotating the acquired imagery with the position and attitude information derived from the on-board GNSS/R-IMU. With MAVs, the common way of image synchronization with the position is through the correlation between image acquisition time stored in an EXIF file and the GPS log. This method is sufficient for the indirect approach to the sensor orientation where the GPS antenna positions enter only during the image pre-selection and/or as an initial approximation for the bundle adjustment. As the precise knowledge of the EO parameters is mandatory for direct or integrated sensor orientation, a considerably more accurate method of synchronization had to be conceived.

The camera delay, or so-called shutter lag, is a feature which affects all consumer grade cameras and has a significant influence on the precision of synchronization. When the shutter button is pressed or a triggering signal is

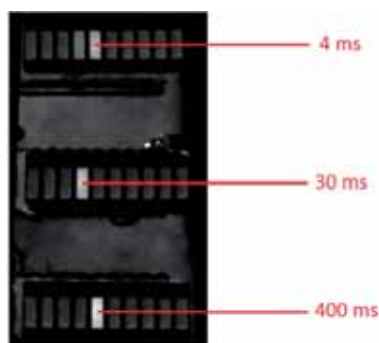


**Fig. 5:** Determination of a camera lag using LED bar-graphs.

sent, the camera may seem to take a photo instantly; however, there is a certain delay before a photo is actually taken. There are several ways to reduce this delay, but it is not possible to eliminate it completely. Even though the mission of the VTOL UAV can be programmed so that during the image acquisition the UAV hovers, the residual motion is not negligible. If the synchronization is not correct, this translates to an error in the parameters of the exterior orientation. Nevertheless, as long as the lag stays constant in time, it can be subtracted and thus corrected. A problem occurs with its instability or randomness.

In order to estimate the lag, we used a timer designed at the Czech Technical University (JON et al. 2013). It sends a trigger signal to the camera at an optional interval, e.g. every two seconds, and at the same time it runs graphical time counters with a resolution of one millisecond (Fig. 5). The camera takes images with these counters and an automatic evaluation based on image processing determines their values at time of exposure. After initial testing summarized in Tab. 3 we concluded that the residual variations are too large and therefore made additional modifications. The relatively large delay has its origin in the shutter construction, whereas the IR-shutter is responsible for its variance.

Several options are viable in terms of change/modification of the triggering system or signalization of the shutter opening. The presented method is based on processing of the camera flash signal, which the camera sends at the exact moment when the shutter opens. This signal is further processed and time-tagged. Thanks to this modification, we managed to eliminate the inaccuracy of the built-in IR shutter and attained the desired accuracy of image time tagging.

**Tab. 3:** Camera-lag statistics in a manual mode (STD = standard deviation).

Number of samples	88
Maximal delay	0.486 s
Minimal delay	0.406 s
Average delay	0.433 s
STD	0.013 s

The need of such modifications can be possibly eliminated by using industrial cameras, which are equipped with a sync port for the precise synchronization. On the other hand, these cameras are significantly more expensive and do not provide a comparable resolution for the same size, weight and price as the camera used here. In addition, an advantage of the Sony NEX-5 camera is the possibility of using various types of original or third party lenses with fixed focal length.

### 3.2 IMU Synchronization

The Gecko4Nav accommodates up to four NavChip IMUs on the same platform. The sampling of inertial observations at the same instance is a prerequisite for being able to exploit the benefits of redundancy and performance alleviation mentioned before. The Gecko4Nav features a synchronization module, which uses the pulse-per-second (PPS) signal issued by the GNSS receiver to adjust dynamically the drift within its crystal clock oscillator. This method ensures the continuity of the measurement procedure even if the PPS signal is lost. The synchronization was tested by placing the Gecko4Nav with the R-IMUs on top of a tactical grade inertial unit whose synchronization is known to be correct (SKALOUDE et al. 2010). The latter served as a reference, although only approximate alignment with respect to MEMS IMUs was determined. The whole system was shaken along each axis and the dynamic responses were compared in time. As shown in Fig. 6, the four MEMS

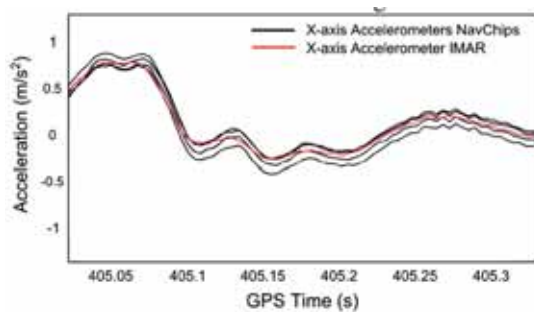


**Fig. 6:** Time-alignment of NavChip sensed specific force to the reference (iMAR-FSAS).

IMUs are synchronized well, both relative to each other and to the reference. Note that the depicted signal does not account for residual misalignments between the sensors.

### 3.3 IMU Noise Parameters

The acceleration and the angular speed measured by the MEMS IMUs are corrupted by relatively large errors of stochastic nature. These errors significantly influence the final navigation solution. Thus, they need to be filtered using a plausible model. The process of model building is not trivial at all. The following general error model can be formulated (TITERTON & WESTON 2005):

$$\hat{l} = M_l \cdot (S_l \cdot l + b_l) + w_l \quad (1)$$

where  $\hat{l}$  represents the adjusted measurements,  $l$  the observation and  $M_l$  the misalignment matrix. The diagonal matrix  $S_l$  contains the scale factors,  $b_l$  is the bias and  $w_l$  the measurement random errors.

### 3.4 Random Errors without Bias

The method of Allan variance (HOU & EL-SHEIMY 2004) is often used to determine the different types of random processes present in the inertial signal. In general, with the Allan variance only five processes are considered: quantization noise, white noise, bias instability, random walk, and the random rate ramp. The Allan variance is only used to build the model type, while the parameters of the model are estimated using the approach of generalized method of wavelet moments (GMWM) (GUERRIER et al. 2013). This estimation method is based on matching the empirical and model-based wavelet variances. The GMWM is able to handle complex error models for which other techniques such as the Allan variance or expectation-maximization (EM) algorithms fail or do not converge. The model consists of a mixture of several Gauss-Markov processes with white noise. The GMWM is used to estimate parameters of these processes, i.e. the variances and in case of Gauss-Markov processes also the correlation times.

### 3.5 Deterministic Parts

A multi-position calibration was used to estimate the deterministic errors such as the constant bias, the scale-factor and the non-orthogonality as shown in (1) (SYED et al. 2007). This method does not require any special mounting. It uses the combined effect of the local gravity and rotation vector to build the reference signals needed for calibration. The sensors do not have to be aligned to the local level frame. Nevertheless, it is necessary to have a redundant number of IMU rotations to estimate the errors by using a least-squares adjustment knowing that constraints can be imposed for accelerometers and gyroscopes:

$$f_1^2 + f_2^2 + f_3^2 - |g|^2 = 0 \quad (2)$$

$$\omega_1^2 + \omega_2^2 + \omega_3^2 - |\omega|^2 = 0 \quad (3)$$

Where  $f_{1,2,3}$  are the specific forces measured along three axes (1,2,3),  $g$  is the true local gravity,  $\omega_{1,2,3}$  are the angular rates measured along three axes, and  $\omega$  is either the earth rotation rate or a known value from a rotation table. Once the model is built its parameters enter into the in-house developed navigation software that allows GNSS/R-IMU integration in different manners (STEBLER & SKALOUD 2013). By using redundancy in inertial sen-

sors, the level of measurement noise can be estimated directly from the data itself and its level adapted dynamically by Kalman filtering/smoothing. This provides a better view of the reality while reducing the level of noise in the whole system. Furthermore, the expected overall navigation solution is improved thanks to the special mechanization/integration of inertial data. The choice of the GNSS/INS integration strategy is mainly guided by the a priori knowledge of the relative geometry between the individual IMUs, i.e. calibration vs. mission.

### 3.6 Performance Evaluation of the R-IMU

The performance of the R-IMU was evaluated during a kinematic ground test with respect to a reference IMU. The latter was a navigation grade INS (IXSEA 2013). Both units were rigidly mounted together with a GNSS antenna and attached to a car roof. The test drive lasted 20 minutes and was carried out in an area with good GNSS signal quality. The collected data were then processed by the custom software (STEBLER & SKALOUD 2013).

The bars in Fig. 7 represent the RMS values calculated from attitude differences between R-IMU and the reference. The dots and

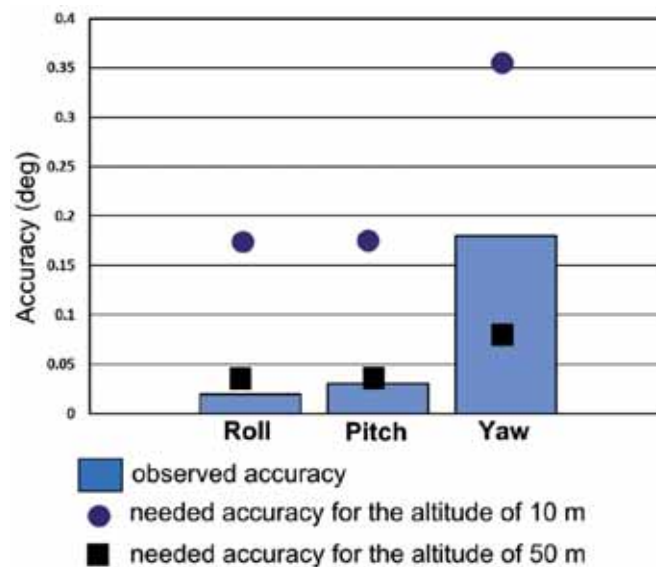


**Fig. 7:** R-IMU attitude accuracy obtained in a test on a moving car vs. required accuracy ( $1\sigma$ ) to achieve  $\sigma_{\text{ground}} = 3$  cm for flying altitudes of 10 m and 50 m.

squares depict the required attitude accuracy for a direct sensor orientation with the current lens at two flying heights so that its influence on the ground is 3 cm ( $1\sigma$ ). It can be seen that for the roll and pitch components the observed accuracy would be sufficient to contribute to direct/integrated sensor orientation. For the flying altitude of 50 m above ground the accuracy of the yaw angle obtained from the R-IMU would cause larger errors in case of direct orientation. However, its impact is mitigated in a strip/block structure due to observations of tie-points and perspective centre positions, respectively. It shall also be noted that for higher flying altitudes a lens with longer focal length would be used to preserve the ground-sampling distance.

## 4 Case Study

To evaluate the previously described development and to actually validate the existing integration of all system components, several field tests were carried out. Each test was performed for a specific task including tests on image quality, target recognition, camera calibration and synchronization of all components. However, this study is focused mainly on the quality of direct positioning. The quality of attitude control was evaluated only as presented in section 3 and is not the subject of this section.

### 4.1 Calibration Field

For the purpose of this study, we developed a calibration field (Fig. 8). Its size is approximately  $30\text{ m} \times 20\text{ m}$  with height differences of up to 2 m. 90 digitally coded targets were placed in a regular grid across the field. The positions of 25 targets were determined by tachymetric measurements and serve as ground control/check points. In such a setup we obtained high redundancy and an excellent distribution of measurements across the image plane. The estimation of the target centres in the image space was achieved by adopting the methodology commonly used by the research community of computer vision. Specifically, we have utilized the open-source software li-



Fig. 8: Calibration field.

brary ARToolkitPlus (WAGNER & SCHMALSTIEG 2007) to perform automatic target recognition. We employed the ARTag marker set due to its high marker library size, near-zero false positive identification rate as well as good accuracy potential for determining the target centres, which was reported to be 1/10 of a pixel (FIALA 2010). As the calibration field is situated in a relatively dense urban environment the quality of the satellite signal reception suffers from the limited visibility to the sky, which results in a relatively poorer geometry affecting mostly the vertical precision.

### 4.2 Data Acquisition

The performance of the proposed processing chain was evaluated during two separate flights. The first mission served specifically for the camera calibration, the second for the assessment of the synchronization and the overall quality of position control. The first flight resulted in a set of 92 images that were taken at two different height levels (5 m and 8 m) and with varying camera convergence angles. The second flight was performed several months later and had a flying pattern similar to traditional photogrammetric flights with a nadir-looking camera. This set consists of 68 images taken from the altitude of 10 m with a ground sampling distance of about 3 mm.

### 4.3 Camera Calibration

As the procedure of camera self-calibration is a well-established method, it is not repeated here; see, for example, FRASER (1997) for details. In this case all available ground control

points were processed together with the image measurements by a bundle-adjustment software (LICHTI & CHAPMAN 1997). The non-planar design of the target field, the variations of the camera convergence angles as well as the use of different flying heights above the target field decrease the correlation between the IO/EO parameters. Tab. 4 summarizes the precision of the most important results obtained from the camera self-calibration.

## 5 Results

The processing pipeline of the second flight was following that of classical airborne image processing with assisted carrier-phase differential GNSS. After the image acquisition and image processing, the image measurements were subsequently fed into a bundle adjustment (LICHTI & CHAPMAN 1997) together with the measured camera positions. The latter were obtained by interpolating between the 10 Hz GNSS solutions of carrier-phase differential results obtained by a professional software package. Self-developed Matlab scripts were used to carry out the assignment of images to the events exported from the receiver. The lever arm between the camera and GNSS antenna was measured with a calliper (Tab. 5). The R-IMU measurements were not considered in this process.

The processing was done with fixed interior orientation parameters that were estimated during the self-calibration project carried out much earlier. No ground control points were included in the adjustment. As mentioned previously, the prerequisite for such a comparison is the temporal-spatial stability between the camera and the navigation sensors. This was achieved by hard mounting the GNSS antenna and R-IMU to the camera gimbal. Even during the flight, the rigidity of the mount guarantees to maintain the stability of the relative positions (Fig. 4). The accuracy of the airborne positions was validated by comparing the GNSS-derived positions with those obtained by aerial triangulation (AT) in a separate adjustment project using 25 ground control points and re-estimated interior orientation parameters. Tab. 6 provides a summary of the quality of the GNSS data.

**Tab. 4:** Precision of the camera parameters after self-calibration.

Parameter	1 $\sigma$
Principal point (x)	0.9 $\mu$ m
Principal point (y)	2.0 $\mu$ m
Principal distance	3.5 $\mu$ m
K1 radial distortion	1.4 E-06
K2 radial distortion	7.9 E-09

**Tab. 5:** Measured lever arm.

Lever arm	Length (cm)
E <sub>x</sub>	5.5
E <sub>y</sub>	-1.1
E <sub>z</sub>	12.9

**Tab. 6:** Summary of the quality of the GNSS data.

	Horizontal (m)	Vertical (m)
Mean estimated accuracy of GNSS positions	0.016	0.023
RMS of EO positions: estimated (AT + 25 GCPs) vs. GNSS measured	0.020	0.039
Maximal GNSS residual	0.069	0.099

**Tab. 7:** Residuals at 25 check points with GNSS-determined camera positions without using ground control points.

Residual	X (m)	Y (m)	Z (m)
MAX	0.028	0.043	0.079
MEAN	0.012	0.009	0.019
RMS	0.022	0.010	0.044

The characteristics of the residuals are presented in Fig. 9 where deviations in positions are depicted as points representing the differences between GNSS-derived positions of the camera perspective centres and those estimated by bundle adjustment with 25 ground control points.

As the lever-arm offset was subtracted from these differences, the depicted variations represent the Euclidean distance from the GNSS observations to the estimated camera perspective centres. We can see that their magnitude is not correlated with the flying speed. The observations lie within the interval given by the predicted incertitude of the estimated EO parameters (about 2 cm in horizontal, 3 cm – 4 cm in vertical direction). This confirms the sufficiently precise synchronization between the camera and GNSS receiver.

The statistics related to the residuals on all 25 check points are shown in Tab. 7. The overall RMS in position differences at the check points is 5 cm. The ground precision matches expectations and corresponds to the accuracy of kinematic carrier-phase differential GNSS. Despite that, an improvement can be still carried out as a part of the position error can be assigned to the GNSS signal quality, e.g. low SNR and higher than normal incertitude in height measurement.

The time-interval between the calibration and presented test flight was more than six months with several flights in between. This confirmed a sufficient stability of the IO parameters of the used camera-lens system.

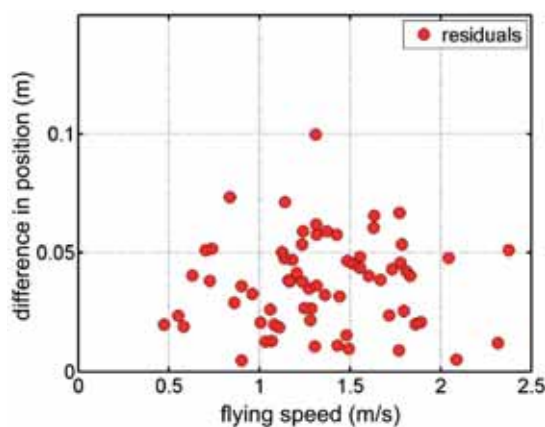


**Fig. 9:** Comparison of the GNSS-determined camera positions with the results of the AT.

## 6 Conclusion and Perspectives

This research aimed at proposing and investigating a novel approach in data acquisition with MAV. The outcomes from the bundle adjustment confirmed the correctness of the preceding development in terms of camera/GNSS integration. The most challenging part of the sensor integration and synchronization on the relative small and low cost UAV system was accomplished. The employed realization isolates the measuring devices from vibrations and provides stable spatial offsets between them. A small case study was performed to verify the quality of synchronization and the accuracy of camera position control. The latter is at 2 cm – 5 cm level which corresponds to the kinematic accuracy of a carrier-phase differential GNSS. The method of integrated sensor orientation allows performing mapping with cm-level accuracy without the need of ground control points. Future investigation will study the attainable attitude accuracy of the redundant MEMS IMU on-board the MAV. The performance of this sub-system is promising, as indicated by a car-based experiment reported in this paper.

## References

- AIBOTIX, 2013: <http://www.aibotix.com/> (10.12.2013).
- BÄUMKER, M. & PRZYBILLA, H.-J., 2011: Investigation on the accuracy of the navigation data of unmanned aerial vehicles using example of the system Mikrokoopter. – Conference on Unmanned Aerial Vehicles in Geomatics, Zurich, Switzerland.
- BÄUMKER, M., PRZYBILLA, H.-J. & ZURHORST, A., 2013: Enhancements in UAV flight control and sensor orientation. – Conference on Unmanned Aerial Vehicles in Geomatics, Rostock, Germany.
- BLÁHA, M., EISENBEISS, H., GRIMM, D. & LIMPACH, P., 2011: Direct georeferencing with UAVs. – Conference on Unmanned Aerial Vehicles in Geomatics, Zurich, Switzerland.
- COLOMINA, I., 1999: GPS, INS and Aerial Triangulation: what is the best way for the operational determination of photogrammetric image orientation? – ISPRS Conference Automatic Extraction of GIS Objects Digital Imagery, München.

- COLOMINA, I. & MOLINA, P., 2014: Unmanned aerial systems for photogrammetry and remote sensing: A review. – *ISPRS Journal of Photogrammetry and Remote Sensing* **92** (6): 79–97.
- ELING, C., KLINGBELL, L., WIELAND, M. & KUHLMANN, H., 2014: Direct Georeferencing of Micro Aerial Vehicles – System Design, System Calibration and First Evaluation Tests. – *PFG – Photogrammetrie, Fernerkundung, Geoinformation* **2014** (4): 227–237.
- EUGSTER, H. & NEBIKER, S., 2008: UAV-based augmented monitoring – real-time georeferencing and integration of video imagery with virtual globes. – *ISPRS XXIIth Congress* **37** (B/1): 1229–1236, Beijing, China.
- FIALA, M., 2010: Designing highly reliable fiducial markers. – *IEEE Transactions on pattern analysis and machine intelligence* **32** (7): 1317–1324.
- FRASER, C.S., 1997: Digital camera self-calibration. – *ISPRS Journal of Photogrammetry and Remote Sensing* **4** (52): 149–159.
- GUERRIER, S., WAEGLI, A., SKALLOUD, J. & VICTORIA-FESER, M.-P., 2011: Fault Detection and Isolation in Multiple MEMS-IMUs Configurations. – *IEEE Transaction on aerospace and electronic systems* **48**: 2015–2031.
- GUERRIER, S., SKALLOUD, J., STEBLER, Y. & VICTORIA-FESER, M.-P., 2013: Wavelet-variance-based estimation for composite stochastic processes. – *Journal of the American Statistical Association* **108**: 1021–1030.
- HOU, H. & EL-SHEIMY, N., 2004: Modeling Inertial Sensors Errors Using Allan Variance. – Master thesis, University of Calgary, AL, Canada.
- INTERSENSE, 2013: <http://www.intersense.com/pages/16/16> (12.12.2013).
- IXSEA, 2013: IXSEA AirINS. – [http://www.ixsea.com/en/mobile\\_mapping\\_airborne\\_survey/3/airins.html](http://www.ixsea.com/en/mobile_mapping_airborne_survey/3/airins.html) (10.12.2013).
- JAVAD, 2013: Javad TR-G3T datasheet. – [www/javad.com/downloads/javadgnss/sheets/TR-G3T\\_Rev.5\\_Datasheet.pdf](http://www.javad.com/downloads/javadgnss/sheets/TR-G3T_Rev.5_Datasheet.pdf) (5.12.2013).
- JON, J., KOSTKA, B. & POSPISIL, J., 2013: Autonomous airship equipped with multi-sensor mapping platform. – 3D-ARCH 2013 – 3D Virtual Reconstruction and Visualization of Complex Architectures: 119–124, Trento, Italy.
- KLUTER, T., 2012: Gecko4Nav. – Technical reference manual, revision 1.0.
- LICHTI, D. & CHAPMAN, M.A., 1997: Constrained FEM self-calibration. – *Photogrammetric Engineering & Remote Sensing* **63** (9): 1111–1119.
- MOSTAFA, M., HUTTON, J. & REID, B., 2001: GPS/IMU products – the Applanix approach. – *Photogrammetric Week*: 63–83, Wichmann, Heidelberg.
- MULTIROTOR FORUM, 2013: <http://www.multirotorforums.com/showthread.php?4015-X8-vs-flat-octo-redundancy-comparison> (13.4.2014).
- NASSAR, S. & EL-SHEIMY, N., 2005: Sensor Integration and Image Georeferencing for Airborne 3D Mapping Applications. – *ISPRS International WG 1/2 Workshop 2005: 3D Mapping from InSAR and LiDAR*, Banff, AL, Canada.
- PFEIFER, N., GLIRA, P. & BRIESE, C. 2012: Direct georeferencing with on board navigation components of light weight UAV platforms. – *ISPRS XXIIth Congress* **39** (B/7), Melbourne, Australia.
- REMONDINO, F., BARAZZETTI, L., NEX, F., SCAIONI, M. & SARAZZI, D., 2011: UAV photogrammetry for mapping and 3D modeling – current status and future perspectives. – *Conference on Unmanned Aerial Vehicles in Geomatics*, Zurich, Switzerland.
- SCHWARZ, K.P., CHAPMAN, M., CANNON, M. & GONG, P., 1993: An integrated INS/GPS approach to the georeferencing of remotely sensed data. – *Photogrammetric Engineering & Remote Sensing* **59** (11): 1667–1674.
- SENSEFLY, 2013: Ebee. – <https://www.sensefly.com/drones/overview.html> (10.12.2013).
- SKALLOUD, J., COSANDIER, D., SCHWARZ, K.P. & CHAPMAN, M., 1994: GPS/INS orientation accuracy derived from a medium scale photogrammetry test. – *International symposium on kinematic systems in geodesy, Geodesy and navigation*, KIS94, Banff, AL, Canada.
- SKALLOUD, J., CRAMER, M. & SCHWARZ, K.P., 1996: Exterior orientation by direct measurements of camera position and attitude. – *International archives of photogrammetry and remote sensing* **31** (B3): 125–130, Vienna, Austria.
- SKALLOUD, J., 1999: Problems in Direct-Georeferencing by INS/DGPS in the airborne environment. – *ISPRS Workshop on Direct versus indirect methods of sensor orientation*, WG III/1, <http://infoscience.epfl.ch/record/29150> (1.5.2014).
- SKALLOUD, J., SCHAER, P., STEBLER, Y. & TOME, P., 2010: Real-time registration of airborne laser data with sub-decimeter accuracy. – *ISPRS Journal of Photogrammetry and Remote Sensing* **65** (2): 208–217.
- STEBLER, Y. & SKALLOUD, J., 2013: Modeling and processing approaches for integrated inertial navigation. – PhD thesis, EPFL, Lausanne, Switzerland.
- SWISSDRONE, 2013: Dragon 35, [http://www.swissdrones.com/SwissDrones\\_AG/Products.html](http://www.swissdrones.com/SwissDrones_AG/Products.html) (5.4.2013).

- SYED, Z., AGGARWAL, P., GOODALL, C., NIU, X. & EL-SHEIMY, N., 2007: A new multi-position calibration method for MEMS inertial navigation systems. – *Measurement science and technology* **18**: 1897–1907.
- TITTERTON, D. & WESTON, J., 2005: *Strapdown inertial navigation technology*. – 2<sup>nd</sup> edition, ISBN 0863413587.
- TRIMBLE, 2013: UX5. – <http://uas.trimble.com/> (5.12.2013).
- WAGNER, D. & SCHMALSTIEG, D., 2007: ARToolkit-Plus for pose tracking on mobile devices. – 12th Computer Vision Winter Workshop, Graz, Austria.
- WÄGLI, A., SKALLOUD, J., GUERRIER, S., PARÉS, M.E. & COLOMINA, I., 2010: Noise reduction and estimation in multiple micro-electro-mechanical inertial system. – *Measurement science and technology* **21**.
- 3DROBOTICS, 2013: Ardupilot Mega 2.5, <http://www.store.3drobotics.com> (10.4.2013).

## Address of the Authors:

Ing. MARTIN REHAK, Ing. ROMAIN MABILLARD & Dr. JAN SKALLOUD, École Polytechnique Fédérale de Lausanne (EPFL), Geodetic Engineering Laboratory (TOPO), CH-1015 Lausanne, Tel.: +41-21-693-2756, -2755, -2753, Fax: +41-21-693-5740, e-mail: {martin.rehak}{romain.mabillard}{jan.skaloud}@epfl.ch

Manuskript eingereicht: Oktober 2013  
Angenommen: März 2014





## MACS-TumbleCam – A Novel Approach for Aerial Oblique Imaging

JÖRG BRAUCHLE, WOLFGANG RÜTHER-KINDEL & RALF BERGER, Berlin

**Keywords:** oblique camera, aerial imaging, UAV, digital terrain modelling, modular payload concept, MACS-TumbleCam, 3D-model

**Summary:** The ATISS measurement drone, developed at the University of Applied Sciences Wildau, is an electrical powered autonomous motor glider with a maximum take-off weight of 25 kg including a payload capacity of up to 10 kg. Two engines enable ultra short take-off procedures and the motor glider design results in a 1 h endurance. The concept of ATISS is based on the idea to strictly separate between aircraft and payload functions, which makes it a very flexible research platform for miscellaneous applications.

In a project together with German Aerospace Center (DLR) this carrier was used for demonstrating a novel approach in high-resolution digital terrain modelling.

A lightweight, 3D-capable photogrammetric camera called MACS-TumbleCam was developed at the DLR Berlin especially for the ATISS payload concept. The unique feature of this camera system is the special combination of two synchronized digital cameras with an adjustable relative alignment. One camera head is oriented in a fixed nadir position while the other one can be driven to variable oblique orientations by a robotic actuator. Thus it is possible to take images from very different view directions for almost every object on the ground. Due to a parametric boresight calibration a low-cost inertial orientation system can be used.

The evaluation of the first test flights shows features of the system, i.e. derived high-precision 3D-models of urban structures with 3 cm ground pixel resolution and high-resolution façade textures.

**Zusammenfassung:** *MACS-TumbleCam – ein neues Verfahren für Schrägluftbilder.* ATISS, eine an der Technischen Hochschule Wildau (FH) entwickelte Messdrohne, ist ein elektrisch angetriebener autonomer Motorgleiter mit einem maximalen Abfluggewicht von 25 kg bei einer Nutzlastkapazität von bis zu 10 kg. Zwei Motoren ermöglichen sehr kurze Startvorgänge und eine Flugzeit von etwa einer Stunde. Das Systemdesign von ATISS basiert auf einer strikten Trennung von Nutzlast- und Flugzeug-Funktionen, was den Träger zu einer flexiblen Forschungsplattform für unterschiedliche Anwendungen macht.

In einem gemeinsamen Projekt mit dem Deutschen Zentrum für Luft- und Raumfahrt (DLR) konnte mit diesem Träger ein neuartiges Konzept zur hochauflösenden luftgestützten Geländemodellierung demonstriert werden.

Dazu wurde vom DLR ein sehr kompaktes 3D-fähiges Luftbildkamera-System (MACS-TumbleCam) entwickelt. Dieses Konzept kombiniert zwei synchronisierte Kameras mit einer Aktuatorik zur schnellen Veränderung der Relativlage. Dabei schaut ein Kamerakopf senkrecht (nadir), der zweite ist dem gegenüber mit einem variablen Sichtwinkel (oblique) ausgerichtet. Dies ermöglicht die weitgehend vollständige hochgenaue Abbildung von Objekten aus unterschiedlichen Perspektiven. Eine parametrische Bore-sight-Kalibrierung ermöglicht die Nutzung eines low-cost Orientierungssystems. Die Auswertung erster Testflüge zeigt die Fähigkeiten des Gesamtsystems. So konnten aus den Daten des Kamerasystems hochgenaue 3D-Modelle urbaner Strukturen mit 3 cm Bodenpixelauflösung inklusive hochauflösender Fassadentexturen gewonnen werden.

## 1 Introduction

Aerial imaging from small unmanned aircrafts (UAVs) has become an emergent topic in recent years (EISENBEISS 2009). The rise was mainly caused by the availability of low-priced but mature aerial vehicles. Applications range from surveillance and reconnaissance to environmental or agricultural monitoring as well as mapping and photogrammetry (ZHANG & KOVACS 2012, HEINZE et al. 2010, REMONDINO 2011).

Apart from military systems, mostly small multicopter or fixed wing aircraft are used, with a maximum take-off weight less than 5 kg. Since there are no photogrammetric camera systems available that can be carried by such limited aircraft, the usual approach is to operate commercial consumer cameras together with a low-cost GPS receiver (CRAMER et al. 2013, NEITZEL & KLONOWSKI 2011, KÜNG et al. 2011a).

Evaluation of such data is often done based on structure-from-motion approaches. While this gives fast and visually appealing results, positional accuracy of the data is difficult to determine.

The first UAV (unmanned aerial vehicle) project at the University of Applied Sciences Wildau started in 2006. It was called SMAP (smart aerial photogrammetry system) and was based on a market-available fixed wing model aircraft. The aim was to demonstrate that small UAV are capable of carrying a calibrated aerial camera to produce aerial images of a quality comparable to man operated systems. A Trimble AIC camera system was integrated in the fuselage together with a navigation system, an on-board computer and a telemetry system.

This project was successfully completed. However, it showed that neither the carrier aircraft nor the camera system was ideal for this kind of mission. The main disadvantages were vibrations from the piston engine, the limited access to the camera system in the narrow fuselage and the total weight of the system. As a consequence it was decided to develop a new carrier aircraft especially designed for multi role measurement tasks.

## 2 The ATISS UAV

Based on the experiences of this first project the system design of UAV ATISS (Autonomous Flying Testbed for Integrated Sensor Systems) was started in 2007. The key requirements for this new aircraft were

1. separation of payload and carrier functions,
  2. electrical propulsion system,
  3. easy access payload concept,
  4. motor glider design for low energy consumption,
  5. low approach speed of 10 m/s,
  6. maximum take-off weight of 25 kg, and
  7. payload up to 10 kg.
8. Configuration and construction were carried out as a bachelor thesis (DANDERS 2007), see Fig. 1.

The final production took place in the aeronautics research lab of the working group, with the first flight performed in summer 2009, see Fig. 2.

The maximum take-off weight of 25 kg was chosen due to legal restrictions in Germany (SEILER 2013), but it can be extended if required. The actual payload capacity of 10 kg gives enough flexibility for a large choice of equipment. Speed range is from 10 m/s to 40 m/s, typical operation speed is 18 m/s for

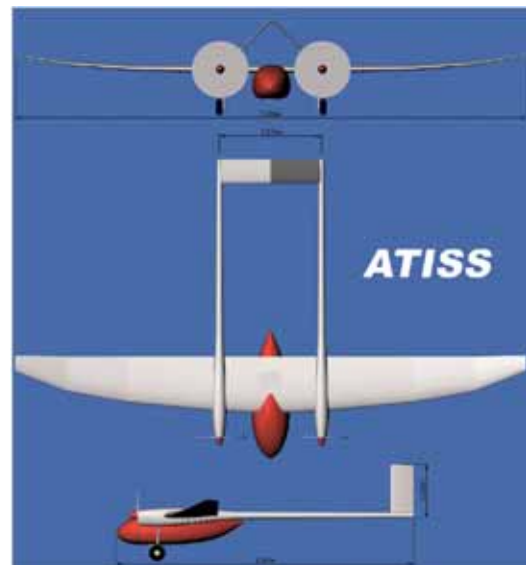


**Fig. 1:** ATISS (autonomous flying testbed for integrated sensor systems) design.



**Fig. 2:** ATISS UAV first flight.



**Fig. 3:** Payload concept CONTAIN.

an endurance of approximately 1 h, which can be increased by reducing the payload weight.

The modular and easy access payload concept CONTAIN (concept for autonomous operating aerial sensor payloads) is shown in Fig. 3. The rack system offers a payload compartment of  $220 \times 220 \times 400 \text{ mm}^3$  volume. The rail system enables easy and fast access to the payload.

The first project for the newly developed aircraft was called SALSA (smart airborne laser scanner) and aimed to integrate a laser scanner for digital terrain modelling. It was clear that it would be difficult to combine a laser scanner with an aerial camera within the ATISS payload limit of 10 kg. After technical discussions with the German Aerospace Center, the technical concept was completely revised in favour of an innovative multi-head camera system instead of a laser scanner, combined with a high-end direct georeferencing device. This new payload idea has considerable advantages regarding costs, weight, ground resolution and accuracy.

### 3 Aerial Camera MACS-TumbleCam

Remote sensing on unmanned platforms offers enormous demands for photogrammetric cameras. However, ad hoc developed systems are practically lacking. The requirements for sophisticated sensor systems are challenging, particularly with respect to dimensions and weight. The pursuit of higher ground sampling distances in the centimetre range requires the carrier to be closer to the target, utilizing smaller electrically powered carriers. One or more circular or linear flight paths over a distinctive object are often shown, followed by computer-based modelling of this object (KÜNG et al. 2011b, LI & LI 2011, WENZEL et al. 2013). Flight times of 15 min to 30 min are common until the need for touch-down.

The Institute of Optical Sensor Systems at the DLR developed the “Modular Airborne Camera Systems (MACS)”, which are a family of highly specialized aerial cameras with many practical applications (LEHMANN et al. 2011). When deploying this concept, advanced requirements of the mission can be fulfilled.

With MACS-TumbleCam a new method of acquiring oblique images is realized. Thus, the target area of airborne surveys can be increased considerably. Practical demonstration was carried out during several test flights with the ATISS UAV in 2012. High precision geoinformation can be derived using images of this lightweight measurement camera system, e.g. fully texturized 3D-models.

#### 3.1 Requirements

As described in chapter 2, the concept of ATISS is based on a strict separation of carrier and payload functions. Thus, a self-sustaining 3D-capable aerial camera system was developed. ATISS provides payload dimensions of  $220 \times 220 \times 400 \text{ mm}^3$  ( $W \times H \times L$ ) and a weight of up to 10 kg. All peripherals such as power supply, GNSS system with support by an inertial measurement unit (IMU) and computational devices had to be integrated into the pod. Actual weight and dimensions of the camera system are listed in Tab. 1. The main objective was to acquire high-grade images

**Tab. 1:** Setup MACS-TumbleCam.

Imaging sensors	RGB CCD, 3296 x 2472 pixels, 5.5 $\mu\text{m}$ pixel pitch
Camera quantity	2, one nadir and one oblique
Ground sampling distance	$\sim 2$ cm @ 100 m height (above ground)
Radiometric resolution	12 bit raw image
Focal length	35 mm each camera
Image rate	5 Hz maximum
Arrangement	1x nadir + 1x oblique with tilt angle of $\sim 30$ deg and arbitrary rotation
Actuator tumbling camera	Rotational stage, 34 $\mu\text{rad}$ encoder resolution
Direct georeferencing	Post-processed L1/L2 GNSS + MEMS AHRS
Computer	3.5" single board, Atom D525, Linux, 2x 256 GB SSD
On-board recording	$\sim 40,000$ images
Telemetry	868 MHz
Dimensions	400 x 220 x 200 $\text{mm}^3$ (L x W x H)
Weight	$< 4$ kg ( $< 5$ kg with LiPo battery)
Power supply	LiPo battery for 1 h operation, or 9 – 36 VDC

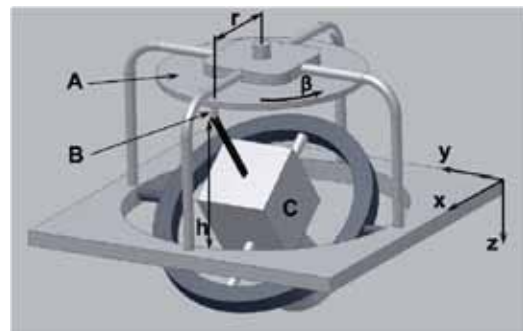
to facilitate accurate models of the surveyed area, therefore photogrammetric cameras are used. Good exterior orientation parameters for all images had to be delivered to assist the aerial triangulation (AT) in post-processing. For visualization of realistic façades, views of the target from different directions had to be acquired. Due to the fixed wing flight characteristics of ATISS parallel lines are flown.

### 3.2 The Tumbling-Concept

These requirements imply that conventional methods of taking oblique images could not be adopted. Taking a penta-camera head (5 fixed cameras with 1 nadir and 4 main oblique axes) would lead to too much weight, energy consumption and computer capacities. On the other hand a triple-camera head (3 fixed cameras with 1 nadir and 2 left-right oblique axes) would reduce the ground coverage by approximately 50% at a given flight endurance, because there is the need for additional flight lines to acquire all 4 main oblique perspectives.

A new approach to acquire multiple perspectives using only one camera is given by the tumbling sensor, see Fig. 4: The camera

(C) is biaxially gimbal-mounted. It can be arbitrarily deflected from the not gimballed axis (z). This converts the camera into an oblique camera. Fixed by a catch (B), the oblique angle is defined by distances between catch and gimbal origin, ( $r$ ) and ( $h$ ). Here a configuration with fixed radius ( $r$ ) is introduced. If radius ( $r$ ) was variable, the oblique angle would be variable accordingly. The catch is mounted on a rotary element (A) and describes a circular path which is the only remaining degree of freedom. By rotating (A) the camera is forced to oscillate around both gimbal axes. Hence the camera's main axis (optical axis) describes a cone whose axis is (z).

**Fig. 4:** Operation principle of tumbling camera.

In this way, only one control parameter (actual position of rotary element, angle  $\beta$ ) will allow the camera to reach all four major perspectives ahead, right, back and left. In addition, arbitrary perspectives are obtainable which are circular around axis  $z$ . In remote sensing applications, the  $z$  axis points towards the nadir point. Hence the camera footprint circulates around the nadir point.

The relation between angular velocity  $d\beta/dt$  and camera acquisition rate determines the overlap of two consecutive images. The direction of rotation is reversible. Velocity is adjustable from 0 deg/s up to 360 deg/s. As the rotation range is unlimited, an  $n \times 360$  deg motion is possible. The camera moves in a tumbling way, hence rotation around the optical axis is avoided, and the cabling remains torsion-free. Rotary joints are not required. Unlimited circulation plays an important role for the photogrammetric processing of images: as a result of the linear flight path the rotating oblique image footprints become a spiral, resulting in a special image block configuration. Fig. 5 shows a constellation of oblique footprints based on real data, here with an oblique angle of  $\sim 30$  deg, gear steps of 45 deg and aircraft crab angle of about  $-10$  deg. The crab-angle can be easily compensated on-the-fly by

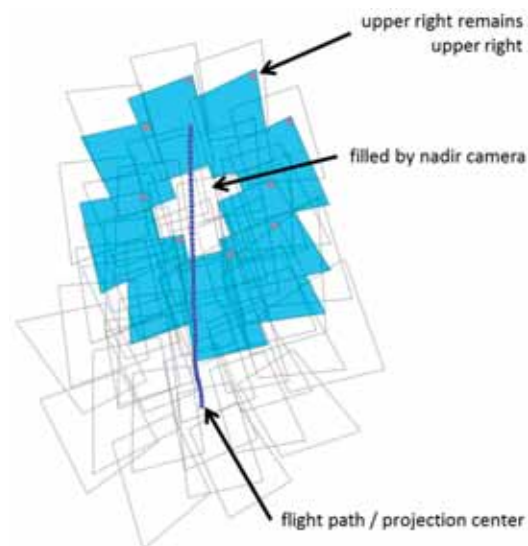


**Fig. 5:** Footprints characteristics of a tumbling camera. Blue dots assign the flight path. Red dots mark upper right image corners, indicating that there is no rotation about the optical axis.

adjusting the motor's zero point position. One full circle of camera rotation is shown in blue colour. The unfilled frames show the spiral of footprints caused by flight path.

In case of an ideal flight trajectory, again by avoiding rotation about the optical axis, the yaw angle of oblique images remains unchanged. Independent of the camera orientation, each image corner remains in the same relative position, see the red marks in Fig. 5. Photogrammetric analysis can be carried out analogously to common nadir image flights using conventional algorithms. The nadir area is covered by an additional fixed camera (Fig. 6).

### 3.3 MACS-TumbleCam

Combining nadir camera and oblique tumbling camera as shown in Fig. 6, added by peripheral devices, enables a lightweight aerial camera system for 3D data acquisition, see Fig. 7.

The oblique footprints circulate around the nadir camera's footprint. Every image has to cover a particular ground detail, not a quadrant as in penta- or triple-systems. The focal

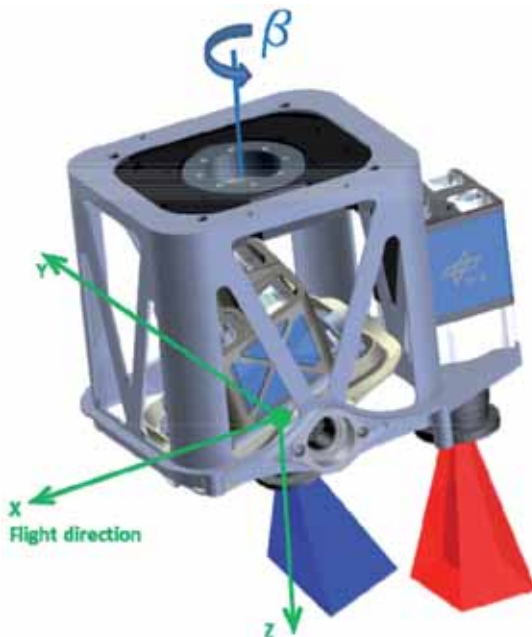


**Fig. 6:** Sensor head with tumbling camera (left) and a nadir camera (right); green: coordinate system of sensor head.



Fig. 7: MACS-TumbleCam.

length can be increased, resulting in higher resolution oblique images. The mounted sensors consist of two 8 megapixel industrial cameras including trigger and event interfaces. Both cameras are constructed identically and take images synchronously. A pair of images with different orientations is generated simultaneously.

With proper overlap of the oblique images the block can be oriented by AT without the use of nadir images. No AT can be processed if only a small overlap between oblique images is available, e.g. an overlap of less than about 5%, which may be caused by a fast camera rotation while using a low image acquisition rate. In this case, the following process can be used for determining the exterior orientation. One can first determine the exterior orientations of nadir images by conventional AT and then transform the exterior orientation of any nadir image to the corresponding oblique image (WIEDEN & STEBNER 2013). As the geometric relation between both images is known, there is no need to overlap nadir and corresponding oblique image, see section 3.4.

The transformation of exterior orientation between images of any image pair is described in section 3.4. To apply this process, the correct geometric relation between both cameras needs to be known for the time of exposure. This geometric relation mainly arises from the construction of the sensor head and from the actual position of the rotary element in terms of angle  $\beta$ . Hence, a rigid frame for both cameras was constructed and a drive unit was assembled, see Fig. 6. The nadir camera and the drive unit are mounted stationary. By

mirrored spring constraints, the gimbaling of the tumbling camera is restrained from free floating that might be caused by any occurring dynamic forces. Further, any temperature-dependent shift is compensated. The weight of the rigid aluminium frame is 214 g.

The constant oblique deflection was set to an angle such that a small overlap between any oblique / nadir image pair is ensured. Thus, an associated image block is established for the images of the first camera and of the second camera, respectively. Furthermore, the images of both cameras are connected by corresponding image points. By operating these two cameras as described, an overall nadir angle combination analogous to a penta-camera head is achieved. The difference is that the tumbling camera acquires the oblique images successively and not at the same moment, as penta-camera heads do.

To move the sensor, a rotation stage of 14 mm height was integrated. It has a built-in angle encoder achieving a resolution of 34  $\mu$ rad (0.002 deg). For the duration of the image acquisition the motor stops and delivers its actual angular position (angle  $\beta$ ) to the computer. Afterwards, the motor rotates the camera to the position for the next image.

Mainly due to weight restrictions the direct georeferencing is produced by a MEMS-based GNSS-aided attitude and heading reference system (AHRS) consisting of a 6 degree of freedom IMU, 3D magnetometer and L1 C/A code GNSS receiver. The AHRS-data are UTC-time stamped with a rate of 120 Hz. Bias stability of the IMU is 1 deg/s for the gyros and 0.02 m/s<sup>2</sup> for the accelerometers, respectively. The noise is 0.05 deg/s/sqrt(Hz) for the gyros and 0.002 m/s<sup>2</sup>/sqrt(Hz) for the accelerometers, respectively. The built-in magnetometers as well as a GNSS solution assist the AHRS to compensate the IMU drifts and enable the output of earth-referenced Euler-angles roll, pitch and heading.

For the AT and 3D modelling, the geodetic position of the projection centres is of much higher importance. Hence, an L1/L2 GNSS receiver for post-processing raw measurements including reference stations was used. The accuracy thus obtained is evaluated in section 4. The general set-up of MACS-TumbleCam is shown in Tab. 1. As a main attribute it should

be noted that the fully operational system has a weight of less than 4 kg plus 1 kg for the payload battery. ATISS is made for a payload of up to 10 kg.

### 3.4. Geometric Accuracy

The geometric relation between nadir camera and oblique camera requires lever arms and angular offsets dependent on the rotational element position. The lever arms are determined directly from the CAD-model. Angular offsets are calculated using the equations

$$\varphi(\beta) = \sin(\beta) * \gamma \tag{1}$$

$$\theta(\beta) = \cos(\beta) * \gamma \tag{2}$$

$$\psi = 0 \tag{3}$$

where

$\varphi$  (roll),  $\theta$  (pitch) and  $\psi$  (yaw) = rotation angles around the sensor head coordinate frame axes x, y and z, respectively (see Fig. 6),

$\beta$  = angular motor position and  
 $\gamma$  = deflection angle of the oblique camera (30 deg, fixed).

These values are used to compute the rotation matrix which transforms the oblique camera orientation into the sensor head coordinate frame (x,y,z-coordinate frame in Fig. 6). A second rotation matrix is used to transform the sensor head coordinate frame into the terrestrial frame with the help of Euler angles, which are provided by the AHRS. Angular correction values (boresight corrections) which depend on the actuator-position have additionally been applied to the angular offsets between the camera and the sensor head frames. This is necessary as a result of manufacturing and assembly imprecision, tolerances within the kinematic chain and angular encoder uncertainty. The boresight corrections have been determined photogrammetrically using the mathematical principle of projective reconstruction. In a laboratory set-up a calibrated camera Canon EOS 5D was fixed to the sensor head frame. Its images played the role

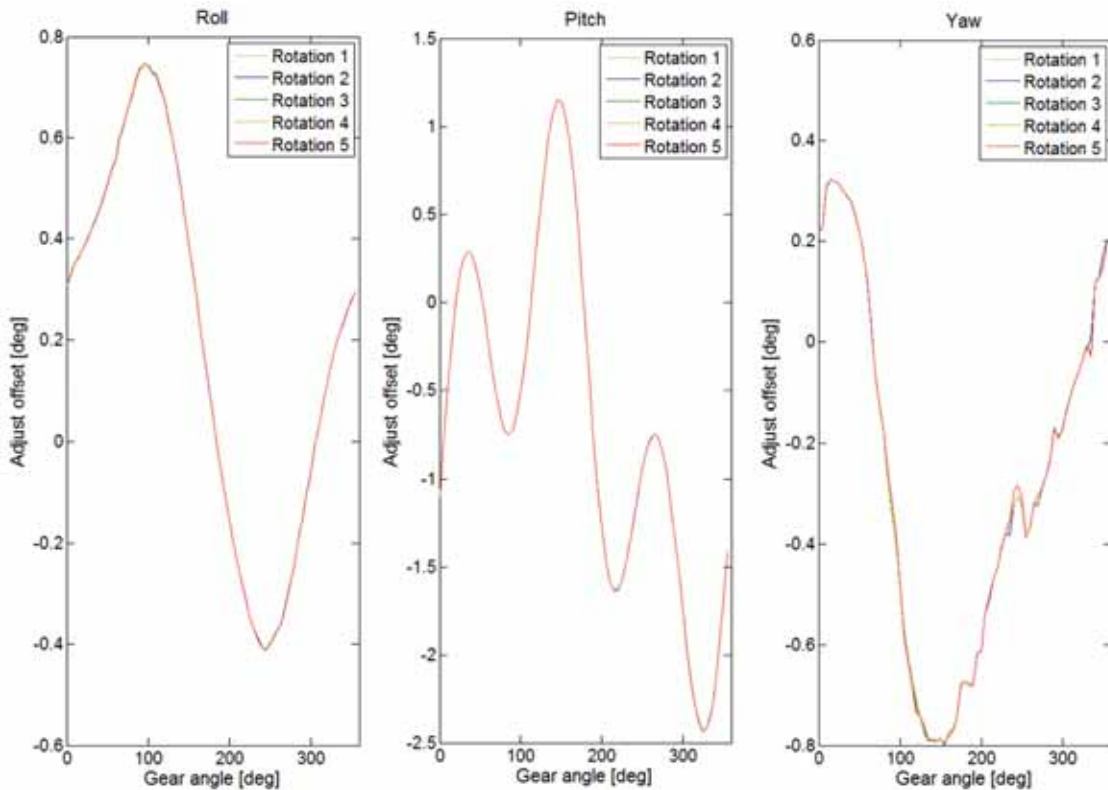


Fig. 8: Angular boresight corrections for Roll, Pitch and Yaw, repeated for 5 full circles.

of joining the minimally overlapping images of nadir and oblique cameras. The EOS 5D images remained static and covered the footprint of all possible oblique footprints. Consequently the nadir camera's footprint was covered as well. The motor turned in steps of 5 deg. At every rest position the images of all three cameras were taken simultaneously. For analyzing the repeat accuracy five full circles of the oblique rotating camera were carried out, leading to 361 image triplets. Executing block matching (MATHWORKS 2013) on each of the static camera images showed that this camera did not change orientation. Thus, just one EOS 5D image could be used as a reference. The purpose of this image was the concatenation of all oblique images. Any oblique image, the nadir image and the concatenation image are projected onto the same plane. Aided by 5323 features, for each of the oblique images the relative angular offset to the reference image was determined. Fig. 8 shows the difference between angles derived by (1) to (3) and real angles determined by the photogrammetric procedure. For each axis and every actuator position, these values are the boresight corrections.

Repeat accuracies for all the five passages are shown in Tab. 2. For the 5 boresight correction curves of roll, pitch and yaw (Fig. 8) mean value curves are calculated, respectively. The determined standard deviations are related to the mean value curves.

The standard deviations indicate that the angular error between any projected oblique image and the projected nadir image is less than 1 pixel ( $2\sigma$ ). Hence the sensor head consisting of drive unit, gimballed mount and two cameras complies with the requirements of a photogrammetric camera system.



**Fig. 9:** Image mosaic generated by applying the angles  $\phi$ ,  $\theta$  and  $\psi$  and additional boresight corrections for the oblique images.

As the correction values are very small, they are applied as additive corrections to the angular offsets, and the corrected values are used to compute the rotation matrix  $R$  which transforms the camera orientations. So the exterior orientation of the nadir camera can be converted into the exterior orientation of the oblique camera and vice versa.

To show that there is 1 pixel accuracy, the boresight corrections for one full circle of oblique images have been considered to form a stitched picture, see Fig. 9. The single images are taken from the laboratory set-up. Images of 5 deg angular position offsets are stitched without any image analysis or interpretation. A deeper analysis of the accuracies that can be achieved by the MACS-TumbleCam is given in (WIEDEN & STEBNER 2014).

**Tab. 2:** Repeat accuracies, 5 times any of 72 angular actuator positions.

	Mean standard deviation ( $2\sigma$ )	Max standard deviation ( $2\sigma$ )
$\Phi$ (roll)	8.6/1000 deg	10/1000 deg At photo 219
$\Theta$ (pitch)	7.8/1000 deg	17/1000 deg At photo 003
$\Psi$ (yaw)	35.9/1000 deg	96/1000 deg At photo 003

## 4 Test Flight

In April 2012 some test flights were conducted using ATISS as carrier. Steered by the autopilot system, 10 parallel flight lines were passed, see Fig. 10. The target area was  $1 \times 0.3 \text{ km}^2$ . The operating height was approximately 200 m above ground level, resulting a ground sampling distance (GSD) of approximately 3 cm at nadir.

For one flight, conventional AT was processed on 726 nadir images by using 6 ground control points (GCP). Further for the projection centres of the nadir images RTK GNSS positions and additional AHRS attitude data were introduced. The internal accuracy of the AT was determined to be 0.1 pixels. Tab. 3 shows the mean standard deviations of the projection centres.

With the help of semi-global matching (SGM) the nadir images were used to generate a digital elevation model (DEM). Afterwards, an orthomosaic was processed. Fig. 11 shows a single oblique image, one of multiple images used to texturize façades following the procedure described in section 3.4. Based on the texturized 3D-model, interactive visualizations can be established. Fig. 12 shows a screenshot of such a visualisation. Each pixel has a well-defined spatial coordinate. The virtual model is based on data exclusively derived by MACS-TumbleCam. Further processing such as the determination of roof geometries, tree counting, classifications etc. can be applied.

## 5 Conclusions and Future Work

A self-sustaining 3D-capable photogrammetric aerial camera system was presented which requires less than 5 kg capacity. A nadir camera was applied to determine exterior orientations and to derive outputs such as digital elevation models and orthomosaics. The single oblique camera is enabled by robotic actuation to cover perspectives around nadir. The oblique camera's rotation about the optical axis is avoided by the described tumbling movement concept. While the camera rotation is not limited, the cabling is kept free from torsion and consequently rotary joints

**Tab. 3:** SD of nadir images exterior orientation.

Mean SD translations (m)		Mean SD rotations (deg)	
X	0.012	<b>Omega</b>	3.7/1000
Y	0.013	<b>Phi</b>	3.8/1000
Z	0.021	<b>Kappa</b>	1.2/1000

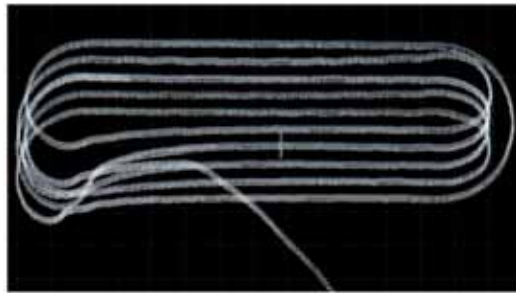


**Fig. 10:** ATISS test-flight path.



**Fig. 11:** Single raw oblique image.



**Fig. 12:** Screenshot of interactive 3D-visualization.

can be omitted. Further image processing is faster as there is one degree of freedom less. The system was used on the UAV ATISS for automated, high resolution and pixel-accurate façade texture without aerotriangulation of its oblique images.

In further steps on-the-fly crab angle compensation is examined, the motor assembly is intended to be significantly reduced in weight, and the actuator is to be used to establish forward motion compensation. A second unconstrained degree of freedom, introducing variable radius ( $r$ ) can be implemented to make the oblique angle adjustable. Hence, all perspectives around nadir could be reached. Even nadir orientation could be set. If the movement of the camera works fast enough, the fixed nadir camera then can be rejected.

The ATISS measurement UAV is still part of the SALSAs project. Further development on ATISS is to improve safety operation by integrating a parachute rescue system and a triple redundant autopilot system.

## Acknowledgement

The project described in this paper was supported by the federal state Brandenburg and the European Union by the EFRE-WiTet program [www.efre.brandenburg.de](http://www.efre.brandenburg.de).

The authors of MACS-TumbleCam want to thank especially the team of Neurorobotics Research Laboratory at the Humboldt-Universität zu Berlin who manufactured the sensor head frame and the motor control unit and the whole team of DLR OS-ASK who assembled, software engineered and post-processed all data.

Thanks also to the people from “Investitionsbank des Landes Brandenburg” ILB for their support of the SALSAs project.

## References

- CRAMER, M., HAALA, N., ROTHERMEL, M., LEINSS, B. & FRITSCH, D., 2013: UAV-gestützte Datenerfassung für Anwendungen der Landesvermessung – das Hessenheim-Projekt. – DGPF Tagungsband 22: 450–469.
- DANDERS, CH., 2007: Entwurf und Konstruktion der Flugmessdrohne ATISS. – Bachelor thesis, Technical University of Applied Sciences Wildau, 2007.
- EISENBEISS, H., 2009: UAV Photogrammetry. – Dissertation, Eidgenössische Technische Hochschule Zürich, Schweiz.
- HEINZE, N., ESSWEIN, M., KRÜGER, W. & SAUR, G., 2010: Image exploitation algorithms for reconnaissance and surveillance with UAV. – SPIE 7668, Airborne Intelligence, Surveillance, Reconnaissance (ISR) Systems and Applications VII, 76680U, April 26, 2010.
- KÜNG, O., STRECHA, C., BEYELER, A., ZUFFEREY, J.-C., FLOREANO, D., FUA, P. & GERVAIX, F., 2011a: The accuracy of automatic photogrammetric techniques on ultra-light uav imagery. – International Archives of the Photogrammetry, Remote Sensing and Spatial Information Sciences, ISPRS XXXVIII-1/C22: 125–130, Zurich, Switzerland.
- KÜNG, O., STRECHA, C., FUA, P., GURDAN, M., ACHTELIK, M., DOTH, K.-M. & STUMPF, J., 2011b: Simplified building models extraction from ultra-light UAV imagery. – International Archives of the Photogrammetry, Remote Sensing and Spatial Information Sciences, ISPRS XXXVIII-1/C22: 217–222, Zurich, Switzerland.
- LEHMANN, F., BERGER, R., BRAUCHLE, J., HEIN, D., MEISSNER, H., PLESS, S., STRACKENBROCK, B. & WIEDEN, A., 2011: MACS – Modular Airborne Camera System for Generating Photogrammetric High-Resolution Products. – PFG – Photogrammetrie, Fernerkundung, Geoinformation 2011 (6): 435–446.
- LI, Z. & LI, Y., 2011: Photogrammetric recording of ancient buildings by using unmanned helicopters – cases in China. – International Archives of the Photogrammetry, Remote Sensing and Spatial Information Sciences, ISPRS XXXVIII-1/C22: 189–193, Zurich, Switzerland.
- MATHWORKS, 2013: <http://www.mathworks.de/de/help/vision/ref/blockmatching.html> (24.5.2013).
- MEISSNER, H. & PLESS, S., 2011: MACS – Modular airborne camera system for generating photogrammetric high-resolution products. – PFG – Photogrammetrie, Fernerkundung, Geoinformation 2011 (6): 435–446.
- NEITZEL, F. & KLONOWSKI, J., 2011: Mobile 3D mapping with a low cost UAV system. – International Archives of the Photogrammetry, Remote Sensing and Spatial Information Sciences, ISPRS XXXVIII-1/C22: 39–44, Zurich, Switzerland.
- REMONDINO, F., BARAZZETTI, L., NEX, F., SCAIONI, M. & SARAZZI, D., 2011: UAV photogrammetry for mapping and 3d modelling – current status and

- future perspectives. – International Archives of the Photogrammetry, Remote Sensing and Spatial Information Sciences, ISPRS **XXXVIII-1/C22**: 25–31, Zurich, Switzerland.
- SEILER, I., 2013: Gemeinsame Grundsätze des Bundes und der Länder für die Erteilung der Erlaubnis zum Aufstieg von unbemannten Luftfahrtssystemen gemäß § 16 Absatz 1 Nummer 7 Luftverkehrs-Ordnung (LuftVO). – Bundesministerium für Verkehr, Bau und Stadtentwicklung, Referat LR 24, Bonn.
- WENZEL, K., ROTHERMEL, M., FRITSCH, D. & HAALA, N., 2013: Image acquisition and model selection for multi-view stereo. – International Archives of the Photogrammetry, Remote Sensing and Spatial Information Sciences, ISPRS **XL-5/W1**: 251–258, 3D-ARCH 2013, Trento, Italy.
- WIEDEN, A. & STEBNER, K., 2013: Referenzorientierung für Bilddaten aus Mehrkopfkamerasystemen. – DGPF Tagungsband **22**: 518–525.
- WIEDEN, A. & STEBNER, K., 2014: Accuracy Analysis for Automatic Orientation of a Tumbling Oblique Viewing Sensor System. – EuroCOW **2014**: 131–136, Barcelona, Spain.
- ZHANG, C. & KOVACS, J., 2012: The application of small unmanned aerial systems for precision agriculture: a review. – Precision Agriculture **13** (6): 693–712.

## Addresses of the Authors:

JÖRG BRAUCHLE & RALF BERGER, DLR, German Aerospace Center, Institute of Optical Sensor Systems, 12489 Berlin, Tel: +49-30-67055-274, -572, e-mail: {joerg.brauchle}{ralf.berger}@dlr.de

Prof. Dr.-Ing. WOLFGANG RÜTHER-KINDEL, University of Applied Sciences Wildau, Department of Aeronautical Engineering, Bahnhofstraße, 15745 Wildau, Tel: +49-3375-508613, e-mail: wkindel@th-wildau.de

Manuskript eingereicht: Oktober 2013

Angenommen: Mai 2014





# Hyperspectral Remote Sensing with the UAS “Stuttgarter Adler” – System Setup, Calibration and First Results

AXEL BÜTTNER & HANS-PETER RÖSER, Stuttgart

**Keywords:** hyperspectral, remote sensing, unmanned aerial system, direct georeferencing, calibration

**Summary:** The UAS “Stuttgarter Adler” was designed as a flexible and cost-effective remote-sensing platform for acquisition of high quality environmental data. Different missions for precision agriculture applications and BRDF-research have been successfully performed with a multispectral camera system and a spectrometer as main payloads. Currently, an imaging spectrometer is integrated in the UAS as a new payload, which enables the recording of hyperspectral data in more than 200 spectral bands in the visible and near infrared spectrum. The recording principle of the hyperspectral instrument is based on a pushbroom line scanner. Each line is stored as a matrix image with spectral information in one axis and spatial information in the other axis of the image. Besides a detailed specification of the system concept and instrument design, the calibration procedure of the hyperspectral sensor system is discussed and results of the laboratory calibration are presented. The complete processing chain of measurement data is described and first preliminary results of measurement-flights over agricultural test sites are presented.

**Zusammenfassung:** *Hyperspektrale Fernerkundung mit dem UAS „Stuttgarter Adler“ – Systemübersicht, Kalibrierung und erste Ergebnisse.* Am Institut für Raumfahrtssysteme (IRS) der Universität Stuttgart wurde in den letzten Jahren das UAS „Stuttgarter Adler“ als flexible Fernerkundungsplattform entwickelt und erfolgreich zur multispektralen Fernerkundung sowie für BRDF-Messungen eingesetzt. Aktuell befindet sich als neue Nutzlast ein abbildendes Spektrometer in der Erprobung. Dieses ermöglicht die Aufzeichnung von hyperspektralen Daten in über 200 Bändern im sichtbaren und nahen infraroten Spektralbereich. In diesem Beitrag wird die Integration und Inbetriebnahme des hyperspektralen Sensors als neue Nutzlast erläutert. Dabei werden neben einer detaillierten Beschreibung des Sensorsystems auf dessen radiometrische und spektrale Kalibrierung sowie das Prozessieren der Daten eingegangen und erste Erfahrungen und Ergebnisse des Systems im Einsatz diskutiert.

## 1 Introduction

Hyperspectral remote sensing data is of great interest in many different research topics and applications. It combines traditional 2D imaging remote sensing technology with classical spectroscopy and allows the acquisition of data with both, geometric and spectral high resolution. The large number of spectral bands provides the ability to derive biophysical and biochemical parameters from the quasi continuous visible and near infrared spectrum

(HABOUDANE et al. 2008), while the geometric resolution can be used for the creation of rectified image strips. In the last decades, hyperspectral remote sensing was mainly performed with airborne sensors such as AVIRIS or HyMap, which are employed on manned aircraft (GREEN et al. 1998, COCKS et al. 1998). The development of compact and lightweight imaging spectrometers in the last few years offers the possibility to integrate such instruments in small unmanned aerial systems (UAS) and closes the gap between time-con-

suming and spatially limited point measurements on the ground and complex and expensive flight campaigns with manned aircraft. Recent studies have investigated the integration of a hyperspectral pushbroom sensor in an UAS (HRUSKA et al. 2012) and shown the potentials of such a system for vegetation monitoring and water stress detection (e.g. BERNI et al. 2009, ZARCO-TEJADA et al. 2012, 2013). The UAS “Stuttgarter Adler” is operated as a remote sensing platform at the Institute of Space Systems and can be equipped with different sensor systems like multispectral and thermal cameras (KIRCHGAESSNER 2013). This paper shows the integration of an imaging spectrometer as hyperspectral payload in our UAS, including a detailed description of the system design and calibration concept of the instrument. Results of the laboratory calibration are presented and first results of measurement flights are discussed. A new approach for improving geometric correction and direct georeferencing is introduced.

## 2 System Overview

### 2.1 UAS “Stuttgarter Adler”

The UAS “Stuttgarter Adler” is a remote sensing platform, which was specially designed for acquiring high quality remote sensing data with great flexibility at comparatively low costs (PUTZE 2013). The twin-engine configuration with two 2.0 kW electrical engines has a wing-span of 4.33 m and allows a take-off weight of 25 kg including a payload capacity of 4 kg – 5 kg. The aerodynamic design ac-

**Tab. 1:** Technical data of the UAS.

Wing span	4.33 m
Total length	2.6 m
Max. take-off weight	25 kg
Electric Propulsion	2 x Polytec C42-60 2kW
Batteries	2x 10s2p 8000mAh LiPo
Payload capacity	4 kg – 5 kg
Flight Time	25 min – 30 min



**Fig. 1:** UAS “Stuttgarter Adler” before take-off.

counts for a stable flight at 12 m/s – 15 m/s air-speed. The radio link and all control surfaces are constructed in a redundant way so that no single point failure leads to loss of the aircraft. The integration of the motors in two nacelles provides enough space for the integration of the payload in the fuselage. Take-off and landing require a paved or grass runway of 150 m length and are performed manually with remote control. The flight itself is controlled autonomously by an autopilot system based on the open source project “paparazzi” (BRISSET 2006). The LiPo batteries allow a total flight-time of up to 30 minutes. An image of the UAS is shown in (Fig. 1) and the technical data are summarized in (Tab. 1).

### 2.2 Hyperspectral Sensor System

The hyperspectral imager consists of three main components, see (Fig. 2) (SPECTRAL IMAGING LTD. 2008). Incoming light is focused on the entrance-slit of the spectrograph by a special fore-lens (OLE9 forelens); a monochrome CCD-camera (Prosilica GE1900) is mounted on the back of the spectrograph to detect the radiance; the spectrograph itself (Specim Inspector V10E) disperses the light and focuses it on the CCD detector surface with a nominal spectral resolution of 2.8 nm. The 9 mm lens leads to a maximum field of view of 76.5° which is used for bidirectional reflectance distribution function (BRDF) research in combination with a BRDF ground measurements device (SCHWARZBACH 2012). Nominal measure-

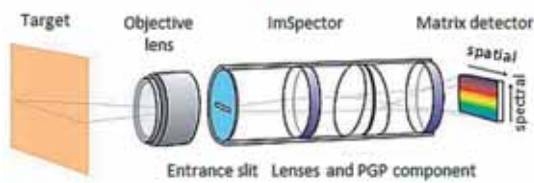


**Fig. 2:** Schematic of the imaging spectrograph.

ments are performed with  $60^\circ$  limited field of view (FOV) to reduce BRDF-effects. The main specifications of the spectrograph are summarized in (Tab. 2).

The hyperspectral imager is working as a pushbroom line scanner with the entrance slit oriented perpendicular to the flight direction. The constant movement of the UAS is used to scan an area in continuous strips. Each single line is stored as a matrix image, which contains spectral information in one dimension and spatial information in the other dimension of the image sensor. The geometric rectification of the image strips is a big challenge in operating a line scanner in an UAS. The small platform is susceptible to gusts of wind and much more unstable in comparison to large

manned aircraft. For correct alignment and rectification of the recorded lines, the position and attitude of the sensor must be known with high precision. Therefore, additional sensors for position and attitude determination are mounted on the spectrograph. To meet the requirements of small and light-weight components for the integration in the UAS, a position and attitude sensor system based on a three-axis micro-electromechanical system (MEMS) accelerometer, gyroscope and magnetometer in combination with a compact L1-GPS receiver providing carrier phase raw measurement data was chosen. A second stationary GPS receiver is used for differential processing against a base station. Barometer and thermometer as additional sensors were added for improving the height determination. The gyroscope used is an ITG-3200 triple-axes gyroscope from InvenSense providing three integrated 16-bit analog-to-digital converters (ADCs) for simultaneous sampling of the gyros. The accelerometer is an Analog Devices ADXL345 digital triaxial acceleration sensor with measurement range up to  $\pm 16$  g, which was designed for low power consumer market. The 13-bit resolution enables measurement of inclination changes smaller than  $0.5^\circ$ . The Honeywell HMC5883L triple-axes sensor is used as digital compass in the hardware setup. The 12-bit ADC enables measurements with milligauss resolution, which lead to a heading accuracy of  $1^\circ$ . An external professional grade global navigation satellite system (GNSS) antenna from Tallysman (TW 2410) is used for acquiring strong GPS signal and improved multipath rejection. The inertial data is recorded with 100 Hz, while the GPS receiver provides raw data with 20 Hz update rate. A small microprocessor board is used for synchronous sensor readout via fast-mode i2c digital interface, a precise GPS pulse-per-second time-signal serves as common time basis. Since no real-time capability is required, a specially designed extended Kalman filter with smoothing techniques is used for sensor fusion of inertial measurement unit (IMU) and GPS data in the post-processing to improve the overall accuracy (KOERNER 2012). The information flow of the tightly coupled filter is shown in (Fig. 3).

**Tab. 2:** Specification of the hyperspectral imager.

<b>Spectrograph</b>	
Spectral range	380 nm – 1100 nm
Spectral resolution	2.8 nm
Numerical aperture	F / 2.4
Slit width	30 $\mu$ m
Spatial resolution	rms spot radius < 9 $\mu$ m
<b>CCD camera and forelens</b>	
Resolution	1920 x 1080
Binning h/v	1–8 pixels / rows
Pixel Size	7.4 $\mu$ m x 7.4 $\mu$ m
Radiometric resolution	12 bit
Frame rate (full resolution)	up to 30 fps
Frame rate (2x binning)	up to 60 fps
Focal length	9 mm
Field of view (max.)	76.5° x 0.19°

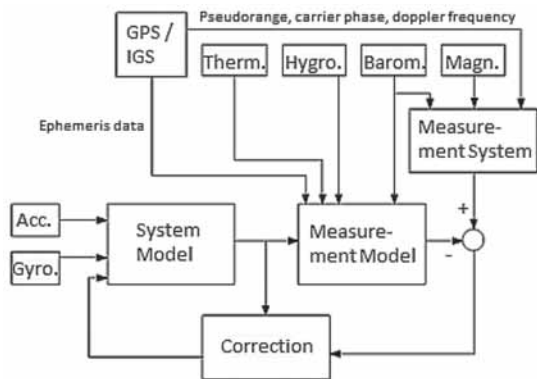


**Fig. 3:** Information flow of the extended Kalman filter.

The whole sensor system is fixed horizontally on a common mounting plate. An optical mirror reflects the incoming light to the fore-lens. Expanded polypropylene-foam is used for vibration isolation from the aircraft. The IMU is mounted directly on top of the spectrometer to keep the position and orientation offset as constant and small as possible. The GPS-antenna is mounted on top of the aircraft right above the instrument for best reception of the GPS satellite signals. A compact PC with Linux operating system, Gigabit-Ethernet interface and solid-state disk for data storage is used as on-board payload computer. Custom software for configuration of the camera and recording of the image data was developed, which enables flexible adjustments of different sensor parameters such as frame rate, binning and exposure time for particular missions.

### 3 Calibration Concept and Data Processing

Radiometric and spectral calibration is performed in-house in an optical laboratory. Different calibration equipment such as an integrating sphere, line emission lamps and a monochromator are available for regular calibration in the laboratory between measurement campaigns. The whole system including mounting plate and mirror is calibrated together to account for possible distortions of the additional components. The results of the

laboratory calibration are used for radiometric pre-processing after measurement flights.

#### 3.1 Radiometric Calibration

The main task of radiometric calibration is the determination of the coefficients for the conversion of raw data (DN) into physical units (spectral radiance,  $\text{mW} / (\text{m}^2 \cdot \text{sr} \cdot \text{nm})$ ). In addition, vignetting effects and sensor inhomogeneities due to slightly varying sensitivities of the CCD elements are corrected. An integrating sphere, which is regularly calibrated against the German national standard (PTB), is used as homogeneous light-source with known spectral radiance. It has a diameter of 500 mm with an output port diameter of 100 mm and is illuminated with a 50 W QTH lamp. The calibration is valid for the spectral range from 380 nm to 1100 nm with a relative uncertainty of 5%. For the determination of the sensor linearity, the integrating sphere is equipped with an adjustable slit in front of the QTH lamp and an optometer for measuring the total radiance. The linearity of the radiometric response function is measured by increasing the luminosity up to saturation level at different integration times. Results show deviations from the linear model to be smaller than 1%, so a linear model is assumed. Dark signal is quantified in the laboratory for different temperatures and integration times to characterize the dark signal non uniformity (DSNU). Noise equivalent spectral radiance (NESR) is determined by measuring the stan-

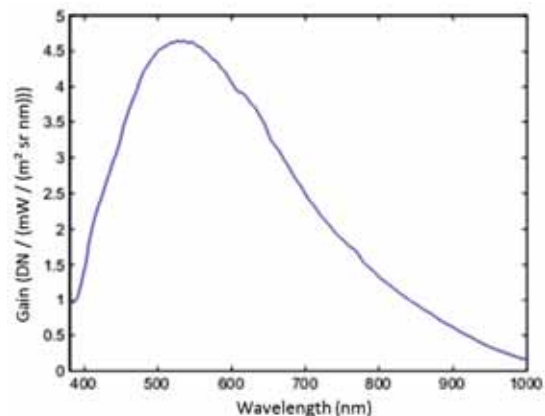


**Fig. 4:** Radiometric calibration coefficient.

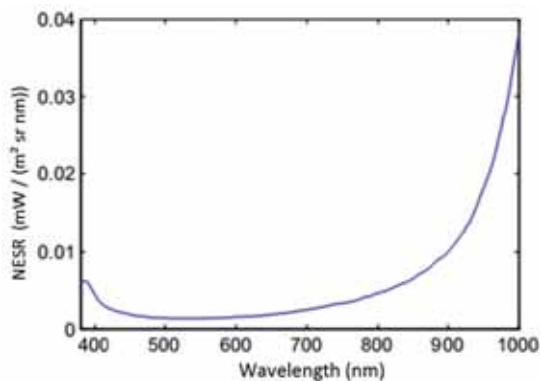


**Fig. 5:** Noise equivalent spectral radiance for 1 ms integration time.

standard deviation of the dark signal and performing radiometric calibration with the radiometric calibration coefficient. It can be used for signal-to-noise ratio (SNR) analysis. The radiometric calibration coefficient for the centre pixel is shown in Fig. 4. The corresponding NESR for an integration time of 1 ms is shown in Fig. 5. The spectral region above 1000 nm is strongly influenced by system noise due to the low quantum efficiency of the CCD-sensor in this region and therefore discarded in further data analysis.

### 3.2 Spectral Calibration

Spectral calibration is needed to successfully derive reflectance spectra or physical parameters of measurement targets. It describes the response of the sensor to discrete light of known wavelength and is used to determine the centre wavelengths and spectral resolution for each spectral channel. The response function of each channel can be approximated with a Gaussian curve, the spectral resolution is defined as the full width half maximum (FWHM) of the function. The peak response of the spectrometer to an infinitesimally narrow emission line describes the centre wavelength of each channel. Special line emission lamps with different gas fills are used to produce narrow, intense lines from the excitation of the gases. Measurements with HgAr-, Xe- and Ne-gas lamps provide emission lines, which cover the whole spectral range of interest. The line width of the emission lines

is much smaller than the spectral resolution of the spectrograph and thus well suited for wavelength calibration (CHEN 1997). Fig. 6 shows the response of the centre channels on the spatial axis to the Xenon lines, in Fig. 7 the 4th order polynomial-fit for the wavelength calibration of the spectral channels is shown. The nominal spectral resolution of the spectrograph is stated as 2.8 nm by the manufacturer. The 1080 spectral pixels of the CCD-Sensor are binned with the factor of 3 which leads to a subset of 331 spectral channels in the 380 nm – 1100 nm region with a spectral sampling interval of approximately 2.2 nm. An Oriel Cornerstone monochromator with a spectral resolution of 0.5 nm is used for sensitivity analysis of adjacent pixels to monochromatic light with 0.1 nm increment. Results of the measurements with line emission lamps and monochromator showed a FWHM between 3.2 nm and 4.7 nm for the binned configuration, depending on the spec-

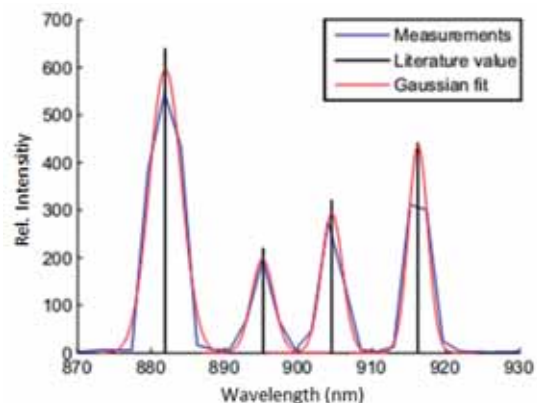


**Fig. 6:** Measurement of Xenon lines.

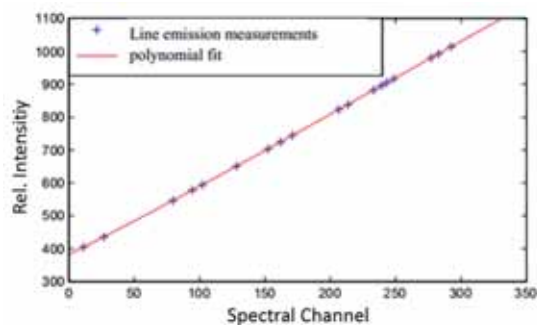


**Fig. 7:** Wavelength calibration with line emission lamps.

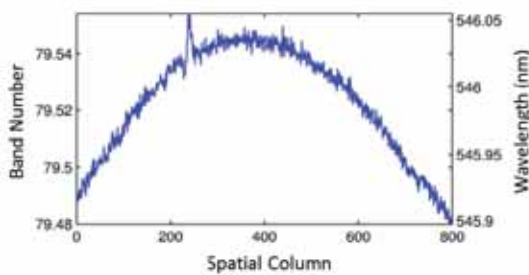


**Fig. 8:** Band position and according wavelength of the 546 nm Hg emission line.

tral channel. In unbinned mode, the FWHM is in the same order of magnitude. Thus, the binning reduces the data volume and increases the SNR without losing spectral information. The bending of spectral lines across the spatial axis (spectral smile) is investigated by comparison of the peak response of all spatial pixels to monochromatic light. Fig. 8 shows a variation of less than 0.1 pixels (3x binned) along the spatial axis for the 546 nm Hg emission line, which is equivalent to 0.2 nm. The bending of spatial lines across spectral axis (keystone) is given by the manufacturer to be smaller than  $5 \mu\text{m}$  which is 0.34 pixels at 2x spatial binning.

### 3.3 Data processing

The results of the laboratory calibration are used for radiometric pre-processing after measurement flights. In a first step, the raw data are corrected for dark signal and can then be converted to spectral radiance by applying the radiometric calibration coefficients. Afterwards, atmospheric distortions have to be corrected. This is done using radiative transfer tools based on the open source software package libRadtran with the core radiative transfer tool uvspec (MAYER & KYLLING 2005). Besides time, date and location, further input-parameters like temperature and humidity are measured during flight time. In addition, a sun-photometer is used to measure the aerosol-optical depth. Based on the spectral calibration of the hyperspectral instrument, a sensor specific wavelength-grid is defined for the numerical calculation of ground and path ra-

diance. As an alternative method, the reflected radiance of a calibrated diffuse grey reference panel with 50% reflectance level can be measured before and after a flight. Reference values are calculated through linear interpolation for the whole flight to derive reflectance values. The linear interpolation method is suitable for stable weather conditions and flight times shorter than 30 minutes (MIURA & HUETE 2009). Finally, geometric rectification and georeferencing have to be performed. Position and attitude of the aircraft are calculated in post-processing with 100 Hz. The beginning and end of each image strip is triggered by the autopilot and marked with a GPS timestamp. A camera-timestamp is stored in every single line-image and used for connecting the images with the position and attitude of the UAS at each exposure. Based on the collinearity equations, custom software was developed for direct georeferencing of the image strips in UTM coordinates on flat terrain or digital elevation model. The correction of boresight angles is implemented with a differential rotation matrix. Final data is stored in ENVI-compatible format and can be further processed with classical remote sensing software packets.

## 4 Results and Discussion

In early 2012, first test flights were performed to prove the system under operational conditions. Parameters like frame rate, exposure time and flight speed were adapted to avoid gaps in image strips. IMU and GPS measurements of the test flights were used for tuning of the Kalman-filter. Tab. 3 shows typical parameters for sensor operation during measurements. In the summer of 2012, the first measurement flights over agricultural test fields were performed. The flight altitude was 300 m above ground. A frame rate of 20 fps and an average ground speed of 15 m/s lead to a ground sampling distance of  $0.5 \text{ m} \times 1 \text{ m}$ . The data were spatially resampled with nearest neighbour method to match a  $1 \text{ m} \times 1 \text{ m}$  UTM grid. Fig. 9 shows an OpenStreetMap aerial photo which is overlaid with a part of a radiometrically calibrated hyperspectral image-strip in RGB-representation.

The hyperspectral image section covers different areas like forest, bare soil or asphalt. As no additional atmospheric measurements were taken on this day, reflectance spectra

**Tab. 3:** Typical parameters for measurement flights.

Flight altitude above ground level	100 m – 300 m
Spatial binning	2x
Spatial pixel	800
FOV/IFOV	1.16 rad/1.45 mrad
Ground sampling distance (GSD)*	0.5 m x 1 m
Swath width*	395 m
Swath length**	1000 m
Spectral binning	3x
Spectral channels	331
Spectral range	380 nm – 1100 nm
Spectral sampling	2.2 nm
Flight time	25 min – 30 min
* valid for 300 m flight altitude	
** limited through line of sight regulation	



**Fig. 9:** Image strip in RGB-representation; map: ©OpenStreetMap.

were calculated based on the reference panel method. Three pre-processed reflectance spectra, which were directly extracted from single pixels of the image in Fig. 9, are shown in Fig. 10. The vegetation reflectance spectrum shows the typical maximum in the green wavelength along with the significant red edge transition zone between visible and near infrared wavelength. These features provide the basis for further investigations like estimation of chlorophyll content, leaf area index or other biophysical parameters (LIU et al. 2004). Also, heterogeneities within one agricultural field are visible and can be utilized for estimating yields or variable-rate application of nitrogen. Reference ground spectra were obtained with an Avantes AvaSpec-128 fibre optic spectrometer for the wavelength region of 500 nm – 1000 nm to prove the spectral image quality. Fig. 11 shows a comparison of UAS and ground measurements for bare soil. The

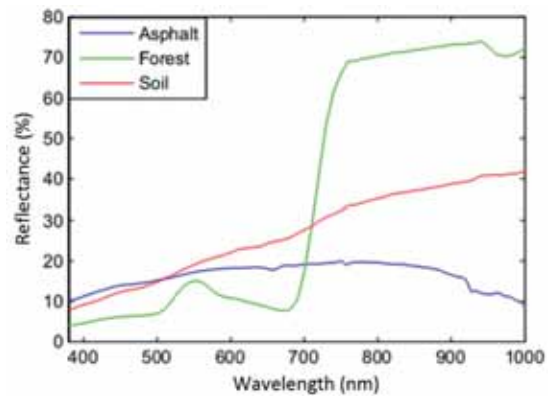


**Fig. 10:** Reflectance spectra for asphalt, forest and soil.

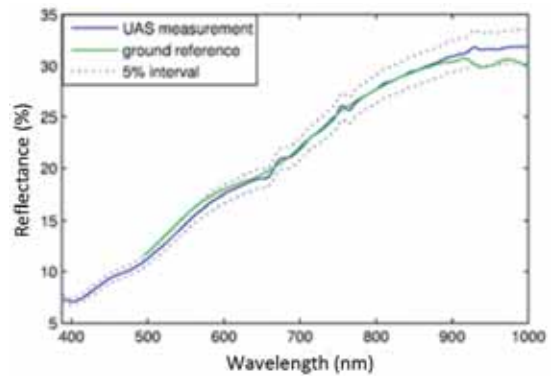


**Fig. 11:** Comparison of ground and airborne measurements of bare soil.

results show a good congruency between both measurements and confirm the high spectral quality of the UAS hyperspectral data. The relative difference between both measurements is smaller than 5%.

The hyperspectral image strip in Fig. 9 was directly georeferenced after post-processing of IMU and GPS data. It can be seen, that there are still geometric distortions which are not corrected properly. Deviations from the aerial image lie in the range of 1 m – 10 m and are particularly noticeable on straight lines like the north-south street between the forest and the field in Fig. 9. The street shows typical S-shaped distortions, which are most likely the result from limited accuracy of the MEMS-sensors. Other studies experienced similar problems with direct georeferencing of line scanner imagery based on lightweight

MEMS sensors (HRUSKA et al. 2012). To increase the accuracy of georeferencing, a new approach is currently adopted. An additional industrial matrix camera, which is triggered synchronously to the line scanner, was integrated in the UAS. It offers the possibility to evaluate very high overlapping images with classical photogrammetric techniques and calculate the exterior orientations of the camera. The orientation can then be used in the direct georeferencing process of the line scanner. Estimations of the Kalman filter are applied as initial values for the exterior orientation of the matrix camera. First tests with the additional camera already show very promising results. Fig. 12 shows a hyperspectral image strip, which is geocorrected based on GPS/IMU measurements (top) and based on exterior orientation of the additional matrix camera (bottom). It can be seen, that geometric distortions are significantly reduced with the integration of the matrix camera. Detailed accuracy assessment of the geometric performance with measurement and analysis of ground control points will be performed in the near future.



**Fig. 12:** Direct georeferencing based on GPS/IMU (top) and exterior camera orientation (bottom).

## 5 Conclusion and Outlook

In this study, we developed a new light-weight hyperspectral sensor system for use on an UAS. The motivation for the study was to enable the recording of high spatial and spectral resolution imagery in the visible and near infrared spectrum, with high temporal flexibility at low operational costs. The system was successfully integrated in the remote sensing platform “Stuttgarter Adler” and showed the ability to acquire spatially detailed and high quality spectral remote sensing data. Based on calibration methods in the laboratory and reference field measurements, a complete processing chain was developed to generate a radiometric and spectral calibrated image. Exemplary reflectance spectra from first measurement flights have been presented in this paper. A comparison with ground measurements confirmed the good spectral performance of the instrument and showed the potential to provide detailed spectral information to scientists and users. Orthorectification methods were implemented for direct geore-

ferencing of the image strips based on post-processing of IMU and GPS measurements. First results indicated geometric distortions after orthorectification in the range of 1 m – 10 m. To increase the geometric accuracy, a new approach for direct georeferencing, including an additional matrix camera, is proposed. A similar approach has been successfully implemented by WALLACE et al. 2012 for direct georeferencing of LIDAR point clouds. For absolute accuracy assessment and bore-sight alignment determination, measurements with ground control points and overlapping flight lines in cross formation have to be performed. In cooperation with the Institute of Crop Science of the University of Hohenheim, hyperspectral remote sensing data shall be used for the determination of spectral characteristics of winter wheat and compared with ground based measurements in the upcoming vegetation period.

## References

- BRISSET, P., 2006: The Paparazzi solution. – European Micro Air Vehicle Conference and Flight Competition, EMVA 2006, Braunschweig.
- BERNI, J., ZARCO-TEJADA, P.J., SUAREZ, L. & FERERES, E., 2009: Thermal and Narrowband Multispectral Remote Sensing for Vegetation Monitoring From an Unmanned Aerial Vehicle. – *IEEE Transactions on Geoscience and Remote Sensing* **47** (3): 722–738.
- CHEN, H., 1997: Remote sensing calibration systems: An introduction. – *Studies on geophysical optics and remote sensing*, A. Deepak Publishing, Hampton, Virginia, USA.
- COCKS, T., JENSSSEN, R., STEWART, A., WILSON, I. & SHIELDS, T., 1998: The HyMap airborne hyperspectral sensor: The system, calibration and performance. – *1st EARSeL Workshop on Imaging Spectrometry*: 37–42.
- GREEN, R.O., EASTWOOD, M.L., SARTURE, C.M., CHRIEN, T.G., ARONSSON, M., CHIPPENDALE, B.J., FAUST, J.A., PAVRI, B.E., CHOVIT, C.J., SOLIS, M., OLAH, M.R. & WILLIAMS, O., 1998: Imaging spectroscopy and the airborne visible/infrared imaging spectrometer AVIRIS. – *Remote Sensing of Environment* **65** (3): 227–248.
- HABOUDANE, D., TREMBLAY, N., MILLER, J. & VIGNEAULT, P., 2008: Remote estimation of crop chlorophyll content using spectral indices derived from hyperspectral data. – *Geoscience and Remote Sensing, IEEE Transactions on* **46** (2): 423–437.
- HRUSKA, R., MITCHELL, J., ANDERSON, M. & GLENN, N.F., 2012: Radiometric and Geometric Analysis of Hyperspectral Imagery Acquired from an Unmanned Aerial Vehicle. – *Remote Sensing* **4** (9): 2736–2752.
- KIRCHGAESSNER, U., 2013: Einsatz eines ferngesteuerten Kleinflugzeugs zur Erfassung von Umweltdaten. – Dissertation, University of Stuttgart.
- KOERNER, F., 2012: Design of a Kalman Filter for Tightly Coupled GPS/INS Integration. – Diploma thesis, University of Stuttgart.
- LIU, J., MILLER, J., HABOUDANE, D. & PATTEY, E., 2004: Exploring the relationship between red edge parameters and crop variables for precision agriculture. – *IEEE International Geoscience and Remote Sensing Symposium* **2**: 1276–1279.
- MAYER, B. & KYLLING, A., 2005: Technical note: The libRadtran software package for radiative transfer calculations – description and examples of use. – *Atmospheric Chemistry and Physics* **5**: 1855–1877.
- MIURA, T. & HUETE, A.R., 2009: Performance of Three Reflectance Calibration Methods for Airborne Hyperspectral Spectrometer Data. – *Sensors* **9** (2): 794–813.
- PUTZE, U., 2013: Auslegung und Instrumentierung eines ferngesteuerten Kleinflugzeugs für die Erdbeobachtung. – Dissertation, University of Stuttgart.
- SCHWARZBACH, M., 2012: Konstruktion und Erprobung eines Bodengerätes zur Messung der BRDF unter natürlichen Beleuchtungsbedingungen. – Dissertation, University of Stuttgart.
- SPECTRAL IMAGING LTD., 2008: ImSpector imaging spectrograph user manual.
- WALLACE, L., LUCIEER, A., WATSON, C. & TURNER, D., 2012: Development of a UAV-LiDAR System with Application to Forest Inventory. – *Remote Sensing* **4** (6): 1519–1543.
- ZARCO-TEJADA, P.J., GONZÁLEZ-DUGO, V. & BERNI, J.A.J., 2012: Fluorescence, temperature and narrow-band indices acquired from a UAV platform for water stress detection using a micro-hyperspectral imager and a thermal camera. – *Remote Sensing of Environment* **117**: 322–337.
- ZARCO-TEJADA, P.J., GUILLÉN-CLIMENT, M.L., HERNÁNDEZ-CLEMENTE, R., CATALINA, A., GONZÁLEZ, M.R. & MARTÍN, P., 2013: Estimating leaf carotenoid content in vineyards using high resolution hyperspectral imagery acquired from an unmanned aerial vehicle (UAV). – *Agricultural and Forest Meteorology* **171–172**: 281–294.

## Addresses of the Authors:

Dipl.-Ing. AXEL BÜTTNER & Prof. Dr. rer. nat. HANS-PETER RÖSER, Universität Stuttgart, Institut für Raumfahrtssysteme, Pfaffenwaldring 29, D-70569 Stuttgart, Tel.: +49-711-685-62056, Fax: +49-711-685-52056, e-mail: {buettner}{roeser}@irs.uni-stuttgart.de

Manuskript eingereicht: Oktober 2013

Angenommen: März 2014



# The Effect of Vegetation Type and Density on X-Band SAR Backscatter after Forest Fires

EVA-MARIA BERNHARD, ANDRÉ TWELE & SANDRO MARTINIS, Oberpfaffenhofen

**Keywords:** forest fire, TerraSAR-X, backscatter analysis, change detection

**Summary:** Various frequencies, e.g. visible light, infrared, and microwaves, from remote sensing sensors can be used for active fire mapping, forest fire detection and fire emission assessment. However, little is known about the applicability of X-band SAR data for burned area detection. This paper presents a detailed SAR backscatter coefficient analysis and accuracy assessment with respect to CORINE 2006 land cover data. For this purpose five forest fires have been analysed. Dry as well as wet acquisition conditions have been taken into account. The analysis demonstrated that the largest differences in backscatter coefficients between pre- and post-fire conditions were linked to tall and dense vegetation types. Contrarily, scant vegetation was marked by lowest signal differences. High correlation coefficients have been obtained from regression analysis between vegetation indices and SAR backscatter changes. Moreover, a burned area classification algorithm with different thresholds for each vegetation type has been applied. The classification result illustrated that areas abundantly covered with vegetation showed classification accuracies of ~91%, whereas sparse vegetation achieved ~5% accuracies.

**Zusammenfassung:** Der Einfluss von Vegetationstyp und -dichte auf das Rückstreuverhalten von X-Band Radar nach Waldbränden. Verschiedene Frequenzen, z.B. sichtbares Licht, Infrarot und Mikrowellen, von Fernerkundungssensoren können zur Feuererfassung, der Brandflächendetektion oder zur Abschätzung von Emissionen genutzt werden. Allerdings ist nur wenig über die Eignung von X-Band Radardaten zur Brandflächendetektion bekannt. Daher präsentiert diese Studie eine detaillierte Analyse des Radar Rückstreuverhaltens über diversen Landbedeckungen (nach CORINE 2006). Fünf verschiedene Gebiete sind unter unterschiedlichen Witterungsbedingungen (trocken und nass) untersucht worden. Die Studie zeigt, dass die größten Unterschiede der Rückstreuoeffizienten – vor und nach dem Brandereignis – in Gebieten mit hochwachsender und dichter Vegetation auftreten, wohingegen Gebiete mit spärlicher Vegetation nur geringe Unterschiede aufweisen. Ebenso erzielen die Regressionskoeffizienten zwischen Vegetationsindizes und der Veränderung des Radar Rückstreusignals hohe Übereinstimmungen. Darüber hinaus wurde ein Klassifikationsalgorithmus für Brandflächen angewandt, der auf individuellen Schwellwerten für jeden Vegetationstyp basiert. Die Klassifikationsergebnisse zeigten, dass dicht bewachsene Gebiete Klassifikationsgenauigkeiten von bis zu 91% aufwiesen, wohingegen spärlich bewachsene Bereiche Klassifikationsgenauigkeiten von 5% erreichten.

## 1 Introduction

Forest fires have always been a natural component of the Mediterranean ecosystem regulating the evolution, productivity and biodiversity of vegetation (MARGARIS et al. 1996, VIEGAS et al. 2009). Nevertheless, the European Mediterranean region has suffered from

an increasing number of large fire events (JUSTICE & KORONZTI 2001). These trends of environmental disasters are due to climate change and socio economic changes expected to continue and intensify in future (JUSTICE & KORONZTI 2001, LEONE 2009, WASTL et al. 2012). On the contrary, an increase in the construction of wildland urban interfaces, the devel-

opment of tourist infrastructure and pressure from tourism activities amplify the risk of man-induced fires (VIEGAS et al. 2009). As a consequence, the role of burned area detection and post fire monitoring are of eminent importance to support fire fighters on site and quantify environmental damage of the ecosystem. Spaceborne remote sensing can contribute to pre-, active and post-disaster mapping with an almost global coverage. While mainly medium resolution optical or thermal sensors, e.g. MODIS and MSG-SEVIRI, are being used for active fire detection (JUSTICE et al. 2002, AM-RAOUI et al. 2010), burned area mapping can be performed with high and very high resolution imaging techniques. However, the applicability of optical data can be severely limited due to persistent cloud coverage, haze or smoke plumes. An alternative method for burned area detection lies in the use of synthetic aperture radar (SAR) data where measurements in the microwave regime can overcome the reported problems. Several studies have been carried out in boreal forests using C-band SAR data (KASISCHKE et al. 1992, FRENCH et al. 1996, BOURGÉAU-CHAVEZ et al. 1997, BOURGÉAU-CHAVEZ et al. 2002). In addition, the impact of different forest types on burned area detection have been studied for tropical rain forests (SIEGERT & RÜCKER 2000), wetlands (marshes and forest mix) (KARSZENBAUM et al. 2003), or savanna woodlands (MENGES et al. 2004). These studies found evidence for a change in backscatter signal (C-, L-, and P-band data) between burned and unburned areas, mainly influenced by soil moisture and the exposure of a rough ground surface. Only few studies were undertaken in the European Mediterranean semi-arid environment, where precipitation during the fire season is rare, and the lack of rain reduces backscatter variability due to changes in soil moisture (TANASE et al. 2010a). Promising results could be achieved using C-band SAR data for burned area detection (GIMENO et al. 2003, GIMENO et al. 2004a, GIMENO et al. 2004b). The burned areas were distinguishable regardless of rainfall, although the wet season showed higher backscatter values than the dry season. TANASE et al. (2010a, 2010b, 2010c) confirmed the utility of X-, C-, and L- band data for fire severity assessment in dry and wet environmental conditions.

Moreover, BERNHARD et al. (2011) confirmed the detection capabilities of X-band SAR data for burned area mapping. This analysis was undertaken in La Palma and Grammatico, and indicated that the backscatter coefficient could be influenced by pre-fire vegetation. Since X-band microwaves cannot penetrate as deeply into vegetation cover as C-, L- or P-band, the incident beam interacts to a large extent with tree crowns (HOEKMANN et al. 1987). The attenuation through the forest canopy depends on stand density, canopy architecture (like crown closure, crown shape) and the incidence angle of the sensor (HOEKMANN et al. 1987). PULLIAINEN et al. (1993) showed that the transmissivity of X-band backscatter decreases nearly exponentially with increasing stem volume, whereas the soil backscatter contribution decreases (almost linearly) with stem volume. This indicates that the magnitude of backscatter changes after forest fires could be related to pre-fire vegetation characteristics.

This study substantially extends and complements the previous findings (BERNHARD et al. 2011) by taking additional study sites, i.e. Alto Trans-os-Montes, Dos Aguas and Andilla, into account, enhancing the classification algorithm and investigating in more detail the influence of pre-fire vegetation type and density on backscatter coefficients and classification results. Further, the data used in this study are acquired under dry and wet environmental conditions, which allowed determining SAR backscatter behaviour not only with respect to the vegetation structure, but also with respect to the impact of precipitation.

## 2 Study Sites

Five different study sites – the Canary Island of La Palma (Spain), Alto Trans-os-Montes (Portugal), Dos Aguas (Spain), Andilla (Spain), and Grammatico (Greece) – have been selected for this study. Fig. 1 shows an overview of the study areas including a composite of SAR pre- and post-disaster images. The fire scars for each scene are shown in red, whereas unburned areas appear in grey. The study site La Palma is not geographically located in the European Mediterranean, but shows comparative vegetation and landscape

characteristics like the other study areas. The fires in La Palma occurred in the beginning of August 2009 in the south of the island and destroyed an area of approximately 2.200 ha. La Palma is characterized by a strong relief with steep slopes and an elevation ranging up to 1.900 m above sea level (a.s.l.). An area of approximately 1.300 ha was destroyed by forest fires in the region of Alto Trans-os-Montes located in the North of Portugal between the end of August 2011 and the beginning of September 2011. The Alto Trans-os-Montes region is marked by an undulating relief with elevations reaching from 400 m up to 1.150 m a.s.l. Two fires near Valencia (Andilla and Dos Aguas) affected more than 36.000 ha. Both fires started at the end of June 2012 and lasted until the beginning of July 2012. The relief ranges from approximately 690 m – 1.320 m in Andilla and 100 m – 900 m in Dos Aguas. The fires in the study site Grammatico occurred at the end of August 2009, 30 km northeast of Athens and destroyed approximately 12.800 ha. Grammatico is characterized by a smooth terrain, ranging from 0 m to 500 m a.s.l. All study areas are dominated by typical Mediterranean vegetation types (see Tab. 1) and a Mediterranean climate with dry and hot summers where the rainy season is concentrated around winter and spring.

### 3 Dataset

The dataset consists of five pairs of single-polarized horizontal transmitted and horizontal

received (HH) TerraSAR-X images, acquired with the same acquisition parameters before and after forest fire occurrence. To consider the consequence of rainfall on the backscatter coefficient, TerraSAR-X scenes were ordered for dry as well as for wet environmental conditions. More detailed information on the datasets is given in Tab. 2. The SAR images were ordered in single-look slant-range complex (SSC), or enhanced ellipsoid corrected (EEC) format. The science orbit (TerraSAR-X 2012) was chosen for the highest orbital precision. The pre-processing was performed in six steps including multilooking (SSC data), co-registration, speckle filtering (Gamma-DE-MAP), geocoding, radiometric calibration and radiometric normalization using the SARscape 4.4 software (SARscape 2012). All data were converted to the radar backscatter coefficient sigma nought (dB).

Optical satellite images, CORINE 2006 land cover classification and precipitation information were collected and used as reference data. Post-disaster optical images were available for each study site. Furthermore, an optical pre-fire image was obtained for La Palma. Pre-processing steps applied to the optical images include orthorectification, pan-sharpening, atmospheric correction and co-registration to the TerraSAR-X images. The burned areas of all study sites were derived semi-automatically in the optical images. The classification workflow consists of an object-based procedure utilizing the indices modified soil adjusted vegetation index (MSAVI), burned area index (BAI) and normalized difference veg-

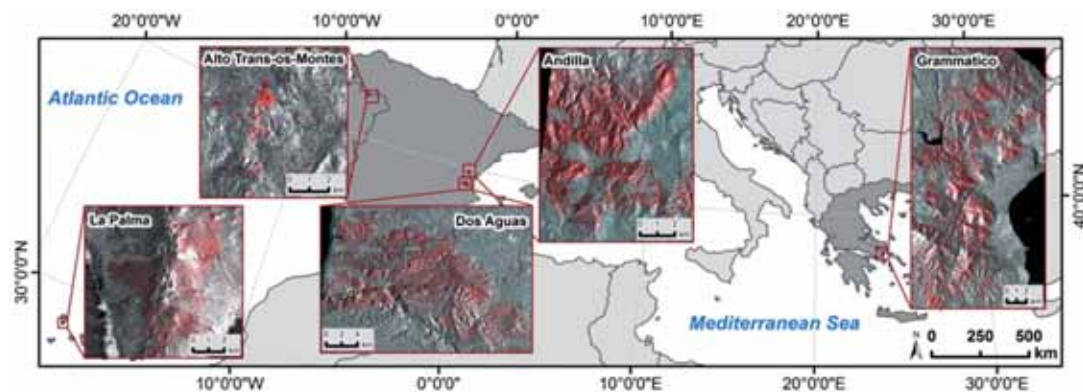


**Fig. 1:** Fire affected areas of the study sites are highlighted in red (RGB combination: red = change layer, green = pre-disaster image, blue = post-disaster image).

**Tab. 1:** Specification of CORINE 2006 land cover classification (CLC) (burned areas only).

Code	Vegetation class	Vegetation types
211	non-irrigated arable land	cereals, legumes, fodder crops, root crops and fallow land, tobacco, sugar cane; includes flowers and fruit trees (nurseries cultivation) and vegetables, whether open field, under plastic or glass (includes market gardening);
212	permanently irrigated land	crops irrigated permanently or periodically, using a permanent infrastructure (which is excluded in the class); most of these crops cannot be cultivated without an artificial water supply;
221	vineyards	areas planted with vines;
222	fruit trees and berry plantation	parcels planted with fruit trees or shrubs; single or mixed fruit species, fruit trees associated with permanently grassed surfaces; includes chestnut and walnut groves; ligneous crops, berry shrubs;
223	olive groves	areas planted with olive trees, including mixed occurrence of olive trees and vines on the same parcel;
231	pastures	dense grass cover, of floral composition, dominated by graminacea, not under rotation system; mainly for grazing, but the fodder may be harvested mechanically; includes areas with hedges; scattered trees and shrubs (10% - 20% of surface)
242	complex cultivation patterns	juxtaposition of small parcels of diverse annual crops, pasture and/or permanent crops; small parcels of annual crops (fruit trees, berry plantations, vineyards and olive groves), city garden pastures, fallow land;
243	land principally occupied by agriculture	areas principally occupied by agriculture, interspersed with significant natural areas; parcels of arable land, parcels of orchards, parcels of the rest of natural forests, groups of trees and shrubs (all smaller than 25 ha);
311	broad-leaved forest	vegetation formation composed principally of trees, including shrub and bush understoreys, where broad-leaved species predominate; young plantation of deciduous trees, walnut trees and chestnut trees, sparse broad-leaved forest with a 30% - 60% bracket of crown cover; quercus ilex, quercus suber, quercus rotondifolio;
312	coniferous forest	vegetation formation composed principally of trees, including shrub and bush understoreys, where coniferous species predominate; larch trees, arborescent matorral with dominating Juniperus oxycedrus/phoenica;
313	mixed forest	vegetation formation composed principally of trees, including shrub and bush understoreys, where neither broad-leaved nor coniferous species predominate;
321	natural grassland	low productivity grassland; often situated in areas of rough, uneven ground; frequently includes rocky areas, briars and heathland; herbaceous vegetation; karstic areas, military training fields, areas of shrub formations of scattered trees;
322	moors and heathland	vegetation with low and closed cover, dominated by bushes, shrubs and herbaceous plants (heather, briars, broom, gorse, laburnum), dwarf forest with a 3 m maximum height, pinus mugo coverage, prostrate, box trees, gorse;
323	sclerophyllous vegetation	bushy sclerophyllous vegetation, includes maquis and garrigue; in case of shrub vegetation areas composed of sclerophyllous species, such as Juniperus oxycedrus and heathland species
324	transitional woodland shrub	bushy or herbaceous vegetation with scattered trees; can represent either woodland degradation or forest regeneration/recolonisation; e.g young broad-leaved and coniferous wood species with herbaceous vegetation
332	bare rock	scree, cliffs, rock outcrops, including active erosion, rocks and reef flats situated above the high-water mark; sparsely vegetated areas where 75% of the land surface is covered by rocks;
333	sparsely vegetated areas	includes steppes, tundra and badlands; scattered high-altitude vegetation, gramineous and/or ligneous and semi-ligneous species; e.g. Artemisia spp., Stipa spp.

**Tab. 2:** Available dataset.

Study site	Sensor	Date	Fire condition	Modus	Optical bands / polarization	Precipitation* Date / Amount	Incidence angle
Alto Trans-os-Montes	WorldView2	28.8.2011	Post-fire	-	coastal, blue, green, yellow, red, red-edge, NIR I, NIR II	-	-
	TerraSAR-X	12.8.2011	Pre-fire	ScanSAR	HH		27.7°
	TerraSAR-X	3.9.2011	Post-fire	ScanSAR	HH		27.6°
Andilla	WorldView2	6.7.2012	Post-fire	-	coastal, blue, green, yellow, red, red-edge, NIR I, NIR II	1.7.2012 / 2.5 mm	-
	TerraSAR-X	12.4.2012	Pre-fire	StripMap	HH		37.2°
	TerraSAR-X	9.7.2012	Post-fire	StripMap	HH		35.3°
Dos Aguas	WorldView2	4.7./6.7.2012	Post-fire	-	coastal, blue, green, yellow, red, red-edge, NIR I, NIR II	20.3.2012 / 58.9 mm	-
	TerraSAR-X	21.3.2012	Pre-fire	StripMap	HH	21.3.2012 / 4.8 mm	35.2°
	TerraSAR-X	9.7.2012	Post-fire	StripMap	HH		35.3°
La Palma	SPOT5	30.7.2007	Pre-fire	-	green, red, NIR, SWIR	-	-
	SPOT5	7.8.2009	Post-fire	-	green, red, NIR, SWIR	-	-
	TerraSAR-X	13.12.2007	Pre-fire	StripMap	HH		33.4°
	TerraSAR-X	9.8.2009	Post-fire	StripMap	HH		33.4°
Grammatico	SPOT5	25.8.2009	Post-fire	-	green, red, NIR, SWIR	-	-
	TerraSAR-X	8.3.2009	Pre-fire	StripMap	HH		31.2°
	TerraSAR-X	31.8.2009	Post-fire	StripMap	HH		31.2°

\*www.wunderground.com (26.2.2013)

etation index (NDVI) in case a mid-infrared band was available. Additionally, all burned areas were screened and corrected by visual analysis. CORINE 2006 was created during 2005 – 2007 on the basis of SPOT4 VHR, SPOT5 VHR and IRS-P6-LISS-III data and reaches a classification accuracy of more than 85% (BÜTTNER & KOSZTRA 2007). The minimum mapping unit for CORINE is 25 ha for a single vegetation type. Thus, areas covered by various vegetation types smaller than 25 ha are classified in mixed classes, e.g. complex cultivation patterns and land principally occupied with agriculture (BOSSARD et al. 2000). Tab. 1 specifies all vegetation types appearing in the burned scars of our study sites. For two study sites, Andilla and Dos Aguas, rainfall was observed recently before data acquisition took place. The corresponding meteorological data were collected from nearby meteorological stations, provided by the Spanish National Meteorological Agency (AEMET).

## 4 Methods

The authors analyzed the change of SAR backscatter coefficients caused by five forest fires (see section 3) and assessed if pre-fire vegetation types and density influence SAR backscatter behaviour. The obtained results were integrated in an enhanced SAR burned area classification algorithm. An accuracy assessment for the semi-automatically derived classification algorithm was performed. The flow chart of the proposed analysis scheme is shown in Fig. 2.

### 4.1 SAR Backscatter Change Analysis

The pre-processed SAR data (section 3) were intersected with CORINE 2006 land cover data. The burned and unburned parts of the image were defined using the optical derived reference data and subsequently averaged for each land cover type. Afterwards, the backscatter change values were computed by differencing the values of pre- and post-disaster

data. Only vegetation classes of more than five ha were used.

The burned area of La Palma was investigated in more detail by calculating Pearson's correlation coefficients of the mean values of the normalized difference vegetation index (NDVI), the normalized difference shortwave infrared index (NDSWIR) and the SAR backscatter change values. For this purpose, the NDVI and NDSWIR values were grouped in 0.1 intervals. Only intervals containing a significant number of pixels ( $p > 500$ ) were used, resulting in ranges from 0 to 0.8 (NDVI) and -0.1 to 0.6 (NDSWIR). These areas were intersected with the TerraSAR-X pre-disaster and post-disaster images. The NDVI and NDSWIR values were chosen as a proxy for vegetation density. A low index value corresponds to a low vegetation density. Contrarily, a high index value indicates a high vegetation density.

#### 4.2 SAR Classification and Accuracy Assessment

The TerraSAR-X images have been classified by an object-based semi-automatic algorithm

suited for rapid mapping activities for the Mediterranean Basin. The algorithm is based on SAR image change detection techniques (difference, ratio, normalized change index) in conjunction with a fuzzy classification approach and post-classification refinement. The method is described in more detail in BERNHARD et al. (2011). Further, the obtained backscatter characteristics of each vegetation type were considered to enhance the classification algorithm. Thus, the thresholds for burned area detection were computed individually for each CORINE land cover type using the mean difference and the 90% quantile of the change values between pre- and post-disaster images.

To investigate if pre-fire vegetation types influence the classification accuracy, a detailed accuracy assessment was performed. The SAR classification result has been intersected with the reference burned area extent. Only areas which were correctly classified in the SAR as well as in the optical data were considered for the analysis. The SAR classification result was then intersected with CORINE land cover classification and the accuracy assessment was performed individually for each vegetation type.

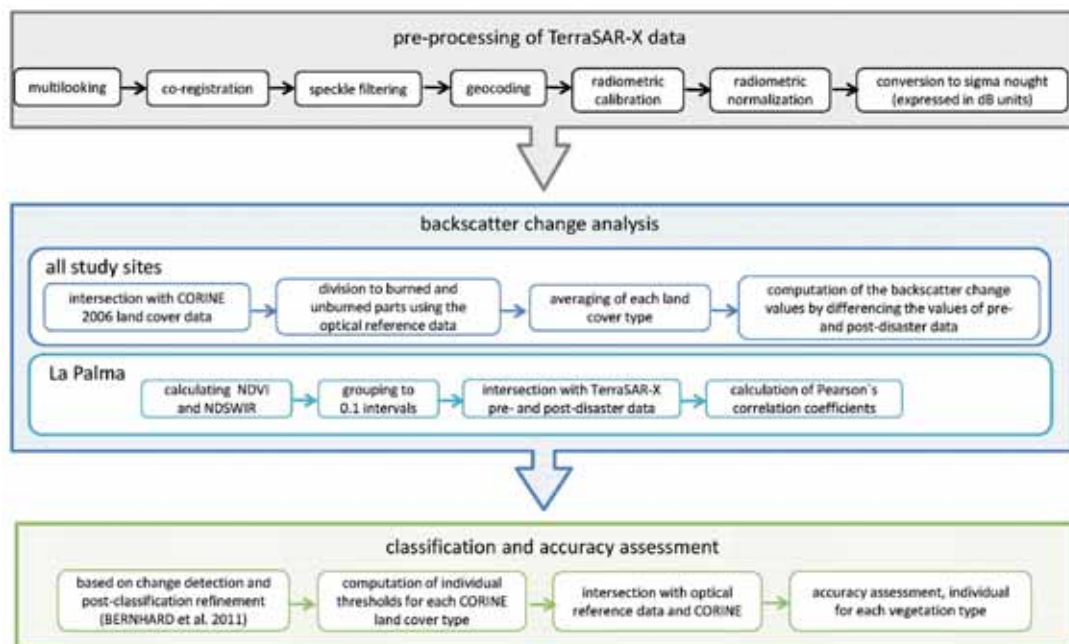


**Fig. 2:** Flow chart of pre-processing, backscatter change analysis, burned area classification and accuracy assessment of the TerraSAR-X data.

## 5 Results and Discussion

### 5.1 SAR Backscatter Change Analysis

The calculated pre- to post-disaster SAR backscatter difference coefficients (BDCs) are presented in Fig. 3. The figure illustrates the mean SAR backscatter change values for each CORINE land cover type, given for fire affected (Fig. 3a) as well as unaffected areas (Fig. 3b). First, the study sites observed under dry environmental conditions (La Palma, Alto Trans-os-Montes and Grammatico) are being discussed. Afterwards, the results of data acquired under wet conditions (pre- versus post-disaster) (see section 3), are being presented.

The study sites with dry acquisition conditions showed highest burned SAR BDCs for coniferous forest, transitional woodland shrub and moors and heathland. This can be attributed to tall and dense vegetation growth previous to burning, a decreased attenuation in the canopy due to the consumption of the needles or leaves by the fire, strong trunk-ground interactions (double-bounce), and an exposal of a rough ground surface. Lowest SAR BDC values in fire affected areas could be obtained for non-irrigated arable land (Grammatico), vineyards (La Palma), complex cultivation patterns (Grammatico) and land principally occupied by agriculture (Grammatico, Alto Trans-os-Montes). No significant change (all values were within the relative radiometric accuracy of TerraSAR-X of 0.7 dB (EINER et al. 2009) of burned SAR BDCs was observed in sclerophyllous vegetation present in La Palma and pastures and vineyards in Grammatico. The low values can be explained by scant vegetation (see also Tab. 1) causing no significant change in backscatter, or low fire severities. The SAR BDCs for unburned areas were rather constant in time, and did not exceed the relative radiometric accuracy of TerraSAR-X (EINER et al. 2009), except for non-irrigated arable land in Alto Trans-os-Montes. A possible explanation could be changes in agricultural management.

Rainfall before post-disaster image acquisition in the study site of Andilla (see Tab. 2) implied an increase in soil and vegetation

moisture. Thus, highest SAR BDCs could be obtained for burned as well as for unburned areas, whereas the increase of SAR BDCs for areas unaffected by fire was lower (around 1.7 dB) than the SAR BDCs for areas affected by fires (up to 7.4 dB). The SAR BDCs in comparison with the results obtained under dry conditions showed an increase of 1.5 dB – 2.3 dB in unburned and 2.2 dB – 6.1 dB in burned areas. These values are confirmed by TANASE et al. (2010c), who observed that the effect of rainfall during summer season increases SAR BDCs from around 1 dB (unburned forest) up to 6 dB (burned area). But, regardless of rainfall, Andilla showed the same trend as the study sites unaffected by rainfall, with highest SAR BDCs associated with tall and dense vegetation structure, whereas vegetation classes with lower SAR BDCs include scant and lower growing vegetation (see Tab. 1).

The second study site affected by rainfall was Dos Aguas. In contrast to Andilla the rainfall occurred prior to the pre-disaster image acquisition and implied higher backscatter coefficients in the pre-disaster image in tall and dense vegetation (up to -8.8 dB versus -13.0 dB in Andilla) than in scant vegetation (up to -11.0 dB versus -11.0 dB in Andilla). This consequently influenced the SAR BDCs. Thus, dense vegetation achieved low SAR BDC values (burned areas up to 1.7 dB and unburned areas up to 1.4 dB), and sparsely growing vegetation obtained high (burned areas up to 3.5 dB and unburned areas up to 1.4) SAR BDC values in comparison to the other study sites.

The scatter plots obtained for La Palma are illustrated in Fig. 4. The results confirmed the previously observed relationship between fire-related backscatter changes and pre-fire vegetation characteristics. SAR BDC values for burned areas versus pre-fire NDVI and NDSWIR values showed a strong positive correlation with  $R_{\text{NDVI}} = 0.94$  and  $R_{\text{NDSWIR}} = 0.98$ , indicating a clear positive relationship between SAR BDCs and vegetation indices. The correlation showed that low pre-fire vegetation density led to low SAR BDCs, and, vice versa, high pre-fire vegetation density implied high SAR BDCs.

### 5.2 SAR Classification Accuracy

The results of the SAR classification in comparison to the combined dataset of the optically derived burned area and CORINE 2006

data are illustrated in Tab. 3. Study sites not affected by precipitation reached highest classification accuracies for coniferous forest (86%, 89%, 91%), and lowest for pastures (5%, 17%). Data acquired under wet conditions (post-dis-

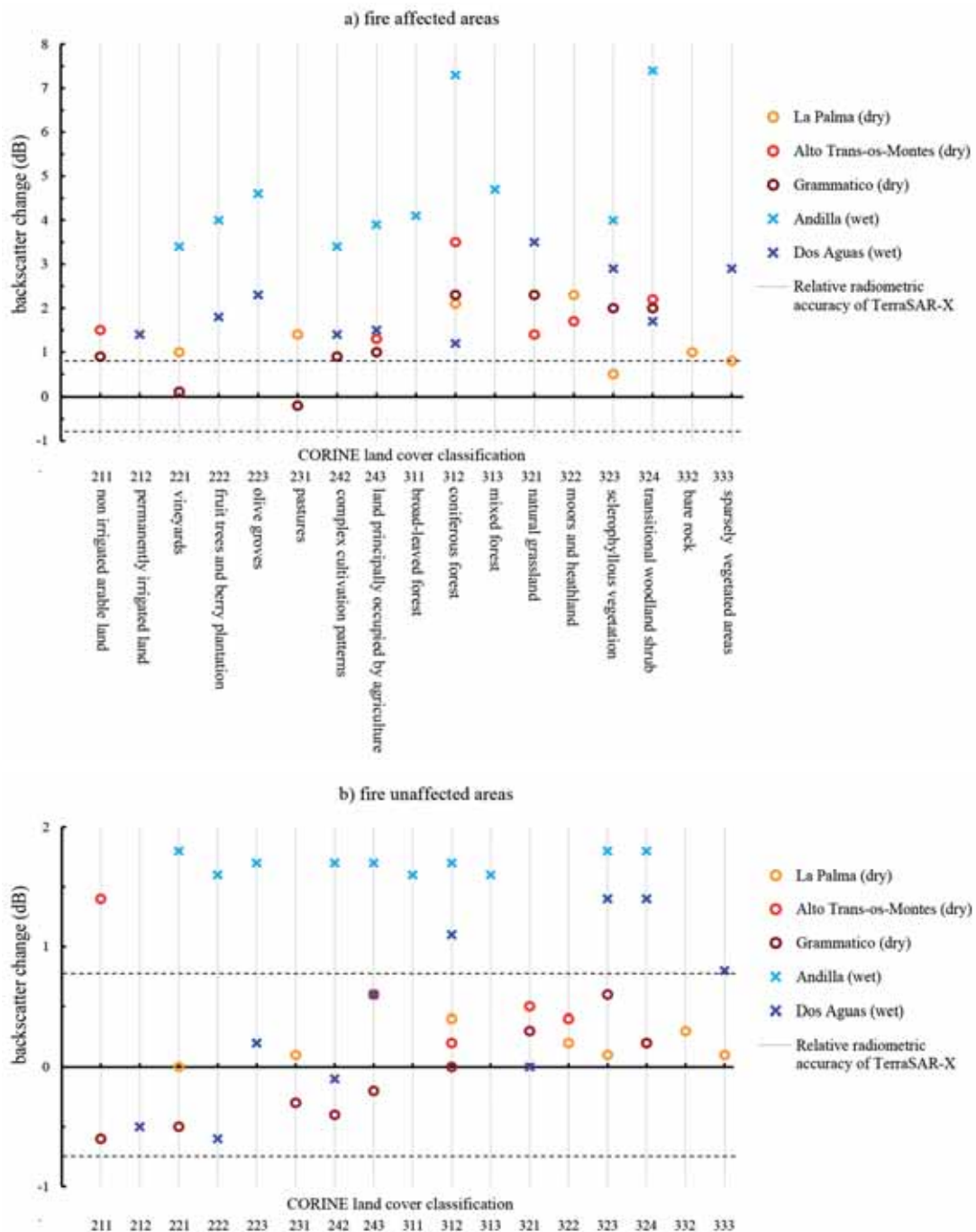


**Fig. 3:** SAR backscatter difference coefficients versus CORINE vegetation classes for a) fire affected and b) fire unaffected areas. Dry study sites are marked by a circle and wet acquisition conditions by a cross.

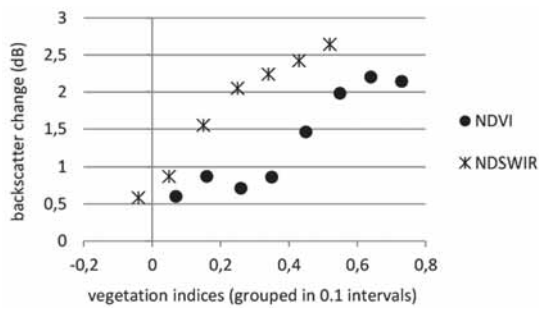


**Fig. 4:** Scatter plot NDVI and NDSWIR versus SAR BDCs in La Palma.

aster) showed highest values for mixed and coniferous forest (81%, 78%), and a lowest value for complex cultivation patterns (39%). The achieved results indicated, that high accuracy values were linked to tall and dense vegetation (see Tab. 1), whereas sparse vegetation exhibited a reduced accuracy, and confirmed the obtained trend of the SAR BDCs analysis. A similar trend was observed by MARI et al. (2012), who used L-band data for dam-

age assessment in Sardinia. Wet conditions in the pre-disaster image led to highest accuracies for natural grassland (86%) and sparsely vegetated areas (86%), where lowest accuracy has been obtained for permanently irrigated arable land (33%). Precipitation prior to pre-disaster image acquisition did not determine lower accuracy values, but an inverse trend could be observed. High accuracies could be obtained in sparsely growing, and comparably low accuracies in dense vegetation.

## 6 Conclusion

In the framework of this study SAR backscatter coefficients and classification accuracy related to pre-fire vegetation type and density have been analyzed. The study was assessed for five study sites located at La Palma, Alto Trans-os-Montes, Dos Aguas, Andilla and Grammatico, and considered dry as well as wet environmental conditions.

**Tab. 3:** Classification result of the SAR burned area algorithm in %.

CLC-code	Vegetation class	La Palma	Alto Trans-os-Montes	Dos Aguas	Andilla	Grammatico
211	non-irrigated arable land		27			69
212	permanently irrigated land			33		
221	vineyards	50			42	76
222	fruit trees and berry plantation			44	56	
223	olive groves			48	69	
231	pastures	5				17
242	complex cultivation patterns			39	39	44
243	land principally occupied by agriculture		28	54	55	75
311	broad-leaved forest				58	
312	coniferous forest	89	86	55	78	91
313	mixed forest				81	
321	natural grassland		42	86		79
322	moors and heathland	32	51			
323	sclerophyllous vegetation	12		83	65	69
324	transitional woodland shrub		74	72	66	77
332	bare rock	29				
333	sparsely vegetated areas	40		86		

SAR backscatter difference coefficients (BDCs) were analyzed for correlations to CORINE 2006 land cover data. The results pointed out that highest SAR BDCs were linked to tall and dense pre-fire vegetation, whereas scant vegetation was marked by lowest differences. This trend was observed in dry as well as in wet environmental conditions when rainfall occurred before the post-disaster image acquisition. Precipitation prior to pre-disaster image acquisitions led to an inverse trend.

A regression analysis of the SAR BDCs, the NDVI and the NDSWIR values for La Palma showed positive correlations. The vegetation indices were used as a proxy for vegetation density, and the correlation coefficients approved the previous obtained relationship between pre-fire vegetation structure and SAR BDCs of dry and wet (post-disaster) environmental conditions.

A classification and accuracy assessment of the proposed algorithm was performed using the optical derived burned area extent as a reference. Since the thresholds for burned area classification were computed individually for each vegetation type, individual class accuracies of up to 91% could be obtained. Nevertheless, classification accuracies (5% – 91%) varied strongly according to the individual (low versus dense) vegetation type.

The lack of ground truth data led to an estimation of vegetation density by vegetation indices. Ground truth data would be necessary to investigate the obtained relationship between pre-fire vegetation density, soil moisture, fire severity and SAR BDCs in more detail. Moreover, it is of interest whether tree crowns stay possibly unaffected by fire. This would lead to an unchanged backscatter behaviour for X-band data, although the ground vegetation might be completely burned. A comparison to other microwave bands (such as L-band) could help to understand SAR backscatter behaviour after forest fires in more detail, and show the potential strengths and weaknesses of each method applied. The results presented are valid for most vegetation types occurring in the European Mediterranean. In significantly different environments, such as tropical or boreal forests, other trends might be observed.

Our analysis confirmed the applicability of X-band SAR data for burned area mapping

in the European Mediterranean. According to this finding, fire management might profit from a more extensive or complementary use of SAR data for burned area detection, especially under challenging weather conditions.

## References

- AMRAOUI, M., DACAMARA, C. & PEREIRA, J., 2010: Detection and monitoring of African vegetation fires using MSG-SEVIRI imagery. – *Remote Sensing of Environment* **114** (5): 1038–1052.
- BERNHARD, E., TWELE, A. & GÄHLER, M., 2011: Rapid Mapping of Forest Fires in the European Mediterranean Region – a Change Detection Approach Using X-Band SAR Data. – *Photogrammetrie, Fernerkundung, Geoinformation* **2011** (4): 261–270.
- BOSSARD, M., FERANEC, J. & OTAHEL, J., 2000: Corine land cover technical guide. – Addendum 2000, European Environment Agency, technical report No. 4.
- BOURGEAU-CHAVEZ, L., HARRELL, P., KASISCHKE, E. & FRENCH, N., 1997: The detection and mapping of Alaskan wildfires using a spaceborne imaging radar system. – *International Journal of Remote Sensing* **18**: 355–373.
- BOURGEAU-CHAVEZ, L., KASISCHKE, E., BRUNZELL, S., MUDD, J. & TUKMAN, M., 2002: Mapping fire scars in global boreal forests using imaging radar data. – *International Journal of Remote Sensing* **23** (20): 4211–4234.
- BÜTTNER, G. & KOSZTRA, B., 2007: CLC2006 Technical Guidelines. – European Topic Centre, European Environment Agency, Spain.
- EINER, M., FRITZ, T., MITTERMAYER, J., ROTH, A., BÖRNER, E. & BREIT, H., 2009: TerraSAR-X Ground Segment Basic Product Specification Document. – Cluster applied remote sensing, German Aerospace Center (DLR), Wessling.
- FRENCH, N., KASISCHKE, E., BOURGEAU-CHAVEZ, L. & HARRELL, P., 1996: Sensitivity of ERS-1 SAR to variations in soil water in fire-disturbed boreal forest ecosystems. – *International Journal of Remote Sensing* **17**: 3037–3053.
- GIMENO, M., SAN-MIGUEL AYANZ, M. & LIBERTA, G., 2003: Fire scar detection in central Portugal using RADARSAT-1 and ERS-2 SAR data. – *IEEE International Geoscience and Remote Sensing Symposium I-VII*: 2491–2493.
- GIMENO, M. & AYANZ, J., 2004a: Evaluation of Radarsat-1 data for identification of burnt areas in southern Europe. – *Remote Sensing of Environment* **104**: 346–359.

- GIMENO, M., SAN-MIGUEL-AYANZ, J. & SCHMUCK, G., 2004b: Identification of burnt areas in Mediterranean forest environments from ERS-2 SAR time series. – *International Journal of Remote Sensing* **25** (22): 4873–4888.
- HOEKMANN, D., 1987: Measurements of the Backscatter and Attenuation Properties of Forest Stands at X-, C- and L-Band. – *Remote Sensing of Environment* **23**: 397–416.
- JUSTICE, C.C. & KORONZTI, S., 2001: A review of the status of satellite fire monitoring and the requirements for global environmental change research. – AHERN, F. (ed.): *Global and regional vegetation fire monitoring from space: planning a coordinated international effort*: 1–19.
- JUSTICE, C., GIGLIO, L., KORONZTI, S., OWENS, J., MORISSETTE, J., ROY, D., DESDOITRES, J., ALLEAUME, S., PETITCOLIN, F. & KAUFMAN, Y., 2002: The MODIS fire products. – *Remote Sensing of Environment* **83** (1–2): 244–262.
- KARSZENBAUM, H., TIFFENBERG, J., GRINGS, F., MARINEZ, J., KANDUS, P. & PRATOLONGO, P., 2003: A SAR time series analysis toolbox for extracting fire affected areas in wetlands. – *IEEE Geoscience and Remote Sensing Symposium, IGARSS '03* **6**: 4107–4109.
- KASISCHKE, E., BOURGEOU-CHAVEZ, L., FRENCH, N., HARRELL, P. & CHRISTENSEN, N., 1992: Initial observations on using SAR to monitor wildfire scars in boreal forests. – *International Journal of Remote Sensing* **13** (18): 3495–3501.
- LEONE, V., 2009: Human factors of fire occurrence in the Mediterranean. – CHUVIECO, E. (ed.): *Earth observation of wildland fires in Mediterranean ecosystems*, Springer: 149–179.
- MARGARIS, N., KOUTSIDOU, E. & GIOURGA, C., 1996: Changes in traditional Mediterranean land-use systems. – BRANDT, C. & THORNES, J. (eds.): *Mediterranean desertification and land use*, 1996.
- MARI, N., LANEVE, G., CADAU, E. & PORCASI, X., 2012: Fire Damage Assessment in Sardinia: the use of ALOS/PALSAR data for post fire effects management. – *European Journal of Remote Sensing* **45**: 233–241.
- MENGES, C., BARTOLO, R., BELL, D. & HILL, G., 2004: The effect of savanna fires on SAR backscatter in northern Australia. – *International Journal of Remote Sensing* **25** (22): 3857–4871.
- PULLIAINEN, J., HEISKA, K., HYYPPÄ, J. & HALLIKAINEN, M., 1993: Backscattering Properties of Boreal Forests at the C- and X-Bands. – *IEEE Geoscience and Remote Sensing Symposium* **2**: 388–390.
- SARSCAPE, 2012: SARscape® 4.4, system for optical and SAR image analysis, Cascine di Barico, Purasca, Switzerland.
- SIEGERT, F. & RÜCKER, G., 2000: Use of multitemporal ERS-2 SAR images for identification of burned scars in south-east Asian tropical rainforest. – *International Journal of Remote Sensing* **21** (4): 831–837.
- TANASE, M., PÉREZ-CABELLO, F., RIVA, J. & SANTORO, M., 2010a: TerraSAR-X data for burn severity evaluation in Mediterranean forests on sloped terrain. – *IEEE Transactions on Geoscience and Remote Sensing* **48** (2): 917–929.
- TANASE, M., SANTORO, M., WEGMÜLLER, U., DE LA RIVA, J. & PÉREZ-CABELLO, F., 2010b: Properties of X-, C- and L-band repeat-pass interferometric SAR coherence in Mediterranean pine forests affected by fires. – *Remote Sensing of Environment* **114**: 2182–2194.
- TANASE, M., SANTORO, M., DE LA RIVA, J., PÉREZ-CABELLO, F. & TOAN, T., 2010c: Sensitivity of X-, C-, and L-Band SAR Backscatter to Burn Severity in Mediterranean Pine Forests. – *IEEE Transaction geoscience and remote sensing* **48** (10): 3663–3675.
- TERRASAR-X, 2012: TX-GS-PL-4001. – <https://www.terrasar-x.dlr.de/pdfs/TX-GS-DD-3302.pdf> (11.12.2012).
- VIEGAS, D., RIBEIRO, L., VIEGAS, M., PITA, L. & ROSSA, C., 2009: Impacts on fire on society: extreme fire propagation issues. – CHUVIECO, E. (ed.): *Earth observation of wildland fires in Mediterranean ecosystems*, Springer: 97–109.
- WASTL, C., SCHUNK, C., LEUCHNER, M., PEZZATTI, G. & MENZEL, A., 2012: Recent climate change: long-term trends in meteorological forest fire danger in the Alps. – *Agricultural and forest meteorology* **162–163**: 1–13.

## Address of the Authors:

EVA-MARIA BERNHARD, ANDRÉ TWELE & SANDRO MARTINIS, German Aerospace Center (DLR), German Remote Sensing Data Center (DFD), D-82234 Oberpfaffenhofen, Tel.: +49-(0)8153-28-2481, -3510, -3034, Fax: +49-(0)8153-28-1445, e-mail: {eva-maria.bernhard}{andre.twele}{sandro.martinis}@dlr.de

Manuskript eingereicht: Februar 2014

Angenommen: April 2014





# Evaluation of a Light-weight Lidar and a Photogrammetric System for Unmanned Airborne Mapping Applications

GIANPAOLO CONTE, PIOTR RUDOL & PATRICK DOHERTY, Linköping, Sweden

**Keywords:** UAS, lidar, sensor fusion, photogrammetry

**Summary:** This paper presents a comparison of two light-weight and low-cost airborne mapping systems. One is based on a lidar technology and the other on a video camera. The airborne lidar system consists of a high-precision global navigation satellite system (GNSS) receiver, a microelectromechanical system (MEMS) inertial measurement unit, a magnetic compass and a low-cost lidar scanner. The vision system is based on a consumer grade video camera. A commercial photogrammetric software package is used to process the acquired images and generate a digital surface model. The two systems are described and compared in terms of hardware requirements and data processing. The systems are also tested and compared with respect to their application on board of an unmanned aerial vehicle (UAV). An evaluation of the accuracy of the two systems is presented. Additionally, the multi-echo capability of the lidar sensor is evaluated in a test site covered with dense vegetation. The lidar and the camera systems were mounted and tested on-board an industrial unmanned helicopter with maximum take-off weight of around 100 kilograms. The presented results are based on real flight-test data.

**Zusammenfassung:** *Bewertung eines Lidar-systems mit geringem Gewicht und eines photogrammetrischen Systems für Anwendungen auf einer UAV.* Dieser Beitrag präsentiert einen Vergleich von zwei leichten und kostengünstigen luftgestützten Kartiersystemen. Eines der Systeme basiert auf Laserscanner-Technologie, während das andere eine Videokamera benutzt. Das luftgestützte Laserscannersystem besteht aus einem hochgenauen Empfänger für globale Navigationssatellitensysteme (GNSS), einer inertialen Messeinheit (IMU) auf Basis eines mikro-elektromechanischen Systems (MEMS), einem magnetischen Kompass und einem kostengünstigen Laserscanner. Das optische System basiert auf einer handelsüblichen Videokamera. Ein kommerzielles photogrammetrisches Softwarepaket wird verwendet, um die damit aufgenommenen Bilder zu prozessieren und digitale Oberflächenmodelle abzuleiten. Die beiden Systeme werden beschrieben und in Hinblick auf ihre Anforderungen an Hardware und Datenprozessierung verglichen. Außerdem werden sie in Hinblick auf ihre Eigenschaften bei der Verwendung auf unbemannten Flugkörpern (UAV) getestet und verglichen. Die Genauigkeit beider Systeme wird evaluiert. Zusätzlich wird die Fähigkeit des Laserscanner-Sensors in Hinblick auf Mehrfachechos in einem Testgebiet mit dichter Vegetation untersucht. Beide Systeme wurden auf einem unbemannten Industrie-Helikopter mit einem maximalen Startgewicht von ca. 100 kg montiert. Alle hier präsentierten Daten beruhen auf tatsächlich im Zuge von Testflügen aufgenommenen Daten.

## 1 Introduction

The work presented in this article focuses on the evaluation of two different traditional technologies for building digital surface

models: airborne lidar and photogrammetry. The investigation is done in the context of the newly emerging technology of light-weight unmanned aerial systems (UAS). UAS's offer many advantages over manned aircraft

mainly due to the reduced operational costs. Additionally, UAS's can operate in hazardous environments or during natural catastrophes without endangering the lives of human pilots.

Applying traditional technologies used on full-size manned aircraft to small UAS platforms (below 100 kg take-off weight) is not straightforward as the weight and costs become of main concern. The use of low-cost sensors degrades the system performance but often the cost/benefit balance is still convenient.

Airborne lidar scanner (ALS) systems have been an active research area in recent years. Since their introduction in the mid-90s the technology has developed substantially in terms of increased accuracy, increased pulse repetition rate, introduction of multiple returns (including full waveform digitizing) and integration with a higher accuracy GNSS and inertial navigation systems.

This paper presents a low-cost and light-weight ALS system for close range airborne applications. Additionally, an investigation of the multi-echo capability of the ALS in the context of vegetation measurement is provided. The ALS system is compared to a light-weight vision-based mapping system installed on the same platform.

The paper has the character of a comparative study of the two different mapping modalities. Both systems are light-weight and low-cost and are suitable for installation on a small UAV platform. The main goal of the paper is to compare the systems with regard to the weight, costs, processing requirements and deployment effort.

Due to their different nature, the two systems could be used in a complementary manner in order to compensate their respective

weaknesses. For instance, the vision-based system does not work well in featureless environments while the lidar system does not require such features to work properly. On the other hand, lidar systems are difficult to calibrate while vision-based systems are relatively easy in this respect. A combination of a lidar and a vision system could help in the lidar calibration process. In this article the two systems operate independently and a fusion of the two methods will be addressed in a future work.

The ALS and vision-based systems described have been integrated and tested on a Yamaha RMAX helicopter (Fig. 1).

## 2 Related Work

Using lidar systems on unmanned rotorcraft opens a wide range of applications, but at the same time this poses a number of challenges which have to be addressed. The complications become more severe for medium and small size platforms using low cost sensors. One complication involves the high vibration levels occurring during flight. Additionally, the fidelity of sensors, which are required to be of low weight, is often sacrificed. These problems open a number of research issues which have been addressed in recent years.

A mobile laser scanning system for post-mission map generation from raw data recorded by a suite of sensors consisting of a GNSS receiver, an inertial measurement unit (IMU), and a laser scanner, was presented by GLENIE et al. (2013). The system is comparable to our approach, however, it is mainly tailored to be operated from a backpack or a balloon where it achieves a vertical accuracy of up to 3 cm and a horizontal accuracy of 17 cm. A laser mapping system for small helicopters has been developed by LIN et al. (2011). The authors demonstrated the feasibility of their approach by processing data collected during a manual flight.

Mapping using image based solutions have also received a considerable amount of attention in recent years. A set of applications using UAVs equipped with cameras for these purposes are presented in REMONDINO et al. (2011).



Fig. 1: The UAS Tech Lab RMAX helicopter.

A system composed of a video camera, a laser range finder, GPS and IMU sensors was presented by NAGAI et al. (2009). The system includes a new method for direct georeferencing by the combination of bundle block adjustment and Kalman filtering. It allows for objects to be rendered richly in shape and with detailed textures automatically using a UAV flying at a low altitude. The average error of the digital surface model is reported to be approximately 10 cm to 30 cm. In contrast with our work, where low-cost MEMS inertial sensors are used, they use fiber-optic gyroscopes which are several orders of magnitude more accurate and expensive.

As previously stated, lidar systems used on helicopters experience a high level of vibrations during flight. Consequently, range measurements depending on pose estimations are typically erroneous and conventional methods for point cloud registration might fail in certain cases. KAESTNER et al. (2006) proposed a probabilistic approach for alignment and change detection using range sensor data and a non-rigid point cloud registration that implicitly deals with high estimation errors. The system was evaluated on a helicopter platform.

A comparison between digital elevation models of a cultural heritage site generated using a camera equipped rotorcraft UAV and a terrestrial laser scanner can be found in EISENBEISS & ZHANG (2006). The results presented show the difference mean value to be less than 1 cm with a standard deviation of 6 cm.

Lidar systems have also been extensively used for forestry applications in order to estimate key forest structure characteristics such as canopy height, topography, average stem diameter, canopy volume etc. Examples of such systems can be found in PIROTTI (2011) and WALLACE et al. (2012). In particular the former investigates the use of full waveform lidar (FWL) technology. In contrast to traditional discrete return lidar, FWL samples the entire back-scattered signal intensity at high rate allowing for an in-depth study of vegetation parameters. However, this technology is still quite complex and expensive and at the moment not suitable for experimentation on small UAV platforms.

The rich body of literature in this field shows the existence of similar lidar-based and

vision-based systems as the one presented in this paper. However, proper evaluations and comparisons of these techniques when used in the same context, i.e. the same flying platform, same environmental conditions, the same flight plan, are not common. This is especially true in the new domain of small size and low-weight unmanned aircraft where the sensor technology used is several orders of magnitude less expensive. This article is intended to be a contribution in this context.

### 3 Helicopter Platform

In this paper, the platform used for experimentation is the UAS Tech Lab (UASTL) RMAX. It is a modified Yamaha RMAX helicopter (Fig. 1). It uses a 21 hp two-strokes gas engine with an empty weight of 61 kg and a maximum take-off weight of 95 kg. The main rotor diameter is 3.1 m. The UASTL RMAX is capable of autonomous flight from take-off to landing. The hardware and software enabling the autonomous flight capabilities were developed at the Division of Artificial Intelligence and Integrated Computer System (AIICS) at Linköping University (DOHERTY et al. 2004, CONTE 2009).

### 4 Airborne Lidar System Description

The following subsections describe the hardware components and algorithms used in the proposed airborne lidar system.



**Fig. 2:** The airborne lidar and camera systems mounted on the UASTL RMAX helicopter.

#### 4.1 Hardware

The ALS described in this paper is depicted in Fig. 2. The system consists of a class 1 SICK LMS511 PRO lidar with multi-echoes capability. The laser wave length is 905 nm and the maximum scanning angle is 190° with a maximum angular resolution of 0.166°. The beam divergence is 11 mrad which gives a spot size of about 50 cm at a distance of 45 m, i.e. a typical flight altitude of the experiments performed here. Other characteristics of the scanner are reported in Tab 1.

The GNSS positioning system used is the Javad TRE-G3T. It is capable of tracking GPS (L1/L2/L2C/L5), GLONASS (L1/L2) and Galileo (E1/E5A) satellite systems. The ground reference correction signal is transmitted to the on-board receiver using the Telit TinyOne Plus 868 MHz wireless datalink. An Analog Devices ADIS16375 MEMS inertial measurement unit (IMU) and a Honeywell HMR3000 magnetic compass are additional parts of the system (see Tab.1 for technical specifications). An embedded PC104 1.6 GHz Intel Atom computer is used for on-board data acquisition. The schematic of the system is presented in Fig. 3. The picture also includes the camera system for photogrammetric reconstruction described in section 5.

The lidar and the IMU sensors are mounted on a vibration isolated rig in front of the UASTL RMAX platform (see Fig.2). The data acquisition PC and the GNSS receiver are mounted on a vibration isolated plate on a side of the helicopter. The magnetic compass

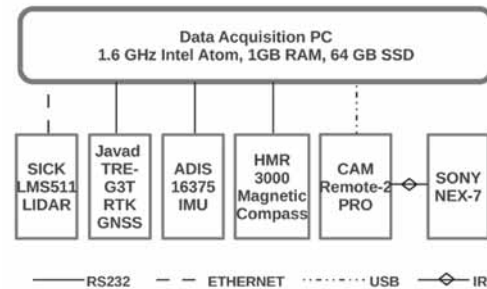


**Fig. 3:** Schematics of the ALS and photogrammetric hardware components (SSD = solid state drive, SICK = manufacturer of sensors, LMS = laser measurement sensor, TRE-G3T = GNSS-board, ADIS = Analog Devices (company), HMR = Honeywell digital compass, Sony NEX-7 = camera).

is placed on the helicopter tail boom to minimize magnetic interferences influencing the measurements.

Compared to high-end ALSs traditionally used in the remote sensing field, the system presented here has a much lower cost, approximately 15,000 Euro versus 200,000 Euro for high-end systems. Additionally, it is lighter but has lower range and accuracy. The accuracy problem must be placed in the context of the intended usage of the system. The target use for the proposed ALS is for small and medium sized UASs flying at low altitudes of 50 m – 100 m above ground level (AGL). Typically, high-end ALS's installed on manned aircraft operate at altitudes of 500 m AGL or more. Considering that direct georeferencing errors increase with the AGL altitude it can be

**Tab. 1:** Airborne lidar system sensor specification.

SICK Laser LMS511 PRO				
Data Rate	Range	Range err.	Weight	Cost
28.6 kHz	80 m	1.8 cm 1 $\sigma$	3.7 kg	6000 €
Javad GNSS TRE-G3T, AirAnt antenna				
Data Rate	Pos. Err.	RTK	Weight	Cost
20 Hz	5 cm	yes	77 g 320 g (antenna)	6500 €
MEMS IMU ADIS16375				
Data Rate	Gyro bias	Acc. bias	Weight	Cost
100 Hz	12°/hr	0.13 mg	25 g	450 €
Compass HMR3000				
Data Rate	Accuracy	Resolution	Weight	Cost
15 Hz	<1.5°	0.1°	92 g	600 €
On-board Data Acquisition PC104				
Processor	Memory	Mass storage	Weight	Cost
Atom 1.6 GHz	2 GB SDRAM	SSD 100 Gb	400 g	900 €
<b>Tot.</b>			4.6 kg	14450 €

reasonable to assume that, from an accuracy point of view, low cost ALS flying at low altitudes can be compared to high-end ALS flying at higher altitudes. Insights on direct georeferencing methods can be found in SKALLOUD (1999).

#### 4.2 Lidar System Calibration

Calibration of sensors is essential to reduce the systematic errors in the system. In case of ALS, a calibration procedure aims at computing the boresight parameters, i.e. the mounting angle between an IMU and a lidar scanner, the lever arms between a lidar, an IMU and a GNSS antenna and biases in the lidar scanner device (ranges and mirror angle).

ALS calibration has been an active area of research and it is still the case that a standard procedure has not yet been defined. An analytical and automatic procedure which estimates all the calibration parameters is difficult to apply because of the correlation between the parameters. Another problem lies in the difficulty of extracting features out of a lidar point cloud. BANG (2010) includes a review of several different approaches developed for ALS calibration. Professional ALSs are still calibrated through empirical ad-hoc procedures requiring well defined features such as planar patches or edges.

An empirical lab calibration was performed for this work. Lever arms between the IMU, the lidar and the GNSS antenna were directly measured on the platform and the correction added in the software. Boresight estimation between IMU and lidar was performed by acquiring IMU and lidar data (the IMU is rigidly mounted on the lidar) while manually pitching and rolling the scanner unit. A point cloud was generated from the acquired data and a visual assessment of the distortion of known features, e.g. walls, floor and ceiling, indicates whether a boresight correction was needed. The boresight parameters were empirically adjusted until such distortion was judged acceptable. However, no numerical criteria was applied but engineering judgment after visual inspection of the point cloud.

#### 4.3 Data Acquisition

The raw data produced by the sensors described in the previous section is saved by the data acquisition PC on a solid state drive (SSD) during a flight. The software developed for the purpose of this work collects data using the appropriate interfaces (see Fig. 3) and saves it in text files. The time-stamping of data is done at the time of receiving them by the acquisition PC which reads the sensors at a high-rate. Hardware triggering of sensors is not used and the time of acquisition and transfer has proven to be negligible for the intended application. However, in order to improve the data synchronization a method for hardware triggering can be used as described by WEHR & LOHR (1999). Even though a non-realtime Linux OS is used, no negative consequences of it have been observed during the system evaluation and operation.

#### 4.4 Processing

The data processing workflow includes: (a) synchronized data collection during a flight; (b) post-processing of the IMU, RTK GNSS and compass data using an efficient two-pass smoothing algorithm; (c) direct georeferencing of lidar measurements and point cloud generation.

Smoothing techniques are used to reconstruct an optimal state solution using past, current and future measurements. The algorithm used here is the Rauch-Tung-Striebel smoother (RTSS) as presented in RAUCH et al. (1965). It belongs to the fixed-interval smoother class. The whole dataset was used to compute the smoothed trajectory.

The smoothing algorithm is implemented in forward and backward processing parts. The forward part is a 15-state extended Kalman filter (EKF). The state vector includes positions, velocities, attitudes, accelerometers and gyroscope biases. The EKF is implemented in a loosely coupled scheme using the error dynamic formulation where the navigation errors of the inertial navigation system (INS) are estimated and used to correct the navigation solution (SHIN 2005). The measurement update step is realized using the so-called UD

algorithm (BIERMAN 1977) and is executed at 20 Hz rate (GNSS update rate). The filter time update is performed at the rate of 100 Hz, which is the same as the IMU data rate.

The backward part is implemented with the RTSS recursive algorithm described in BROWN & HWANG (1992), p. 334. The advantage of the RTSS algorithm is that its implementation is of low complexity compared to other smoothing algorithms. On the other hand, it requires a certain amount of memory storage since some of the parameters must be retained during the forward pass at each time step.

## 5 Vision-based System Description

This section describes the photogrammetric hardware and software components used in this paper.

### 5.1 Hardware

The camera used in the photogrammetric system is a Sony Nex-7 and it is mounted, pointing downward, on the same vibration isolated rig used for the lidar in front of the UASTL RMAX platform (see Fig. 2). The imaging sensor size is  $23.5 \times 15.6 \text{ mm}^2$  (APS-C size), with a total of 24 megapixels and is based on the CMOS technology. The camera features a mirror-less construction and allows for changing lenses. It has been equipped with a fixed focal length lens as it guarantees better optical parameter stability during flight. The lens chosen has a 16 mm focal length (or 24 mm if using the 35 mm equivalent terminology) with the angle of view of  $83^\circ$ . The total weight of the camera is 423 grams. The communication between the camera and the data acquisition PC is realized using the CAMremote-2 PRO (<http://vp-systems.eu/camremote.html>) infrared interface. The interface is used only for triggering the image acquisition. The physical connection is shown schematically in Fig. 3.

### 5.2 Camera System Calibration

The image processing software described in more detail in section 5.4 estimates the cam-

era internal parameters during the processing of the images. Therefore, there is no need for an explicit calibration procedure. This is a great advantage compared to the complex calibration procedure required for the ALS. The software estimates the lens focal length, the principal point, radial and tangential lens distortion parameters. It is important that these parameters remain stable during flight. This is usually not the case for cheap consumer cameras. In this application, a fixed focal length lens is used in order to maintain a sufficient optical stability.

### 5.3 Data Acquisition

Particular care must be taken in the flight planning phase to ensure that the pictures collected have sufficiently large overlapping regions. More information about flight plans is provided in section 6. The time of triggering of the image capture is logged and used for synchronization with the GNSS data. Images are saved on the camera's memory card and downloaded after a flight for processing.

### 5.4 Processing

As already mentioned, the processing is done using *Pix4UAV Desktop 3D 2.1* (PIX4D 2013) software from Pix4D company. It uses a structure-from-motion approach and implements the complete workflow in an automated way. The workflow can be divided into 3 main steps. The first step consists of keypoint extraction using SIFT (LOWE 2004), keypoint matching, camera calibration and pose optimization using bundle block adjustment and finally point cloud geolocation using GNSS geotags or ground control points. In the second step, a point cloud densification and filtering is performed. The last step includes a DSM (digital surface model) generation, image ortho-rectification and orthomosaic blending. At the end of the first step the software produces a report containing information about the quality of the acquired images. Based on the reported results the user can decide to continue with the processing or to repeat the image acquisition.

The software allows use of either ground control points or geo-tagged images. The second option was used in this work as the GNSS position is already available and used for the lidar system. Image geo-tagging information is added in the exchangeable image file (EXIF) metadata. Images are geo-tagged using latitude, longitude and altitude information taken from the on-board GNSS.

Pix4D is similar to many other software packages like PhotoScan, MicMac, Bundler, etc. A description of alternative software solutions can be found in NEITZEL & KLONOWSKI (2011). In this article the authors do not make any comparative statements between Pix4D and other solutions because of lack of experience in using other photogrammetric software. Pix4D software was chosen as a representative example of an image-based DSM solution for comparison with the proposed ALS system.

## 6 Experimental Results

This section presents surface reconstruction results for two different landscapes: a small airfield with a few building structures and a tree covered area. The reconstruction of the airfield is performed using the ALS and photogrammetric system presented in previous sections. Photogrammetric reconstruction of the tree-covered field is not reported here as this technique presents additional complications in this kind of environment.

### 6.1 Airfield Mapping

The object of this study is an airfield located near Motala (Sweden). An overview of the area is depicted in Fig. 4. The size of the mapped area is about 1.6 ha. The flight was performed using a rectangular scanning pattern consisting of 3 flight lines as shown in Fig. 4. The flight parameters (velocity, altitude, distance between scanning lines) were chosen in order to satisfy the requirements of both the ALS and the vision-based systems. Lidar and camera images were acquired simultaneously.

The first parameter chosen was the flight altitude above the ground (about 45 m). The value was chosen in order to operate far enough from the lidar range limit (about 80 m). Given the flight altitude, the other parameters were chosen in order to satisfy the constraints imposed by the vision system. In order to reach a satisfactory accuracy, the Pix4D software requires a number of keypoint matches greater than 1000 per image pair. This is usually achieved when the image front overlap is greater than 75% and the image side overlap is greater than 40% on an easy terrain, i.e. rich in features such as urban terrain, for instance. In order to satisfy such requirements the flight speed was set at 3 m/s with a distance of 40 m between consecutive flight lines. A wide angle camera lens was also used (16 mm as described in section 5.1). Additionally, the image acquisition rate was set at 1 image every 2 seconds. The camera image size was set to  $3008 \times 2000$  pixels resulting in a ground sampling distance (GSD) of about 2.5 cm/pixel. The lidar scanning rate was set at the maximum speed of 100 Hz with a scanning angular resolution of  $0.66^\circ$  resulting in a point density of 50 points/m<sup>2</sup>. This is a much larger number compared to the typical point density obtained from an ALS used on manned airborne plat-

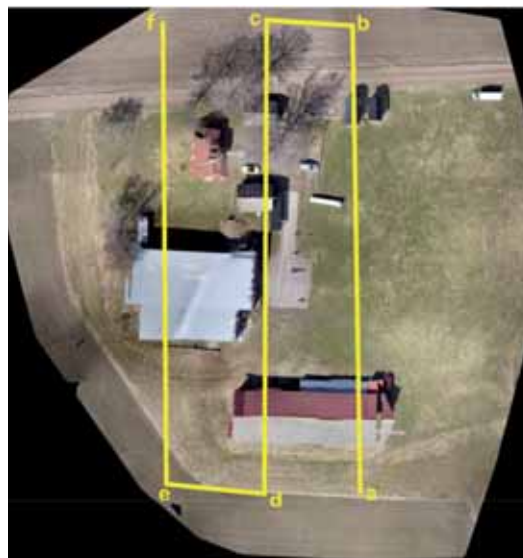


**Fig. 4:** Orthomosaic of the airfield near Motala (Sweden). The yellow lines show the scanning pattern used to cover the area starting from point a to f.

forms (below 10 pts/m<sup>2</sup>). The scanning angle was set at 50°.

Fig. 5 (a) shows a snapshot of the airfield surface model generated with the ALS. The photogrammetric model displayed in Fig. 5 (b) was generated from 76 images.

From a visual inspection of Fig. 5 (a) and (b) it can be observed that neither the ALS nor the photogrammetric models are complete. Some parts of the buildings are missing in both models. It can be observed also that the photogrammetric model is slightly more noisy than the ALS one. In addition, on the right side of the photogrammetric model there is a certain amount of erroneous elevation (which is not present in reality) and the trees are not modeled properly. The reason could be an insufficient image overlap since some parts of the area have a poor feature content.

In order to give an indication about the accuracy of the different point clouds generated, it was decided to accurately model the long hangar building (at the bottom of Fig. 4). The resulting model has been used as the best available reference. The following procedure was used in order to build the reference model.



(a) Surface model generated from the lidar system.



(b) Surface model generated from the photogrammetric software.

**Fig. 5:** Digital surface model of the airfield. The green colour represents the ground surface. An elevation value greater than 20 cm (the elevation is intended from the ground surface which is substantially flat) is represented in red colour. The red becomes lighter with an increase in elevation.

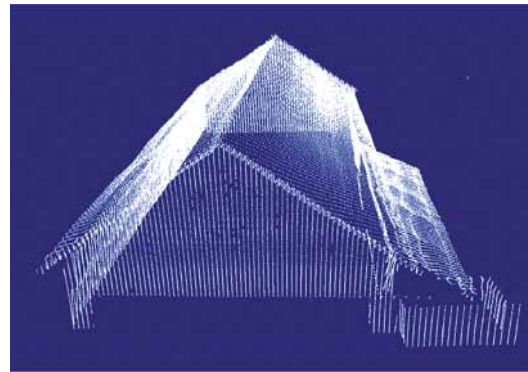


**Fig. 6:** Hangar reference model generated from lidar measurements taken from the ground.

The four building façades were reconstructed from lidar measurements taken from 4 different positions on the ground and at a distance of around 30 m from each façade. Each façade was scanned by changing the lidar elevation angle while keeping the position static. The resulting point cloud of the hangar was accurately geolocated by measuring the four hangar corners with the same RTK GNSS system used on the helicopter. A 30 s static measurement acquisition for each corner was performed and the mean value was taken for each corner. The lidar scanner used for the model construction was the same as that installed on the helicopter. Given the accuracy of the sensors used (see Tab. 1) we believe that the accuracy of the resulting reference model is of the order of 5 cm. The model is shown in Fig. 6.

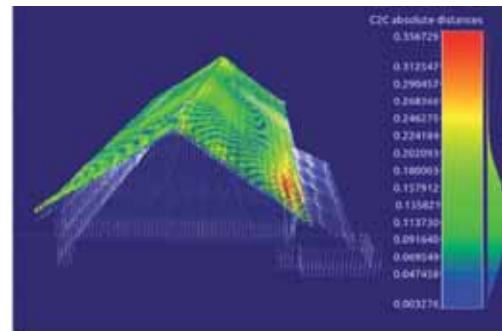
The hangar roof was captured from each of the 3 lidar strips generated from the scanning segments *a-b*, *c-d*, *e-f* (Fig. 4). Each of the roof reconstructions were compared to the reference model while only one photogrammetric hangar roof reconstruction was available for comparison. The error statistic of the different point clouds have been computed using CloudCompare software (CLOUDCOMPARE 2013) and are reported in Tab. 2. The CloudCompare *cloud-to-cloud* distance command has been used. The mean error generated by the lidar system has a strong fluctuation depending on the scanning direction. This is potentially due to the use of a magnetic compass which introduces a relatively large error in heading estimation and/or an insufficient sensor calibration. The standard deviation is more

consistent between the different lidar scans. It can be observed that the third scan (*e-f*) has a higher standard deviation value compared to the first two. This is expected due to the higher angular incidence of the lidar beams with the hangar roof increasing the effects of the attitude errors.

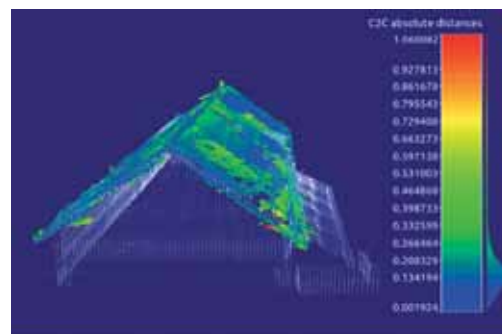
A visualization of the point cloud noise of the two reconstruction methods is depicted in Fig. 7. The lidar and photogrammetric point clouds have been registered with the reference model using the iterative closest point (ICP) method (BESL & MCKAY 1992) to remove the mean distance. It can be noticed that the lidar point cloud is slightly less noisy than the photogrammetric one ( $\sigma$  is smaller) but it has stronger systematic deviations.

For the lidar system, the dominating error source comes from the MEMS IMU and the magnetic compass. From the type of IMU used the expected pitch and roll estimation errors are in the order of  $0.2^\circ - 0.3^\circ$ . With a ground altitude of 45 m this leads to a lidar survey horizontal error of 15 cm – 25 cm. The vertical error is directly related to the RTK GNSS vertical accuracy and the lidar scanner range accuracy (both in the sub-decimetres accuracy range). The other expected relevant source of error comes from heading estimation. The magnetic compass accuracy is in the order of  $1^\circ - 1.5^\circ$ . At a ground altitude of 45 m and scanning angle of  $50^\circ$ , a horizontal error of 35 cm – 55 cm at the border of the lidar strip is expected. The use of a double GNSS antenna instead of a magnetic compass for heading estimation can reduce the heading error of one order of magnitude.

For the photogrammetric system, given the flight altitude  $H = 45$  m, the height/base ratio  $H/B = 4$  (where  $B$  is the baseline between consecutive images), the camera focal length  $f =$



(a) Airborne lidar



(b) Photogrammetry

**Fig. 7:** Deviation between the reference model and reconstruction based on the two methods examined. The values of on the colour bars are in meters.

16 mm and the standard deviation of a measured image coordinate  $\sigma_p = 0.0077$  mm, the expected photogrammetric accuracy is  $\sigma_{xy} \approx 2$  cm (horizontal) and  $\sigma_z \approx 9$  cm (vertical).

### 6.2 Multi-echo Capabilities

The aim of this section is to evaluate the performance of the multi-echo capability of the lidar sensor when operating over a forest. Valuable information such as canopy height could

**Tab. 2:** Point cloud error statistics in meters. Mean is the mean error,  $\sigma$  is the standard deviation and *rms* is the RMS error of the distances between the point clouds.

Lidar a-b	Lidar c-d	Lidar e-f	Photogrammetry
mean: 0.005	mean: 0.607	mean: 0.263	mean: 0.080
$\sigma$ : 0.112	$\sigma$ : 0.107	$\sigma$ : 0.139	$\sigma$ : 0.148
rms: 0.112	rms: 0.616	rms: 0.297	rms: 0.168

be extracted from lidar measurements. The capability of recording 5 different echoes for one pulse can improve the performance in estimating the canopy height compared to a single return lidar sensor.

For this purpose a flight-test was performed over a small forest with the canopy height of about 25 m. The flight altitude was approximately 50 m from the ground level. All five lidar echoes were recorded in the log file. The flight path was executed at the forest border. Measurements falling outside the forest area were manually removed. Fig. 8 (a) shows a snapshot of the helicopter camera view over the forest. Fig. 8 (b) shows a side view snapshot of the lidar measurements while in Fig. 8 (c) only the ground-points are displayed. The ground-points are extracted from elevation by thresholding using the flat-ground assumption.

Tab. 3 presents statistics of the pulse returns of the scanned area. As can be observed from the data, the 4th and 5th echoes did not provide any useful information due to the low number of returns. This implies that the multi-

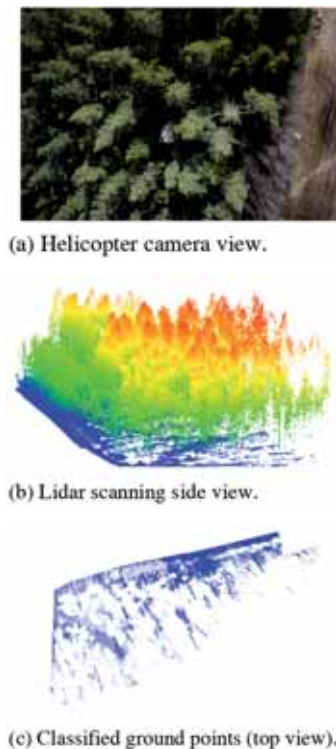


**Fig. 8:** Camera image and lidar measurements.

**Tab. 3:** Number of echoes and classified groundpoints for the scanned forest area of 1 ha size.

Echoes	Total	Ground	% Ground
1st	1141195	182361	16%
2nd	172507	27502	16%
3rd	10233	1571	15.3%
4th	241	18	7.47%
5th	3	3	100%
all	1324179	211455	16%

echo capability of this sensor does not provide additional bare earth information in this kind of environment.

## 7 Conclusions

The paper presented two systems for building digital surface models: an airborne lidar system and photogrammetry-based vision system.

The analysis presented shows that the ALS errors are in line with the expectations. The major source of errors come from the low-cost IMU and the magnetic compass. A dual GNSS antenna can reduce the heading error leading to a more accurate DSM. An in-flight lidar boresight calibration procedure could further reduce the reconstruction errors.

Vision-based techniques can achieve centimetre level accuracy with a simpler system without dealing explicitly with complex calibration and synchronization issues. The flight planning for a photogrammetric system is more complex compared to the ALS system as it is subjected to constraints on the image overlap. Areas with poor visual content have been problematic for the vision system during the tests while the lidar has not shown any problem in this respect.

The ALS hardware is substantially heavier than the video camera, 4.6 kg compared to 0.9 kg (the camera including the GNSS receiver). The cost of the ALS presented is about 15,000 Euro while the camera used was around 1,000 Euro including the lens. It should be pointed out that if an accurate geolocation

of the DSM is required, an RTK GNSS system must be included with the camera system increasing the costs up to 8,000 – 9,000 Euro.

## Acknowledgements

This work is partially supported by the EU FP7 project SHERPA (grant agreement 600958), the Swedish Research Council (VR) Linnaeus Center for Control, Autonomy, and Decision-making in Complex Systems (CADICS), the ELLIIT network organization for Information and Communication Technology, the Swedish National Aviation Engineering Research Program NFFP6 and the SSF – the Swedish Foundation for Strategic Research (CUAS Project).

## References

- BANG, K.I., 2010: Alternative Methodologies for Lidar System Calibration. – PhD thesis, Schulich School of Engineering, University of Calgary, AL, Canada.
- BESL, P. & MCKAY, N.D., 1992: A Method for Registration of 3-D Shapes. – *Pattern Analysis and Machine Intelligence, IEEE Transactions on* **14** (2): 239–256.
- BIERMAN, G., 1977: *Factorization Methods for Discrete Sequential Estimation*. – Academic Press, New York, NY, USA.
- BROWN, R. & HWANG, P., 1992: *Introduction to Random Signal and Applied Kalman Filtering*. – John Wiley & Sons, Inc., second edition.
- CLOUDCOMPARE, 2013: (version 2.4) [GPL software]: <http://www.danielgm.net/cc/> (25.4.2014).
- CONTE, G., 2009: *Vision-Based Localization and Guidance for Unmanned Aerial Vehicles*. – PhD thesis, Linköping University, Sweden.
- DOHERTY, P., HASLUM, P., HEINTZ, F., MERZ, T., NYBLOM, P., PERSSON, T. & WINGMAN, B., 2007: A Distributed Architecture for Autonomous Unmanned Aerial Vehicle Experimentation. – *Distributed Autonomous Robotic Systems* **6**: 233–242.
- EISENBEISS, H. & ZHANG, L., 2006: Comparison of DSMs Generated from Mini UAV Imagery and Terrestrial Laser scanner in a Cultural Heritage Application. – *ISPRS International Archives of Photogrammetry, Remote Sensing and Spatial Information Sciences XXXVI* (part 5).
- GLENNIE, C., BROOKS, B., ERICKSEN, T., HAUSER, D., HUDNUT, K., FOSTER, J. & AVERY, J., 2013: Compact Multipurpose Mobile Laser Scanning System – Initial Tests and Results. – *Remote Sensing* **5** (2): 521–538.
- KAESTNER, R., THRUN, S., MONTEMERLO, M. & WHALLEY, M., 2006: A Non-rigid Approach to Scan Alignment and Change Detection Using Range Sensor Data. – *Field and Service Robotics* **25** (4): 179–194, Springer, Berlin, Heidelberg.
- LIN, Y., HYYPPÄ, J. & JAAKKOLA, A., 2011: Mini-UAV-borne LIDAR for Fine-scale Mapping. – *IEEE Geoscience and Remote Sensing Letters* **8** (3): 426–430.
- LOWE, D., 2004: Distinctive Image Features from Scale-invariant Keypoints. – *International Journal of Computer Vision* **60**: 91–110.
- NAGAI, M., CHEN, T., SHIBASAKI, R., KUMAGAI, H. & AHMED, A., 2009: UAV-borne 3-D Mapping System by Multisensor Integration. – *IEEE Transactions on Geoscience and Remote Sensing* **47** (3): 701–708.
- NEITZEL, F. & KLONOWSKI, J., 2011: Mobile 3d Mapping with a Low-cost UAV System. – *ISPRS International Archives of the Photogrammetry, Remote Sensing and Spatial Information Sciences XXXVIII-1/C22*.
- PIROTTI, F., 2011: Analysis of Full-waveform Lidar Data for Forestry Applications: A Review of Investigations and Methods. – *iForest – Biogeosciences and Forestry* **4**: 100–106.
- PIX4D, 2013: Pix4uav desktop 3D (version 2.1): <http://pix4d.com/> (25.4.2014).
- RAUCH, H., TUNG, F. & STRIEBEL, C., 1965: Maximum Likelihood Estimates of Linear Dynamic Systems. – *AIAA Journal* **3** (8): 1445–1450.
- REMONDINO, F., BARAZZETTI, L., NEX, F., SCAIONI, M. & SARAZZI, D., 2011: UAV Photogrammetry for Mapping and 3D Modeling – Current Status and Future Perspectives. – *ISPRS International Archives of the Photogrammetry, Remote Sensing and Spatial Information Sciences XXXVIII-1/C22*: 25–31.
- SHIN, E.-H., 2005: *Estimation Techniques for Low-Cost Inertial Navigation*. – PhD thesis, University of Calgary, AL, Canada.
- SKALLOUD, J., 1999: *Optimizing Georeferencing of Airborne Survey Systems by INS/DGPS*. – PhD thesis, University of Calgary, AL, Canada.
- WALLACE, L., LUCIEER, A., WATSON, C. & TURNER, D., 2012: Development of a UAV-Lidar System with Application to Forest Inventory. – *Remote Sensing* **4** (6): 1519–1543.
- WEHR, A. & LOHR, U., 1999: Airborne Laser Scanning: An Introduction and Overview. – *ISPRS Journal of Photogrammetry and Remote Sensing* **54** (2-3): 68–82.

## Address of the Authors:

Dr. GIANPAOLO CONTE, M.Sc. PIOTR RUDOL & Prof. PATRICK DOHERTY, Linköping University, Department of Computer and Information Science, S-581 83 Linköping, Sweden, Tel.: +46-13-28-1167, -1606, -2426, e-mail: {gianpaolo.conte}{piotr.rudol}{patrick.doherty}@liu.se

Manuskript eingereicht: Oktober 2013

Angenommen: April 2014

## Hochschulnachrichten

### Universität Stuttgart

#### *Dissertation von Wassim Moussa*

Herr M.Sc. WASSIM MOUSSA promovierte am 28.2.2014 an der Fakultät für Luft- und Raumfahrttechnik und Geodäsie der Universität Stuttgart mit der Arbeit „*Integration of Digital Photogrammetry and Terrestrial Laser Scanning for Cultural Heritage Data Recording*“ zum Dr.-Ing..

Referent: Prof. Dr.-Ing. habil. DIETER FRITSCH, Universität Stuttgart;

Referent: Prof. Dr.-Ing. habil. VOLKER SCHWIEGER, Universität Stuttgart.

#### *Zusammenfassung:*

Die digitale Oberflächenrekonstruktion mit Hilfe von digitaler Photogrammetrie und terrestrischem Laserscanning (TLS) stellt seit längerer Zeit ein Forschungsthema dar. Dies führt zu einer ständigen Weiterentwicklung solcher Systeme, die eine zuverlässige und dichte 3D-Punkterfassung von Objektoberflächen ermöglichen. Aufgrund der Geschwindigkeit und Effizienz der Datenerfassung mittels TLS glaubte man bald nach dem Aufkommen dieser Methode, dass die Nahbereichsphotogrammetrie durch TLS Systeme ersetzt werden würde. Andererseits legten viele Wissenschaftler dar, dass die photogrammetrische Erfassung durch die Verwendung von Verfahren zur dichten Bildzuordnung (Dense Image Matching) mit viel geringeren Kosten realisiert werden könne. Jedoch wurde offensichtlich, dass das Erreichen des höchsten Effizienz- und Flexibilitätsgrades nur durch den gemeinsamen Einsatz beider Techniken zu erreichen ist und komplette und konsistente Ergebnisse sicherstellt, vor allem bei der Erfassung von komplexen Objekten wie Kulturdenkmälern. Diese Kombination ermöglicht die Ausnutzung der Vorteile beider Messprinzipien: Laufzeitmessung TLS kann eingesetzt werden, um großräumige Punktwolken in mittleren Distanzen zu erfassen, wohingegen die bildbasierte Oberflächenrekonstruktion eine flexible, hochpräzise Erfassung auf kurze Distanzen ermöglicht.

Daher diskutiert diese Arbeit das Potential der Kombination von digitalen Bildern und TLS-Daten für Anwendungen im Nahbereich, wobei im Speziellen auf die 3D-Datenerfassung für die Konservierung von Kulturdenkmälern eingegangen wird. In dieser Arbeit wird ein automatisches Verfahren für die Kombination von Bildern und Laserscanner-Daten präsentiert, welche das Ziel verfolgt, eine vollständige digitale Repräsentation einer Szene zu erstellen. Über diese Verbesserung der geometrischen und visuellen Qualität des Modells hinaus hat diese Kombination des Weiteren zum Ziel, Probleme aufzuzeigen, die weiteren Untersuchungen bedürfen. Dazu gehören das Füllen von Datenlücken in den TLS-Daten, um Modellierungsfehler zu vermeiden, und die Erfassung von mehr Details in höherer Auflösung sowie die Zielmarken freie Registrierung mehrerer Scans. Das Integrationsverfahren basiert auf der Reduktion der Merkmalsextraktion von einem 3D- auf ein 2D-Problem durch die Verwendung synthetischer bzw. virtueller Bilder, welche aus den 3D-Laser-Daten berechnet werden.

Das Verfahren besteht aus drei Methoden zur Datenfusion. Die erste Methode verwendet eine Szenendatenbank, welche in einem punktbasierten Umgebungsmodell (Point-based Environment Model – PEM) gespeichert ist und die 3D TLS-Punktwolken zusammen mit ihren Intensitäts- und RGB-Werten enthält. Das PEM erlaubt die Extraktion präziser Kontrollinformation sowie Kamerapositionen relativ zu den TLS-Daten und 2D-3D-Korrespondenzen zwischen jedem Bild und den 3D-Daten, was die direkte Berechnung von absoluten Kameraorientierungen mit Hilfe von präzisen räumlichen Rückwärtsschnitten ermöglicht. Die zweite Methode verwendet einen Structure-from-Motion (SfM)-Ansatz für die vorangehende Berechnung der lokalen relativen Orientierungen der Bilder. Diese Orientierungen werden eingesetzt, um eine Oberflächenrekonstruktion mittels Verfahren zur dichten Bildzuordnung zu berechnen. Daraufhin können die 3D-3D-Korrespondenzen zwischen dem Ergebnis der

dichten Bildzuordnung und Punkten des PEM bestimmt werden. Hierfür wird die dichte Punktwolke in mindestens ein Kamerabild projiziert und die 3D-3D-Korrespondenzen zwischen den projizierten Punkten und jenen aus dem PEM extrahierten gesucht. Alternativ können auch die 3D-3D-Kamerapositionen für diesen Zweck eingesetzt werden. Dadurch werden die Parameter einer Helmert-Transformation berechnet und eingesetzt, um die absolute Orientierung jedes Bildes in Bezug zu den TLS-Daten zu bestimmen.

Die Ergebnisse werden durch die Einführung einer allgemeingültigen Lösung, der dritten Methode, weiter verbessert, welche die synthetischen Bilder und die Kamerabilder in einem gemeinsamen SfM-Prozess vereint. Dieser Prozess hat genaue Bildorientierungen und dünn besetzte Punktwolken zum Ergebnis, welche zunächst in einem beliebigen Koordinatensystem vorliegen. Dies ermöglicht eine implizite Bestimmung von 3D-3D-Korrespondenzen zwischen der dünn besetzten Punktwolke und den TLS-Daten unter Verwendung der 2D-3D-Korrespondenzen, die in den generierten Bildern enthalten sind. Alternativ können die dünn besetzten Punktwolken mittels der Kollinearitätsgleichung auf die virtuellen Bilder projiziert werden, um die Messredundanz zu erhöhen. Daraufhin werden die Parameter einer Helmert-Transformation berechnet. Deren Verfügbarkeit ermöglicht eine automatische Registrierung mehrerer Laserscans, insbesondere solcher, die mit stark unterschiedlichen Sichtfeldern oder ohne Überlappung erfasst wurden. Darüber hinaus können über die dichte Bildzuordnung weitere Oberflächeninformationen aus den Bildern extrahiert werden. Aufgrund der gemeinsamen Bündelblockausgleichung liegen die Ergebnisse dieses Schrittes im gleichen Koordinatensystem und mit dem gleichen Maßstab vor wie die TLS-Daten und können daher direkt verwendet werden, um Datenlücken oder verdeckte Bereiche in den TLS-

Punktwolken zu füllen oder kleine Objektetails aufzulösen.

Darüber hinaus wurden zwei bildbasierte Methoden für die automatische paarweise Registrierung von mehreren Laserscans basierend auf dem PEM und den geometrischen Beziehungen zwischen gemeinsamen Punkten entwickelt. Dies beinhaltet einen Schritt zur Organisation der Scans auf Basis einer gerichteten Graphstruktur, die präzise und schnell Verbindungen zwischen einzelnen Scans anhand von Merkmalspunkten zwischen allen Scans identifiziert. Des Weiteren werden 3D-Modelle von Denkmälern genutzt, indem diese mittels bild- und distanzmessenden Techniken erfasst und sowohl für Dokumentation und digitale Erhaltung, als auch für geschichtliche Interpretation, Restaurierung und Bildung nutzbar gemacht werden. Die vorgeschlagenen Methoden wurden im Rahmen von Fallstudien anhand von verschiedenen Bildern und unter Verwendung verschiedener Sensoren getestet, um ihre Allgemeingültigkeit und Effizienz aufzuzeigen.

Über die Präsentation einer neuen Methode für die Kombination von Fotografien und Laserscanner Daten hinaus werden in dieser Arbeit einige wichtige Probleme und deren Lösungen in der Praxis von Low-cost Nahbereichsanwendungen aufgezeigt. Dies soll die Datenfusion von Low-cost Sensoren wie der Microsoft Kinect und Mobiltelefonen für Anwendungen im Innen- und Außenbereich motivieren.

Die Dissertation ist in der Reihe C der Deutschen Geodätischen Kommission bei der Bayerischen Akademie der Wissenschaften (ISSN: 0065-5325, ISBN 978-3-7696-5137-9) unter der Nr. 725 online veröffentlicht (<http://dgk.badw.de/index.php?id=12>). Gleichzeitig erscheint die Arbeit in elektronischer Form bei der Bibliothek der Universität Stuttgart (<http://elib.uni-stuttgart.de/opus/doku/e-diss.php>).

## Mitteilung der Deutschen Geodätischen Kommission (DGK)

### DGK Wissenschaftspreis 2014

Die Deutsche Geodätische Kommission (DGK) hat den Preisträger des DGK-Preises 2012 bekannt gegeben: Es ist Dr.-Ing. JAN DIRK WEGNER von der ETH Zürich. JAN DIRK WEGNER (Jahrgang 1982) ist ein Experte auf dem Gebiet der Mustererkennung zur automatischen Extraktion und 3D-Modellierung von Objekten für Anwendungen in Photogrammetrie, Fernerkundung und Computer Vision. Die DGK würdigt seine international sehr anerkannten Arbeiten, in denen er neuartige wahrscheinlichkeitstheoretische Mustererkennungsansätze entwickelt hat, die mittels maschinellen Lernens automatisch Kartierungen erlauben. Darüber hinaus engagiert sich Dr. WEGNER in der Internationalen Gesellschaft für Photogrammetrie und Fernerkundung, um weltweit modernste Fernerkun-

dungsdaten öffentlich und frei für Benchmarks zugänglich zu machen.

Der Wissenschaftspreis der Deutschen Geodätischen Kommission wurde im Jahre 2011 zur Förderung hochqualifizierter Wissenschaftlerinnen und Wissenschaftler ins Leben gerufen und wird in diesem Jahr auf der im Oktober in Berlin stattfindenden INTERGEO 2014 überreicht. Der DGK-Preis ist für junge Wissenschaftlerinnen und Wissenschaftler mit bereits ausgeprägt internationalem Profil gedacht. Als Grundlage für die Beurteilung der Preiswürdigkeit dient die wissenschaftliche Gesamtleistung einschließlich der nach der Promotion veröffentlichten wissenschaftlichen Publikationen. Der Preis wird alle zwei Jahre vergeben und besteht aus einer Urkunde und einem Preisgeld in Höhe von 2.000,- €.

## Neuerscheinung

BEHR, F.-J., 2014: Strategisches GIS-Management. – 3. neu bearbeitete Auflage, Wichmann-Verlag, 322 Seiten. ISBN 978-3-87807-534-8.

Die Einführung und das Management von Geoinformationssystemen stellen an jede Or-

ganisation hohe Anforderungen in Bezug auf Qualifikation, Organisation und Finanzierung. Das informative Buch vermittelt erfolgsrelevante Aspekte für den gesamten Prozess – von der Planung bis zur Systemimplementierung.

## Veranstaltungskalender

### 2014

24.–28. August: **International Conference on Pattern Recognition (ICPR) 2014** in Stockholm, Schweden. [icpr2014.org](http://icpr2014.org)

5.–7. September: **ISPRS Technical Commission III Symposium – Photogrammetric Computer Vision 2014** in Zürich, Schweiz. [isprs.org/pcv2014](http://isprs.org/pcv2014)

5.–12. September: **European Conference on Computer Vision (ECCV) 2014** in Zürich, Schweiz. [eccv2014.org](http://eccv2014.org)

17.–18. September: **14. Seminar GIS & Internet „Integrierte Lösungen, ausgewählte IT- und GIS-Trends“**, Universität der Bundeswehr, München. [unibw.de/inf4/professuren/geoinformatik/seminar-gis-und-internet](http://unibw.de/inf4/professuren/geoinformatik/seminar-gis-und-internet)

22.–25. September: **SPIE Remote Sensing 2014** in Amsterdam, Niederlande. [spie.org/remotesensing-europe.xml?WT.mc\\_id=RCaI-ERSW](http://spie.org/remotesensing-europe.xml?WT.mc_id=RCaI-ERSW)

23.–26. September: **GIScience 2014** in Wien, Österreich. [giscience.org](http://giscience.org)

24.–25. September: **International Workshop on Remote Sensing and GIS for Monitoring of Habitat Quality** in Wien, Österreich. [rsgis4hq.geo.tuwien.ac.at/](http://rsgis4hq.geo.tuwien.ac.at/)

29. September – 2. Oktober: **ISPRS Technical Commission VII Symposium 2014** in Istanbul, Türkei. [isprstc7-2014.org/](http://isprstc7-2014.org/)

6.–8. Oktober: **ISPRS Technical Commission II Symposium 2014** in Toronto, Kanada. [www2.isprs.org/2014GeoTPMA/home.html](http://www2.isprs.org/2014GeoTPMA/home.html)

7.–9. Oktober: **INTERGEO 2014** in Berlin. [Intergeo.de](http://Intergeo.de)

22.–24. Oktober: **International Conference on Image Analysis and Recognition (ICIAR) 2014** in Vilamoura, Portugal. [aimiconf.org/iciar14](http://aimiconf.org/iciar14)

27.–30. Oktober: **International Conference on Image Processing (ICIP) 2014** in Paris, Frankreich. [icip2014.com](http://icip2014.com)

3.–8. November: **EUROMED 2014 – Progress in Cultural Heritage e-Documentation, Preservation and Protection** in Limassol, Zypern. [culturalheritage2014.eu](http://culturalheritage2014.eu)

11.–13. November: **3d GeoInfo 2014** in Dubai, Vereinigte Arabische Emirate. [3dgeoinfo2014.org](http://3dgeoinfo2014.org)

15.–17. November: **GI Research2014** in Teheran, Iran. [giresearch.ut.ac.ir](http://giresearch.ut.ac.ir)

17.–20. November: **ISPRS Technical Commission I Symposium 2014** in Denver, USA. [isprs.org/2014tc1symposium](http://isprs.org/2014tc1symposium)

26.–27. November: **MoLaS 2014 – Mobile Laserscanning Technology Workshop** in Freiburg. [ipm.fraunhofer.de/en/tradefairs-events/molas-workshop-2014.html](http://ipm.fraunhofer.de/en/tradefairs-events/molas-workshop-2014.html)

26.–28. November: **11<sup>th</sup> Symposium on Location-Based Services** in Wien, Österreich. [lbs2014.org](http://lbs2014.org)

2.–3. Dezember: **LowCost3D 2014** in Dresden. [lc3d.net](http://lc3d.net)

4.–5. Dezember: **3D-NordOst 2014** in Berlin. [3d-nordost.de](http://3d-nordost.de)

9.–12. Dezember: **ISPRS Technical Commission VIII Symposium 2014** in Hyderabad, Indien. [nrsc.gov.in/technicalcommission8.html](http://nrsc.gov.in/technicalcommission8.html)

14.–17. Dezember: **ICDM - IEEE Conference on Data Mining 2014** in Shenzhen, China. [icdm2014.sfu.ca/](http://icdm2014.sfu.ca/)

Weitere Konferenzen und Workshops finden sich beispielsweise unter:  
<http://www.isprs.org/calendar/default.aspx> und  
[iris.usc.edu/Information/iris-conferences.html](http://iris.usc.edu/Information/iris-conferences.html)

## Korporative Mitglieder

### Firmen

AEROWEST GmbH  
 AICON 3D Systems GmbH  
 aphos Leipzig AG  
 Becker GeoInfo GmbH  
 Bernhard Harzer Verlag GmbH  
 Blom Deutschland GmbH  
 Brockmann Consult GmbH  
 bsf swissphoto GmbH  
 Büro Immekus  
 CGI Systems GmbH  
 DB Netz AG  
 DELPHI IMM GmbH  
 Deutsches Bergbau-Museum  
 EFTAS Fernerkundung Technologietransfer GmbH  
 ESG Elektroniksystem- und Logistik-GmbH  
 Esri Deutschland GmbH  
 EUROPEAN SPACE IMAGING  
 Eurosense GmbH  
 fokus GmbH  
 g.on experience gmbh  
 GAF GmbH  
 GeoCart Hertzen GmbH  
 GeoContent GmbH  
 Geoinform. & Photogr. Engin. Dr. Kruck & Co. GbR  
 geoplana Ingenieurgesellschaft mbH  
 GEOSYSTEMS GmbH  
 GGS - Büro für Geotechnik, Geoinformatik, Service  
 Hansa Luftbild AG  
 IGI - Ingenieur-Gesellschaft für Interfaces mbH  
 ILV Ingenieurbüro für Luftbilddatenauswertung und Vermessung  
 Infoterra GmbH  
 INVERS - Industrievermessung & Systeme  
 ITT Visual Information Solutions Germany  
 J. Linsinger ZT-GmbH  
 Leica Geosystems GmbH  
 Luftbilddatenbank-Würzburg  
 Messbildstelle GmbH  
 Microsoft Photogrammetry  
 MILAN Geoservice GmbH  
 M.O.S.S. Computer Grafik Systeme GmbH  
 PHOENICS GmbH  
 PMS - Photo Mess Systeme AG  
 RapidEye AG  
 RIEGL Laser Measurement Systems GmbH  
 RWE Power AG, Geobasisdaten/Markscheidewesen  
 technet GmbH  
 topometric GmbH  
 TRIGIS Vermessung + Geoinformatik GmbH  
 Trimble Germany GmbH  
 trimetric 3D Service GmbH

Wichmann, VDE Verlag GmbH  
 Z/I Imaging Ltd.

### Behörden

Amt für Geoinformationswesen der Bundeswehr  
 Bayerische Landesanstalt für Wald und Forstwirtschaft  
 Bundesamt für Kartographie und Geodäsie  
 Bundesministerium für Ernährung, Landwirtschaft und Verbraucherschutz  
 Hessisches LA für Bodenmanagement und Geoinformation  
 Innenministerium NRW, Gruppe Vermessungswesen  
 Institut für Umwelt- und Zukunftsforschung  
 LA für Geoinformation und Landentwicklung, BW  
 LA für Vermessung und Geoinformation, Bayern  
 LB Geoinformation und Vermessung, Hamburg  
 LB für Küstenschutz, Nationalpark und Meeresschutz, SH  
 Landeshauptstadt Düsseldorf, Vermessungs- und Liegenschaftsamt  
 Landesvermessung und Geobasisinformation Niedersachsen  
 Märkischer Kreis, Vermessungs- und Katasteramt  
 Regierungspräsident Tübingen, Abt. 8 Forstdirektion  
 Regionalverband Ruhr  
 Staatsbetrieb Sachsenforst Pirna  
 Stadt Bocholt, Fachbereich 31  
 Stadt Köln, Amt für Liegenschaften, Vermessung und Kataster  
 Stadt Wuppertal, Vermessung, Katasteramt und Geodaten  
 Thüringer LA für Vermessung und Geoinformation

### Hochschulen

BTU Cottbus, Lehrstuhl für Vermessungskunde  
 FH Frankfurt a.M., FB 1, Studiengang Geoinformation  
 FH Mainz, Institut für Raumbezogene Informations- und Messtechnik  
 Jade Hochschule, Institut für Angewandte Photogrammetrie und Geoinformatik  
 HCU HafenCity Universität Hamburg, Geomatik  
 HfT Stuttgart, Vermessung und Geoinformatik  
 HS Bochum, FB Vermessung und Geoinformatik  
 HS Karlsruhe, Fakultät für Geomatik  
 HTW Dresden, FB Vermessungswesen/Kartographie  
 LUH Hannover, Institut für Kartographie und Geoinformatik  
 LUH Hannover, Institut für Photogrammetrie und Geoinformation  
 MLU Halle, FG Geofernerkundung

- Ruhr-Uni Bochum, Geographisches Institut  
RWTH Aachen, Geodätisches Institut  
TU Bergak. Freiberg, Institut für Markscheidewesen und Geodäsie  
TU Berlin, Computer Vision & Remote Sensing  
TU Berlin, Institut für Geodäsie und Geoinformationstechnik  
TU Braunschweig, Institut für Geodäsie und Photogr.  
TU Clausthal, Institut für Geotechnik und Markscheidewesen  
TU Darmstadt, Institut für Photogrammetrie und Kartographie  
TU Dresden, Institut für Photogrammetrie und Fernerkundung
- TU München, FG Photogrammetrie und Fernerkundung  
TU Wien, Institut für Photogrammetrie und Fernerkundung  
Uni Bonn, Institut für Photogrammetrie  
Uni Göttingen, Institut für Waldinventur und Waldwachstum  
Uni Heidelberg, IWR Interdisziplinäres Zentrum für Wissenschaftliches Rechnen  
Uni Kassel, FB Ökologische Agrarwissenschaften  
Uni Kiel, Geographisches Institut  
Uni Stuttgart, Institut für Photogrammetrie  
Uni Würzburg, Geographisches Institut  
Uni zu Köln, Geographisches Institut